Search for Microscopic Black Hole Signatures at the Large Hadron Collider

by

Ka Vang Tsang

B.Sc., The University of Hong Kong; Hong Kong, 2003

M.Phil., The University of Hong Kong; Hong Kong, 2005

A dissertation submitted in partial fulfillment of the requirements for the degree of Doctor of Philosophy in Department of Physics at Brown University

PROVIDENCE, RHODE ISLAND

May 2011

This dissertation by Ka Vang Tsang is accepted in its present form

by Department of Physics as satisfying the

dissertation requirement for the degree of Doctor of Philosophy.

Date________________ ____

Greg Landsberg, Advisor

Recommended to the Graduate Council

Date________________ ____

Antal Jevicki, Reader

Date________________ ____

Meenakshi Narain, Reader

Approved by the Graduate Council

Date________________ ____

Peter M. Weber, Dean of the Graduate School

Vitae

Ka Vang Tsang was born on November 2, 1981 in Macau. He received his B.Sc. in Mathematics/Physics in 2003, and M.Phil. in Physics in 2005 from the University of Hong Kong. He came to Brown University in 2005, and has been advised by Prof. Greg Landsberg since 2006.

Acknowledgements

Merci!

Abstract of " Search for Microscopic Black Hole Signatures at the Large Hadron Collider " by Ka Vang Tsang, Ph.D., Brown University, May 2011

A search for microscopic black hole production and decay in proton-proton collisions at a center-of-mass energy of 7 TeV has been conducted using Compact Muon Solenoid (CMS) detector at the CERN Large Hadron Collider. A total integrated luminosity of 35 pb^{-1} data sample, taken by CMS Collaboration in year 2010, has been analyzed. A novel background estimation for multi-jet events beyond TeV scale has been developed. A good agreement with standard model backgrounds, dominated by multi-jet production, is observed for various final-state multiplicities. Using semi-classical approximation, upper limits on minimum black hole mass at 95% confidence level are set in the range of 3.5 - 4.5 TeV for values of the Planck scale up to 3 TeV. Model-independent limits are provided to further constrain microscopic black hole models with additional regions of parameter space, as well as new physics models with multiple energetic final states. These are the first limits on microscopic black hole production at a particle accelerator.

Contents

List of Tables

List of Figures

Chapter 0

Introduction

With the startup of the Large Hadron Collider (LHC), the high-energy particle physics field is entering to a new era. The LHC is the highest energy proton-proton collider with designed center-of-mass energy of 14 TeV, allowing to probe new physics at TeV energy scale. Microscopic black hole production [1, 2] is predicted, assuming the existence of extra dimensions [3]. The observation of microscopic black hole signature via Hawking radiation [4] provides a new foundation for quantum gravity, which leads to the unification of quantum mechanics and general relativity at a few TeV energy scale.

The goal of this work is to search for microscopic black hole signatures at LHC with center-of-mass energy 7 TeV, using $34.7 \pm 3.8\,\mathrm{pb}^{-1}$ of data taken by Compact Muon Solenoid (CMS) experiment in year 2010. This Dissertation is arranged in five additional chapters. Chapter 1 introduces the standard model, a review of current understanding on particle physics. Chapter 2 describes several solutions of Einstein field equations as classical black holes, followed by a short introduction of large extra dimensions and the mechanism of microscopic black hole production at LHC. Properties of simulated microscopic black hole signatures are studied with two event generators: BlackMax [5] and CHARYBDIS [6]. Chapter 3 briefly describes the LHC facility and the main components of CMS experiment. Chapter 4 looks at the data taken and discusses the workflow of the analysis, including particle identification, event selection, background and signal acceptance estimation together with their systematic uncertainties, results of the search, and the limit setting procedures. Finally, Chapter 5 concludes this Dissertation.

Chapter 1

Theory I: The Standard Model

The standard model is a theory of gauge group $SU_c(3) \times SU_L(2) \times U_Y(1)$, describing strong, weak, and electromagnetic interactions between elementary particles. The basic components of the standard model are leptons, quarks, and gauge bosons. Leptons are denoted as left-handed isospin doublets and right-handed isospin singlet under $SU_L(2)$ symmetry:

$$\psi_L = \begin{pmatrix} l^- \\ \nu_l \end{pmatrix}_L \text{ and } \psi_R = (l)_R \, ,$$

where l represents $\{e, \mu, \tau\}$, and there is no right-handed neutrino singlet in standard model. Similarly, quarks are represented as

$$\psi_L = \begin{pmatrix} u_i \\ d'_i \end{pmatrix}_L \text{ and } \psi_R = (u_i)_R \, , (d'_i)_R \, ,$$

where u_i, d_i are the three quarks families, namely $\{u, c, t\}$ and $\{d, s, b\}$, respectively. The weak isospin doublet of light quarks (d'_i) are rotated from strong isospin doublet (d_i) by the Cabibbo-Kobayashi-Maskawa matrix [7] (V_{ij}): $d'_i = \sum_j V_{ij} d_j$. Gauge bosons are fields associated with the generators of the group $SU_c(3) \times SU_L(2) \times U_Y(1)$. There are eight gauge fields for $SU_c(3)$, labeled as gluons G^{α}_{μ} ($\alpha = 1, 2, .., 8$). Unless otherwise specified, Greek indices represent 4-dimensional space-time components in this dissertation. The subscript c of $SU_c(3)$ group indicates color quantum numbers for the gluons. There are three gauge fields W^a_μ ($a = 1, 2, 3$) for $SU_L(2)$, and one field for $U_Y(1)$ labeled as B_μ. The subscript Y means weak hypercharge quantum number, while subscript L emphasizes the weak isospin quantum number carried by left-handed fields only. The four gauge fields (W^a_μ, B_μ) are responsible for electroweak interaction, and can be identified as $W^\pm/Z$ bosons and photon after spontaneous symmetry breaking.

1.1 Electroweak Interaction

The Standard Model of Electroweak Interactions, known as the Glashow-Weinberg-Salam model [8, 9, 10], is a theory unifying electromagnetic and weak interactions, and belongs to a subgroup of standard model ($SU_L(2) \times U_Y(1)$). The fermions part of the Lagrangian can be written as

$$\mathcal{L}_F \sim \sum_i \bar{\psi}_i \not{D} \psi_i,$$

where the sum runs through all types of isospin doublets and singlets, and the slashed notation $\not{D} = \gamma^\mu D_\mu$ is a shorthand for index contraction with Dirac matrices (γ^μ) and gauge covariant derivative D_μ. In terms of the generators of $SU_L(2)$ and $U_Y(1)$

groups, the gauge covariant derivative is written as

$$D_\mu = \partial_\mu + i\frac{g}{2}\tau_{La}W^a_\mu + i\frac{g\prime}{2}YB_\mu,$$

where τ_{La} are Pauli matrices - generators of $SU_L(2)$, Y is a scalar, and g, g' are coupling constants. The subscript L of Pauli matrices indicates that the middle term associated with $SU_L(3)$ acts on left-handed fermions only. The algebra of the group gives the following commutation relations

$$[\tau_{La}, \tau_{Lb}] = i\epsilon_{abc}\tau_{Lc}, \text{ and } [\tau_{Li}, Y] = 0,$$

where ϵ_{abc} is Levi-Civita symbol. Since Y commutes with any one of the Pauli matrices, the quantum number Q is defined by the Gell-Mann-Nishijima formula [11, 12]:

$$Q = I_3 + \frac{1}{2}Y,$$

where Q is the electric charge, I_3 is projection of isospin on any axis, labeled as 3, and Y is the hypercharge. The gauge fields part of the electroweak Lagrangian is

$$\mathcal{L}_{\text{gauge}} = -\frac{1}{4}W^{\mu\nu}_a W^a_{\mu\nu} - \frac{1}{4}B_{\mu\nu}B^{\mu\nu}, \tag{1.1}$$

with the field strength tensors:

$$\begin{aligned} W^a_{\mu\nu} &= \partial_\mu W^a_\nu - \partial_\nu W^a_\mu + g\epsilon_{abc}W^b_\mu W^c_\nu, \\ B_{\mu\nu} &= \partial_\mu B_\nu - \partial_\nu B_\mu. \end{aligned}$$

The free Lagrangian from $\mathcal{L}_F$ and $\mathcal{L}_{\text{gauge}}$ gives massless fermions and gauge bosons, which does not reflect physical world. The solution is to apply a spontaneous local symmetry breaking on the group $SU_L(2) \times U_Y(1)$ via the Englert-Brout-Higgs-

Guralnik-Hagen-Kibble mechanism or simply the Higgs mechanism, which published independently almost at the same time in three papers by Higgs [13]; Brout and Englert [14]; and Guralnik, Hagen, and Kibble [15]. Lagrangian of a free scalar doublet (Higgs field φ) is introduced:

$$\mathcal{L}_\varphi = \not{D}_\mu \varphi^\dagger \not{D}^\mu \varphi - m_H^2 \varphi^\dagger \varphi - \lambda(\varphi^\dagger \varphi)^2,$$

where m_H is latter identified as the mass of the Higgs boson and λ is the coupling constant for the Higgs field. The symmetry of electroweak group is broken into exact electromagnetic symmetry:

$$SU_L(2) \times U_Y(1) \rightarrow U_{\mathrm{EM}}(1),$$

to maintain massless photon and electric charge conservation. Meanwhile, the Higgs field becomes

$$\varphi = \begin{pmatrix} \varphi^+ \\ \varphi^0 \end{pmatrix} \rightarrow \frac{1}{\sqrt{2}} \begin{pmatrix} 0 \\ v + H \end{pmatrix},$$

where $v = \sqrt{-m_H^2/\lambda}$ is the vacuum expectation value of the Higgs field, and H is the Higgs field relative to the vacuum v. Gauge fields are transformed by the following equations:

$$\begin{aligned} W_\mu^\pm &= \frac{1}{\sqrt{2}}(W_\mu^1 \mp W_\mu^2), \\ \begin{pmatrix} A_\mu \\ Z_\mu \end{pmatrix} &= \begin{pmatrix} \cos\theta_W & \sin\theta_W \\ -\sin\theta_W & \cos\theta_W \end{pmatrix} \begin{pmatrix} B_\mu \\ W_\mu^3 \end{pmatrix}, \end{aligned}$$

where $\theta_W = \tan^{-1}(g'/g)$ is the Weinberg angle. The Higgs part of the Lagrangian after spontaneous symmetry breaking is

$$\begin{aligned}
\mathcal{L}_\varphi &= \frac{1}{2}(\partial H)^2 - \frac{1}{2}m_H^2 H^2 \\
&- \frac{1}{8}m_H^2 v^2 \left(-1 + \frac{4H^3}{v^3} + \frac{H^4}{v^4}\right) \\
&+ \frac{1}{4}g^2 W_\mu^+ W^{-\mu}(v+H)^2 + \frac{1}{8}\frac{g'^2}{\sin^2\theta_W} Z_\mu Z^\mu (v+H)^2. \qquad (1.2)
\end{aligned}$$

The first two lines of the Lagrangian are the kinetic and mass terms for Higgs scalar field and its cubic and quartic self interactions. The last line contains the mass terms of the W and Z bosons:

$$M_W^2 W_\mu^+ W^{-\mu} + \frac{1}{2}M_Z^2 Z_\mu Z^\mu,$$

where M_W and M_Z are now massive by coupling to the Higgs vacuum expectation value:

$$\begin{aligned}
M_W &= \frac{gv}{2}, \\
M_Z &= \frac{g'v}{2\sin\theta_W} \\
&= \frac{M_W}{\cos\theta_W}.
\end{aligned}$$

Note that the gauge field (A_ν) does not appear in the mass term, implying that the photon remains massless after spontaneous symmetry breaking. The Higgs part of the Lagrangian also contains coupling terms, which are responsible for WWH, ZZH, $WWHH$ and $ZZHH$ interactions.

The Higgs field interacts to the fermion fields as well. In terms of the fermions mass eigenstates, the coupling term is $m_i\bar{\psi}_i\psi_i(1 + H/v)$. The strength of coupling between fermion and Higgs field $m_i/v = gm_i/2M_W$ is very small except for the top quarks. The fermions part of the Lagrangian is written as

$$\begin{aligned}
\mathcal{L}_F &= \sum_i \bar{\psi}_i \left(i\partial\!\!\!/ - m_i - \frac{gm_iH}{2M_W} \right) \psi_i \\
&- \frac{g}{2\sqrt{2}} \sum_i \bar{\psi}_i \gamma^\mu (1-\gamma^5)(T^+W_\mu^+ - T^-W_\mu^-)\psi_i \\
&- e\sum_i q_i\bar{\psi}_i\gamma^\mu\psi_i A_\mu \\
&- \frac{g}{2\cos\theta_W} \sum_i \bar{\psi}_i\gamma^\mu(g_V^i - g_A^i\gamma^5)\psi_i Z_\mu, \qquad (1.3)
\end{aligned}$$

where $T^\pm = (\tau_{L1} \mp \tau_{L2})/2$ are the weak isospin raising and lowering operators, $e = g\sin\theta_W$ is the positron electric charge, and q_i is charge of ψ_i in unit of e. The vector and axial-vector coupling are

$$\begin{aligned}
g_V^i &= t_{3L}^i - 2q_i\sin^2\theta_W, \\
g_A^1 &= t_{3L}^i,
\end{aligned}$$

where t_{3L}^i is the weak isospin of fermion i (+1/2 for u_i and ν_l; -1/2 for d_i and l). Putting Equations 1.1, 1.2 and 1.3 together, the Lagrangian for electroweak interaction after spontaneous symmetry breaking is

$$\mathcal{L}_{\mathrm{EW}} = \mathcal{L}_F + \mathcal{L}_{\mathrm{gauge}} + \mathcal{L}_\varphi.$$

The crossing terms of $\mathcal{L}_{\mathrm{gauge}}$ are responsible for the self-interaction of gauge fields: WWZ, $WW\gamma$, $WWWW$, $WWZZ$, $WWZ\gamma$, and $WW\gamma\gamma$. There are three free parameters in the gauge part of the Lagrangian: g, v, and θ_W. The coupling constants are related to two precisely measured numbers: fine structure constant $\alpha(0) = 1/137.035999679(94)$ [16], determined from the $e^\pm$ anomalous magnetic moment [17]; and Fermi coupling constant $G_F = 1.16637(1) \times 10^5\,\mathrm{GeV}^2$ [16], determined from the muon lifetime experiments [18, 19]. The Weinberg angle $\sin^2(\theta_W) = 0.23116(13)$ [16] is obtained from $W^{\pm}$ boson mass $M_W = 80.399(23)\,\text{GeV}$ [16] and Z boson mass $M_Z = 91.1876(21)\,\text{GeV}$ [16]. All three parameters are obtained experimentally from the following relations:

$$\begin{aligned} \alpha(0) &= \frac{g\sin^2\theta_W}{4\pi} \\ G_F &= \frac{1}{\sqrt{2}v^2}. \end{aligned}$$

For the mass terms, all leptons and quarks masses are measured [16], except the mass of Higgs bosons m_H. Neutrinos are assumed to be massless in the original standard model construction. Extension of the standard model for including neutrino masses can be found in Refs. [20, 21, 22].

1.2 Strong Interaction

The strong interaction, also known as quantum chromodynamics (QCD), is a $SU_c(3)$ gauge theory of the standard model. The Lagrangian of QCD is

$$\mathcal{L}_{\text{QCD}} = -\frac{1}{4}F^{(a)}_{\mu\nu}F^{(a)\mu\nu} + i\sum_q \bar{\psi}^i_q (\not{D}_\mu)_{ij}\psi^j_q - \sum_q m_q \bar{\psi}^i_q \psi^i_q,$$

where the field strength tensors and gauge covariant derivative are defined as

$$\begin{aligned} F^{(a)}_{\mu\nu} &= \partial_\mu G^a_\nu - \partial_\nu G^a_\mu - g_s f_{abc} G^b_\mu G^c_\nu, \\ (D_\mu)_{ij} &= \delta_{ij}\partial_\mu + i g_s \sum_a \frac{\lambda^a_{i,j}}{2} G^a_\mu. \end{aligned}$$

Here g_s is the QCD coupling constant, and the structure constants f_{abc} $(a, b, c = 1, .., 8)$ are defined by

$$[\lambda^a, \lambda^b] = 2if_{abc}\lambda^c,$$

where λ are the Gell-Mann matrices (i.e. representations of $SU_c(3)$). The ψ_q^i are Dirac spinors of quark fields with color i and flavor q. The gauge part of the QCD Lagrangian contains gluon self-interaction of three-point coupling with strength g_s, and four-point coupling with strength g_s^2. The strong interaction has a property of asymptotic freedom, so the running coupling constant becomes small at short distance or high energy. At low energy or long distance, the coupling constant becomes large, known as quark and gluon confinement, and therefore perturbation method does not work very well in this regime. The coupling constant $\alpha_s(Q) = g_s^2(Q)/4\pi$ as a function of energy scale (Q) is shown in Figure 1.1.

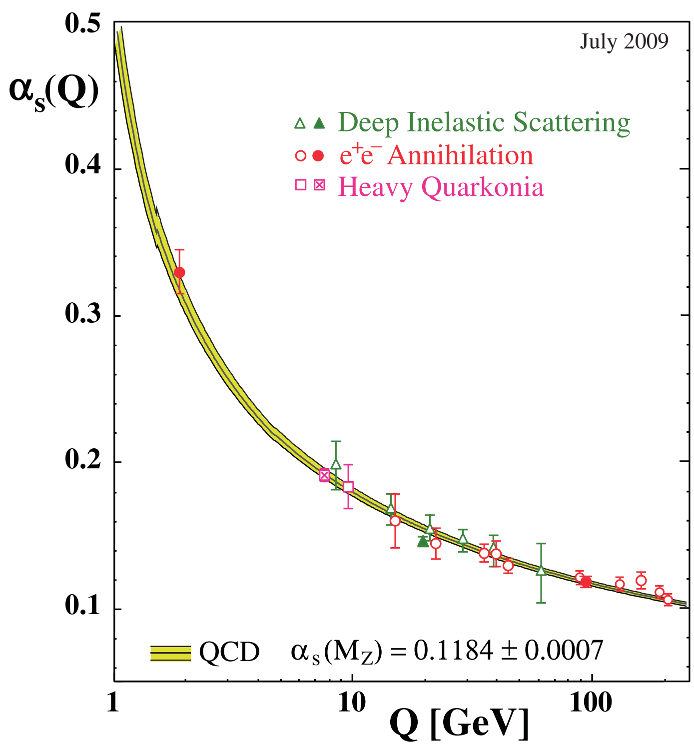

Figure 1.1: Measurements of QCD coupling constant α_s as a function of energy scale Q [16].

Hadronization is the process of hadrons formation from partons: quarks and gluons. Since this process is non-perturbative at short distance, the products of hadronization cannot be obtained easily by solving the Lagrangian. One of the popular models for hadronization is the Lund string model [23]. Initially a quark-pair is in color neutral state. Color force carried by gluon is modeled as a narrow tube (string) connecting two quarks, with force constant $\kappa \approx 1\,\mathrm{GeV/fm} \sim 0.2\,\mathrm{GeV}^2$. As the quarks move apart, the force becomes stronger and pull them back together like a horizontal spring pendulum. The phase space of the Lund model is a two-dimensional space-time (i.e. evolution of distance between quarks in time). At any moment, the string has a probability $\sim \exp(-m^2/\kappa)$ to break into two qq pairs, each quark takes part of string energy. The process repeats until kinematic cutoff is reached. This process is implemented in PYTHIA [24], which are widely used in experimental high energy physics. Since hadronization is a process based on QCD phenomenon, the parameters are tuned by experimental measurements.

Chapter 2

Theory II: Black Holes

The behavior of light near a dense and massive object was studied by J. Michell [25] in 1783. Suppose there is a massive spherical star with mass M and radius R. By Newtonian mechanics, in order to an object with mass (m) to escape from the star's surface, the object must carries enough kinetic energy (i.e. a minimum velocity v_{escape}) to compensate the potential energy by gravitational attraction:

$$\frac{1}{2}mv_{\text{escape}}^2 = G\frac{Mm}{R} \text{ (SI units).}$$

Michell proposed that if the planet is massive and dense enough, even light cannot escape from it. Independently, same conclusion was mentioned by Pierre-Simon Laplace in 1795. The idea has not be further developed until 1916, when A. Einstein published his theory of general relativity [26].

2.1 Classical Black Hole

The theory of general relativity describes the fundamental interaction of gravitation using a geometric curvature of spacetime created by energy and matter, formulated as Einstein field equations:

$$R_{\mu\nu} - \frac{1}{2} g_{\mu\nu} R = 8\pi T_{\mu\nu},$$

where $R_{\mu\nu}$ is the Ricci curvature tensor, R is the scalar curvature, $g_{\mu\nu}$ is the metric tensor, and $T_{\mu\nu}$ is the stress-energy tensor. All terms from the left hand side are pure geometric properties of spacetime, while the right hand side terms are physics results of the gravitational interaction. Soon after Einstein's publication, K. Schwarzschild found the first non-trivial exact solution of the Einstein field equations, which describes a spherical, non-rotating, and uncharged object [27].

2.1.1 Schwarzschild Black Hole

Let M be the mass of a spherical, non-rotating, and uncharged object. In spherical coordinates, with the origin at the center of the object, the solution of Einstein field equations is expressed in Schwarzschild metric [27]:

$$ds^2 = -\left(1 - \frac{2M}{r}\right) dt^2 + \left(1 - \frac{2M}{r}\right)^{-1} dr^2 + r^2 d\Omega^2, \tag{2.1}$$

where Ω is the solid angle of a 2-sphere. Since there is spherical symmetry, a particle follow radial timelike geodesic, i.e. trajectory of the particle can be expressed in r-

coordinate only ($d\Omega = 0$), and $ds^2 = -d\tau^2$ for proper-time τ. Equation 2.1 becomes

$$ds^2 = \left[-\left(1 - \frac{2M}{r}\right) + \left(1 - \frac{2M}{r}\right)^{-1} \left(\frac{dr}{dt}\right)^2 \right] dt^2.$$

On the other hand, the energy density is given by

$$E = -g_{00}\frac{dt}{d\tau} = \left(1 - \frac{2M}{r}\right)\frac{dt}{d\tau},$$

which implies that the velocity of the particle from a far observer time frame is

$$\left(\frac{dr}{dt}\right)^2 = -\frac{1}{E^2}\left(1 - \frac{2M}{r}\right)\left(1 - E^2 - \frac{2M}{r}\right), \tag{2.2}$$

and the velocity of the particle in the proper-time frame is

$$\left(\frac{dr}{d\tau}\right)^2 = -\left(1 - E^2 - \frac{2M}{r}\right). \tag{2.3}$$

Clearly if $E > 1$, the particle is unbounded by gravitational force, and therefore the mass does not form a black hole. Only in-falling particle $E \leq 1$ ($E = 1$ represents a particle at rest at $r = \infty$) is considered. Define $r_0 = \frac{2M}{1-E^2}$ and Schwarzschild radius $r_s = 2M$. Figure. 2.1 shows the particle starts falling at r_0 in the proper-time frame, i.e. observer travels along with the particle. In the proper-time frame, the object (or star) begins to collapse at r_0. However, a far observer would see the star collapses at Schwarzschild radius r_s.

In order to investigate the behavior near Schwarzschild radius, a new coordinate is defined as $r = r_s + \epsilon$. Furthermore, setting $E = 1$ to simplify the calculation, Equation. 2.2 gives

$$dt = -\frac{(r_s+\epsilon)^{3/2}}{r_s^{1/2}\epsilon}d\epsilon.$$

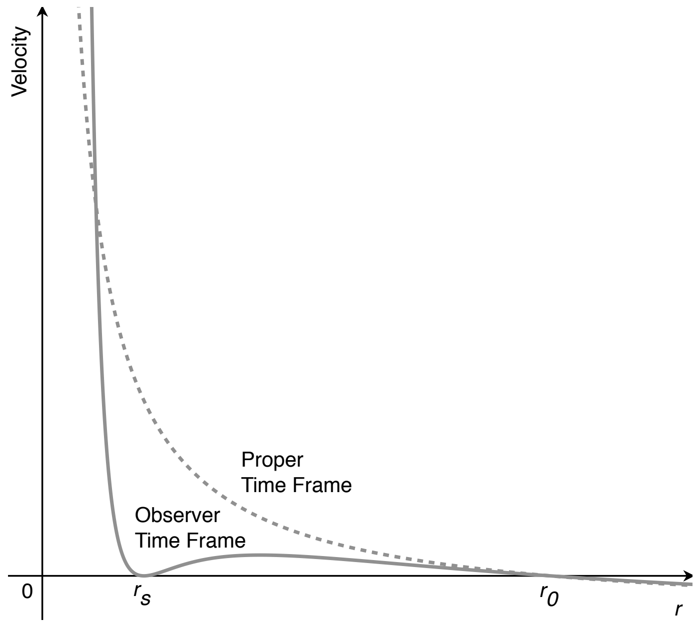

Figure 2.1: Velocity of an in-falling particle in the observer and the proper-time frames.

The trajectory of the particle can be obtained by integrating the above differential equation with initial conditions $\tau = t = 0$ and placing the particle outside the Schwarzschild radius $\epsilon(t = 0) > 0$. However, when the particle approaches to the Schwarzschild radius, i.e. $\epsilon \to 0$, the integral $\int dt$ diverges logarithmically as $dt \to 1/\epsilon$. In a far observer's view, the particle never crosses the Schwarzschild radius as it takes infinite time to approach there. (Fig. 2.2). This phenomenon can be explained by considering the shape of a lightcone (setting $ds^2 = 0$ in Equation 2.1) along the trajectory:

$$\frac{dr}{dt} = \pm \left(1 - \frac{r_s}{r}\right).$$

When $r \to r_s$, the slopes of the lightcone turn vertical and the area of the timelike regions become zero. Since all signals, including light, must travel within the timelike regions of the lightcone, a far observer would not receive any signal when the particle reaches r_s. The surface at Schwarzschild radius where spacetime disjoints, is known as event horizon. There is no divergence for solving Equation 2.3 in the proper-time frame. It takes a finite amount of time for a particle to cross the event horizon

(Fig. 2.2), since an observer in the proper-time frame is traveling along with the particle.

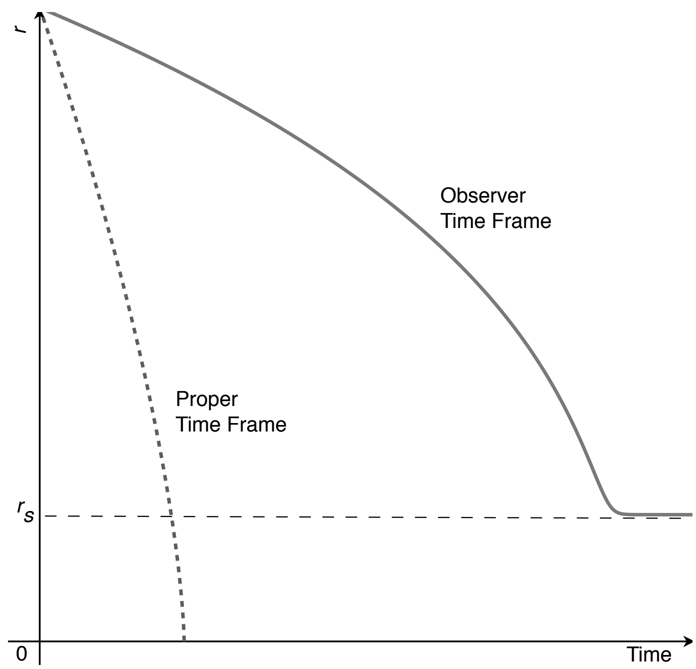

Figure 2.2: Trajectory of a in-falling particle in far observer and proper-time frame.

The object followed by Schwarzschild solution of Einstein field equations is called (Schwarzschild) black hole. The size of black hole is defined as Schwarzschild radius (r_s). According to the Birhoff's Theorem [28], Schwarzschild metric is the unique spherically systematic solution to Einstein field equations. Hence, the Schwarzschild black hole is the only model for a non-rotating, uncharged, and spherical black hole.

2.1.2 Hawking Radiation

Once a black hole is formed, it starts growing as gravity attracts mass toward center of the black hole, and nothing can escape beyond the event horizon. In 1974, S. Hawking proposed that black hole does radiate thermally with a black body spectrum [4], right after a prediction by J. Bekenstein that black hole has finite non-zero temperature and entropy [29]. According to the Heisenberg uncertainty principle [30], vacuum fluctuation allows virtual particle-antiparticle pairs creation near the event horizon. The particle just beyond the event horizon gets boosted and escapes, while its partner is pulled back to the black hole by strong gravitational attraction. As a result, the black hole loses energy through radiation. This process is known as Hawking radiation, or Bekenstein-Hawking radiation.

The emission process of black hole evaporation is characterized by its temperature, Hawking temperature or sometimes Hawking-Unruh temperature, derived independently by Hawking [31] and William George Unruh [32].

Consider a new coordinate system near event horizon,

$$r = r_s + \frac{\rho^2}{8M} = 2M + \frac{\rho^2}{8M},$$

and define $\kappa = \frac{1}{2M}$,

$$\begin{aligned} dr^2 &= (\kappa\rho)^2 d\rho^2, \\ 1 - \frac{2M}{r} &= \frac{(\kappa\rho)^2}{1 + (\kappa\rho)^2} \\ &\approx (\kappa\rho)^2 \text{ as } \rho \to 0. \end{aligned}$$

The Schwarzschild metric in Equation 2.1, assuming spherical solution in vacuum without pressure ($d\Omega = 0$), can be expressed near event horizon as

$$ds^2 = -(\kappa\rho)^2 dt^2 + d\rho^2, \tag{2.4}$$

which known as the Rindler coordinates. Applying The Wick rotation to transform the real time to the imaginary time $t' = it$, Equation 2.4 becomes

$$ds^2 = \rho^2 \kappa^2 dt'^2 + d\rho^2. \tag{2.5}$$

Since ds^2 is an invariant quantity, image of Equation 2.5 in $(\rho, \kappa t')$ can be identified as a circle in two-dimensional Euclidean space using polar coordinates, where the period of t' is $2\pi/\kappa$. Quantization of field $\Phi(\rho, t')$ near event horizon under periodic boundary condition $\Phi(\rho, t') = \Phi(\rho, t' + 2\pi/\kappa)$ gives the partition function

$$\mathcal{Z} = \int \mathcal{D}\Phi e^{-S[\Phi]} \sim e^{-\oint H dt'},$$

where $S[\Phi]$ is the action in Euclidean space, and H is the Hamiltonian of the system. On the other hand, the partition function of a system in temperature T can be calculated by statistical mechanics

$$\mathcal{Z} = Tr\left(e^{-\beta H}\right),$$

where $\beta = 1/T$. For a black hole in thermal equilibrium at Hawking temperature T_H, there is a connection between field theory and statistical mechanics, such that

$$\begin{aligned} \beta &= \frac{2\pi}{\kappa} \\ \Longrightarrow T_H &= \frac{1}{8\pi M}. \end{aligned}$$

Since black hole evaporation follows black body spectrum, power of energy radiated is given by Stefan-Boltzmann law

$$P = \sigma A T_H^4,$$

where σ is Stefan-Boltzmann constant, and $A = \pi r_s^2$ is the area of black hole. The lifetime, defined as total time required for a black hole to lose all its mass:

$$\begin{aligned} t_{\mathrm{BH}} &= \int_0^{t_{\mathrm{BH}}} dt \\ &= -\int_M^0 P dM \\ &\approx \left(\frac{M}{M_\odot}\right)^3 \times 10^{66} \text{ years.} \end{aligned}$$

Hawking temperature is inversely proportional to mass, and lifetime increase with mass. This implies black hole with smaller mass is hotter and evaporate faster.

2.1.3 Rotating Black Hole and Others

The non-rotating spherical black hole described by Schwarzschild is too idealistic, as most of the astronomical objects do spin by nature. The rotating and uncharged solution of Einstein field equations was found by Kerr [33], known as Kerr black hole.

For an object with mass M and angular momentum J, Kerr solution is written in Boyer-Lindquist coordinates (r, θ, ϕ). The transformation to Cartesian coordinates are

$$\begin{aligned} x &= \sqrt{(r^2 + a^2)} \sin\theta \cos\phi, \\ y &= \sqrt{(r^2 + a^2)} \sin\theta \sin\phi, \\ z &= r\cos\theta, \end{aligned}$$

where $a = J/M$ is the angular momentum per unit mass. The Kerr metric is

$$\begin{aligned} ds^2 &= -\left(1 - \frac{2Mr}{\Sigma}\right) dt^2 + \frac{\Sigma}{\Delta} dr^2 + \Sigma d\theta^2 \\ &\quad + \frac{(r^2 + a^2)^2 - a^2 \Delta \sin^2\theta}{\Sigma} \sin^2\theta d\phi^2 - \frac{4Mar\sin^2\theta}{\Sigma} dt d\phi, \end{aligned} \tag{2.6}$$

where $\Delta = r^2 - 2Mr + a^2$ and $\Sigma = r^2 + a^2\cos^2\theta$. Note that Schwarzschild metric is a special solution of Kerr metric when $a = 0$, i.e. zero angular momentum. The Kerr metric is not invariant under $\phi \to -\phi$. However, it is symmetric about the rotation axis $\theta \to -\theta$.

Event horizon can be found at the singularity of the radial coordinate, i.e. $g_{rr} \to \infty$ or $\Sigma = 0$. There are two solutions:

$$r_\pm = M \pm \sqrt{(M^2 - a^2)}, \tag{2.7}$$

namely outer (r_+) and inner (r_-) horizons. Outer horizon is considered as the event horizon of the black hole. The size of the rotating black hole is smaller than the non-rotating one with same mass since $r_+ \leq 2M = r_s$ for $a \geq 0$. Equation 2.7 does not have solution if $a > M$ (no rotating black hole is formed), which implies that the angular momentum for a rotating black hole is bounded by $J \leq M^2$.

Another special property of rotating black hole, which does not appear in the Schwarzschild black hole, is the ergosphere, a surface corresponding to $g_{tt} = 0$:

$$r = M + \sqrt{M^2 - a^2\cos^2\theta}.$$

The ergosphere is an ellipsoid, which intercepts the event horizon at $\theta = 0$. Another solution of $g_{tt} = 0$, which lies inside event horizon is not relevant in this discussion.

The volume between the ergosphere and the event horizon is called ergoregion, where t is spacelike ($g_{tt} > 0$). Any particles inside that region must co-rotate with the black hole, in order to maintain a timelike trajectory. Consider a far observer looking at a fixed r and θ, the angular velocity is defined as

$$\Omega = \frac{d\phi}{dt} = \frac{d\phi/d\tau}{dt/d\tau}.$$

Let $ds^2 = -d\tau^2$, and $d\theta = dr = 0$, the Kerr metric (Eq. 2.6) is simplified to

$$ds^2 = g_{tt}dt^2 + g_{\phi\phi}d\phi^2 + 2g_{t\phi}dtd\phi = -d\tau^2.$$

In terms of the angular velocity Ω, it is written as

$$-\left(\frac{d\tau}{dt}\right)^2 = g_{tt} + 2g_{t\phi}\Omega + g_{\phi\phi}\Omega^2,$$

which implies $g_{tt} + 2g_{t\phi}\Omega + g_{\phi\phi}\Omega^2 < 0$. Inside the ergoregion, the angular velocity observed from a far rest frame cannot be zero as $g_{tt} > 0$, and Ω is constrained in a range of

$$0 < \Omega_- < \Omega < \Omega_+,$$

where

$$\begin{aligned}
\Omega_\pm &= -\frac{g_{t\phi}}{g_{\phi\phi}} \pm \sqrt{\left(\frac{g_{t\phi}}{g_{\phi\phi}}\right)^2 - \frac{g_{tt}}{g_{\phi\phi}}} \\
&= \omega \pm \sqrt{\omega^2 - \frac{g_{tt}}{g_{\phi\phi}}}, \\
\omega &= -\frac{g_{t\phi}}{g_{\phi\phi}} \\
&= \frac{2Mar}{(r^2+a^2)^2 - a^2\Delta\sin^2\theta}.
\end{aligned}$$

Note that Ω_- increases with decreasing r inside the ergoregion, and $\Omega_- = 0$ at the ergosphere. There is no stationary observer for the non-rotating black hole, and the effect is known as frame-dragging. Since the ergoregion is beyond the event horizon, particles in that region can decay, escape, and extract energy and angular momentum from the black hole. The process of energy extraction was studied by Penrose [34], known as Penrose process. The upper bound of energy fraction extracted from Penrose process was calculated by Christodoulou [35].

The solution of charged black hole is given by the Kerr-Newman metric [36] in Boyer-Lindquist coordinates:

$$\begin{aligned} ds^2 &= -\frac{\Delta - a^2\sin^2\theta}{\Sigma}dt^2 - \frac{2a(r^2+a^2-\Delta)\sin^2\theta}{\Sigma}dtd\phi \\ &+ \frac{(r^2+a^2)^2 - a^2\Delta\sin^2\theta}{\Sigma}\sin^2\theta d\phi^2 + \frac{\Sigma}{\Delta}dr^2 + \Sigma d\theta^2, \end{aligned}$$

where $\Sigma = r^2 + a^2\cos^2\theta$, $\Delta = r^2 - 2Mr + a^2 + Q^2$, and Q is the electric charge. The non-zero components of the electromagnetic potentials are

$$\begin{aligned} A_t &= -\frac{Qr}{\Sigma}, \\ A_\phi &= \frac{Qar\sin\theta}{\Sigma}. \end{aligned}$$

When the electric charge is zero ($Q = 0$), the Kerr-Newman metric reduces to the Kerr metric. The uniqueness of the Kerr-Newman solution for a charged rotating black hole was proved by Pawel O. Mazur [37]. On the way of studying different solutions for black hole, a series of black hole uniqueness theorems were proved by Israel (1967,1968) [38, 39], Carter (1971) [40], Robinson (1974,1975) [41, 42] and Mazur (1982) [37], which leads to the remarkable "no-hair theorem", named after a quote from Misner, Thorne, and Wheeler [43]:

A black hole has no "hair".

The no-hair theorem states that a black hole is completely characterized by three parameters: mass (M), angular momentum (J) and electric charge (Q). [1] No matter how complicated the initial state is, all properties (hairs) except the three characteristic parameters are thrown away during black hole formation.

2.2 Microscopic Black Hole

Microscopic black hole, or mini black hole, refers to the TeV-scale black hole in a scale of 10^{-4} fm, produced in collider experiment. This Section gives a review on the theory, production and simulation of microscopic black hole.

2.2.1 Large Extra Dimensions

Gravity is often ignored in particle physics, since Planck scale $M_{\mathrm{Pl}} \sim 10^{16}\,\mathrm{TeV}$ is much higher than standard model scale, while the electroweak scale is in the order of TeV. The strength of gravity is negligibly small comparing to strong or electroweak interactions. The huge difference between Planck and standard model scale, called the hierarchy problem, is an unsolved problem in modern physics.

A possible explanations was proposed by Arkani-Hamed, Dimopoulos, and Dvali [3, 44] or ADD model, assuming the existence of large (compared to the inverse Planck scale) extra spatial dimensions. The extra spatial dimensions are compactified: a dimensional reduction technique by imposing periodic boundary conditions, to ensure all physics laws are still valid in four-dimensional space-time. The idea of compact-

[1] Magnetic monopole charge P, if exists, can be included in Kerr-Newman metric as an effective charge $e = \sqrt{P^2 + Q^2}$.

ification can be demonstrated by considering a fifth dimension (x^5), such that any field $\Phi(x^\mu, x^5)$ is invariant under coordinate transformation $x^5 \rightarrow x^5 + 2\pi R$, where R is interpreted as the size of the extra dimension. Visually, x^5 coordinate is winding up in a circle of radius R. The field $\Phi(x^\mu, x^5)$ then can be expanded as a Fourier series, i.e. superposition of normal modes:

$$\Phi(x^\mu, x^5) = \sum_{n=-\infty}^{\infty} \phi^{(n)}(x^\mu) e^{-i\frac{nx^5}{R}},$$

where the Fourier coefficients $\phi^n(x^\mu)$ depend only on x^μ coordinates, representing physics laws in usual 4-dimensional space-time. This special case of 5-dimensional model is known as Kaluza-Klein theory, originally attempted to unify gravity and electromagnetic interaction by Kaluza [45] and Klein [46].

In general, the extra spatial dimensions are compactified in a n-dimensional sphere or a torus in a size of R with $R > M_{\mathrm{Pl}}$. Let M_{D} be a new fundamental scale for gravitational interaction in $(n+4)$-dimensional space-time. By Gauss's law, the gravitational potential can be written as

$$V(r) \sim \frac{1}{{M_{\mathrm{D}}}^{n+2} r^{n-1}}.$$

At large distance $r > R$, the above equation is asymptotically equivalent to Newton's law of gravity

$$V(r) \sim \frac{1}{{M_{\mathrm{Pl}}}^2 r},$$

which gives the relation ${M_{\mathrm{Pl}}}^2 \sim {M_{\mathrm{D}}}^{n+2} R^n$. In this dissertation, Planck scale in extra dimensions (M_{D}) is expressed in Particle Data Group (PDG) definition [16]:

$${M_{\mathrm{Pl}}}^2 = 8\pi R^n {M_{\mathrm{D}}}^{n+2}.$$

The "apparent" Planck scale (M_{Pl}) is enlarged by the size of extra dimension, whereas the "true" Planck scale in extra dimensions (M_{D}) might be essentially very small, even in a few TeV-scale, depending on the size of extra dimensions (Table 2.1).

Table 2.1: Number of extra dimensions n and the corresponding size of extra dimensions R for $M_{\mathrm{D}} = 1\,\mathrm{TeV}$.

n	R (m)
1	$\sim 10^{11}$
2	$\sim 10^{-4}$
3	$\sim 10^{-9}$
7	$\sim 10^{-15}$

Various experiments were done to test Newton's law of gravity at short range, by comparing measurements to the Yukawa potential [47, 48, 49, 50, 51, 52, 53, 54]

$$V(r) = V_0(r)[1 + \alpha \exp(-r/\lambda)],$$

where $V_0(r)$ is the Newton's gravitational potential, α is relative strength of extra interaction, and λ is the length scale of the Yukawa potential. Figure 2.3 shows the excluded region, where Newton's law of gravity is violated at 95% confidence level based on these measurements. Since most area of length scale under 10^{-4} m is not covered by the excluded region, the ADD model might hold for number of extra dimension $n > 2$ at $M_{\mathrm{D}} = 1\,\mathrm{TeV}$ (Table 2.1). As a result, M_{D} could be as low as a few TeV, comparable to the electroweak scale, and the effect of gravity is no longer negligible.

2.2.2 Microscopic Black Hole at LHC

A direct consequence of inclusion of the gravitational interaction in particle physics is the possibility of black hole production, as predicted by the solution of Einstein field

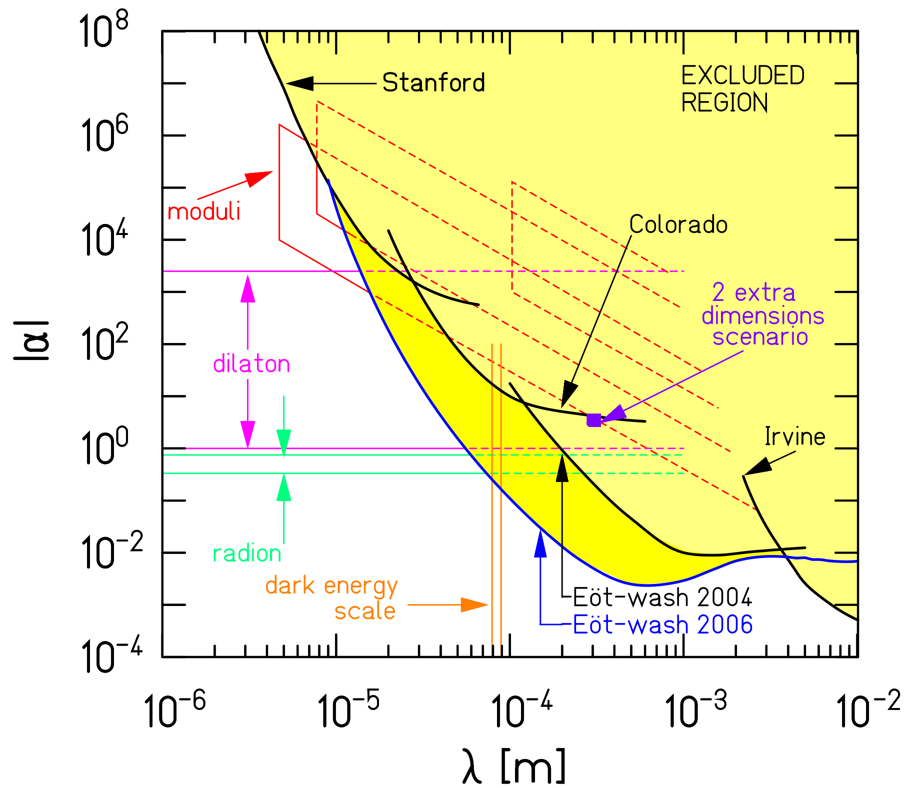

Figure 2.3: Constraints on Yukawa violations of Newton's law of gravity [54]. Shaded region is excluded at the 95% confidence level.

equations. Up to now, since there is no unified theory for gravity and the standard model, the microscopic black hole is modeled as a semi-classical object: formation and physical properties are similar to classical black hole, while quantum effects at small scale are considered. The black hole production at LHC and its possible observations were predicted by Dimopoulos and Landsberg [1], as well as Giddings and Thomas [2].

Solutions of Einstein field equations in higher dimensions were studied by Meyer and Perry [55]. For the simplest case of a non-rotating and uncharged black hole with mass M_{BH} in $n+4$ dimensions, the corresponding Schwarzschild metric is given by Tangherlini [56] as

$$ds^2 = -f(r)dt^2 + f(r)^{-1}dr^2 + r^2 d\Omega_{n+1}^2,$$

where Ω_{n+1} is a $(n+1)$-sphere and $f(r)$ is expressed in terms of the Schwarzschild radius r_s in extra dimensions:

$$\begin{aligned} r_s &= \frac{1}{\sqrt{\pi}M_{\mathrm{D}}}\left[\frac{M_{\mathrm{BH}}}{M_{\mathrm{D}}}\frac{8\Gamma(\frac{n+3}{2})}{n+2}\right]^{\frac{1}{n+1}} \\ f(r) &= 1-\left(\frac{r_s}{r}\right)^{n+1}. \end{aligned}$$

Assume that the size of extra dimension is much larger than the Schwarzschild radius ($R \gg r_s$), a black hole is formed if the impact parameter of two colliding partons is within the Schwarzschild radius. The cross section of a black hole produced by colliding two partons (labeled as a, b) with center-of-mass energy $\sqrt{\hat{s}} = M_{\mathrm{BH}}$ is estimated semi-classically,

$$\hat{\sigma}(ab \to \mathrm{BH})|_{\hat{s}=M_{\mathrm{BH}}^2} \approx \pi r_s^2.$$

In real proton-proton (pp) collision, the two interacted partons carry only a fraction of total center-of-mass energy. To get the total cross section of black hole production from pp collision, the parton luminosity (L) is calculated [57] from

$$\frac{dL}{dM_{\mathrm{BH}}} = \frac{2M_{\mathrm{BH}}}{s} \sum_{a,b} \int_{M_{\mathrm{BH}}^2/s}^{1} \frac{dx_a}{x_a} f_a(x_a) f_b\left(\frac{M_{\mathrm{BH}}^2}{s x_a}\right),$$

where a, b are combinations of quarks and gluon, and $f_i(x_i)$ is the parton distribution functions (PDF) of the i-th quark/gluon that carrying a momentum fraction x_i. The PDF parameterization from MSTW2008lo68 [58] at various energy scale Q are shown in Fig. 2.4. The parton luminosity of quark-quark, gluon-quark and gluon-gluon interactions are then calculated at 7 TeV center-of-mass energy as a function of the black hole mass(Fig. 2.5) by setting the PDF energy scale to the mass of black hole ($Q^2 = M_{\mathrm{BH}}$). The process is dominated by quark-quark interaction. The differential cross section for process $pp \;\rightarrow\; \mathrm{BH} + X$ is

$$\frac{d}{dM_{\mathrm{BH}}}\sigma(pp \;\rightarrow\; \mathrm{BH} + X) = \frac{dL}{dM_{\mathrm{BH}}}\hat{\sigma}(ab \rightarrow \mathrm{BH})|_{\hat{s}=M_{\mathrm{BH}}^2},$$

and the total cross section of black hole production by LHC is given by integrating M_{BH} from a minimum threshold $M_{\mathrm{BH}}^{\mathrm{min}} > M_{\mathrm{D}}$ to the maximum center-of-mass energy $M_{\mathrm{BH}}^{\mathrm{max}}$ provided by LHC, currently being 7 TeV:

$$\sigma = \int_{M_{\mathrm{BH}}^{\mathrm{min}}}^{M_{\mathrm{BH}}^{\mathrm{max}}} d\sigma(pp \;\rightarrow\; \mathrm{BH} + X).$$

The cross section of black hole production at 7 TeV center-of-mass energy is shown in Figs. 2.6 and 2.7. The total cross section can be as high as 100 pb if the Planck scale in higher dimensions is close to 1 TeV.

Like classical black hole, evaporation of microscopic black hole is governed by the

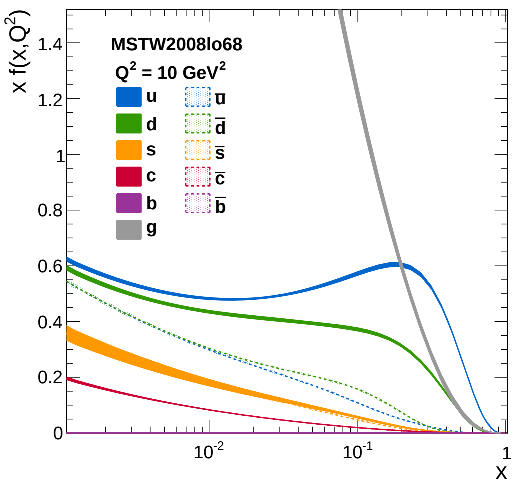

(a) $Q^2 = 10\,\mathrm{GeV}^2$

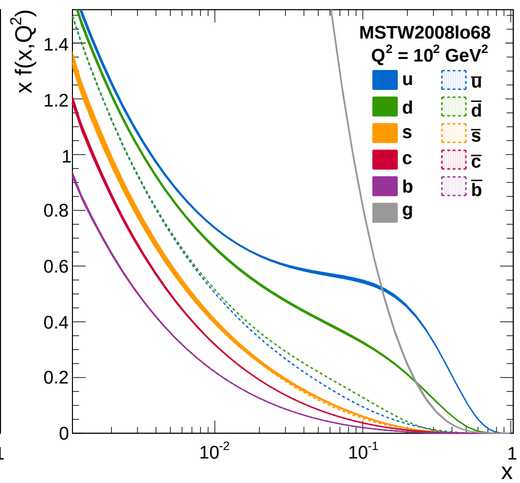

(b) $Q^2 = 10^2\,\mathrm{GeV}^2$

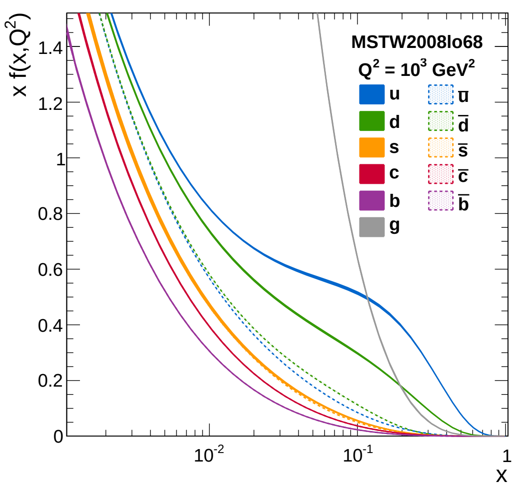

(c) $Q^2 = 10^3\,\mathrm{GeV}^2$

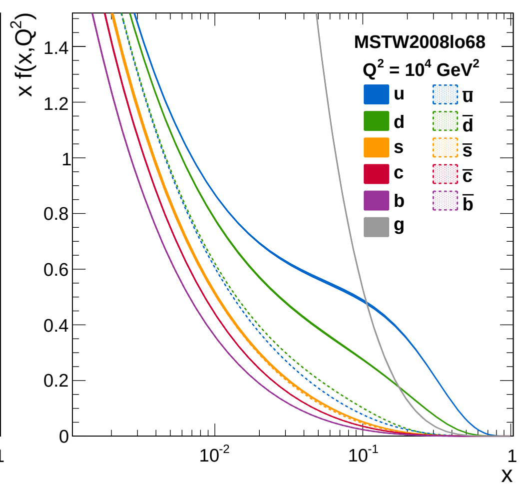

(d) $Q^2 = 10^4\,\mathrm{GeV}^2$

Figure 2.4: Parton distribution functions of MSTW2008lo68 at $Q^2 = 10, 10^2, 10^3, 10^4\,\mathrm{GeV}^2$.

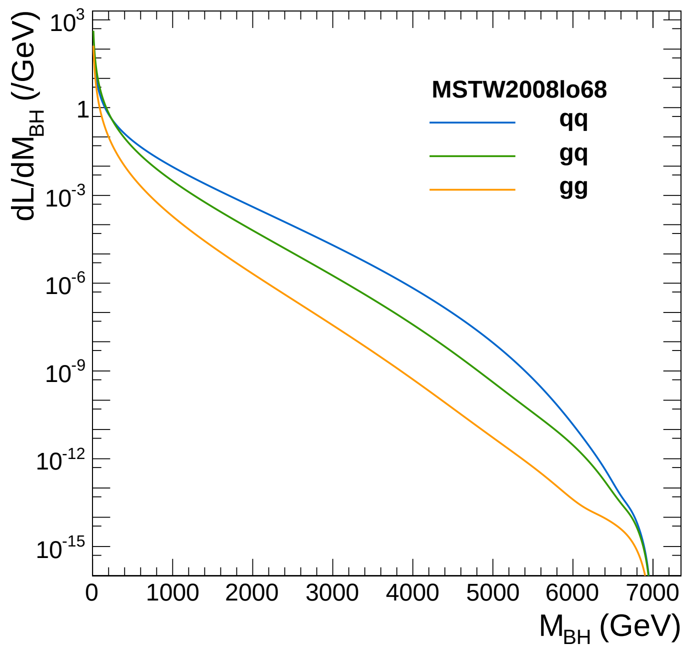

Figure 2.5: Parton luminosity of quark-quark (qq), gluon-quark (gq) and gluon-gluon (gg) interactions at 7 TeV center-of-mass energy as a function of the black hole mass.

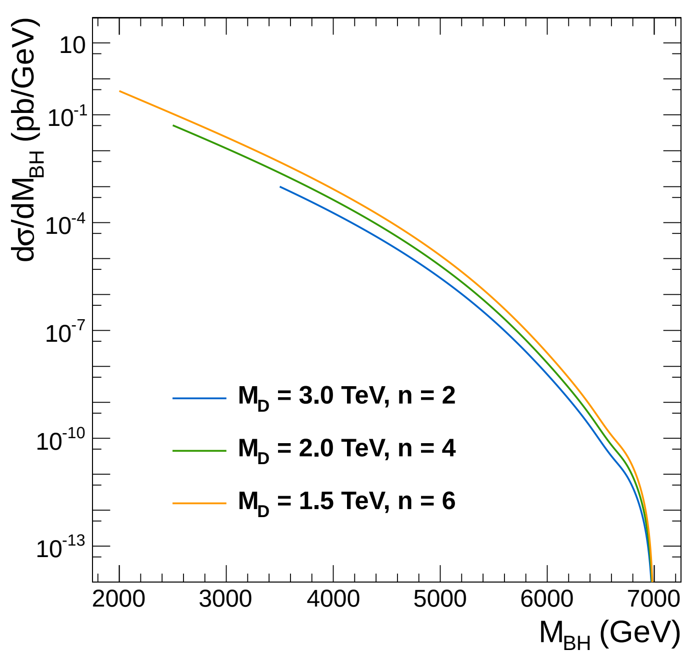

Figure 2.6: Differential cross section of black hole production at 7 TeV collisions.

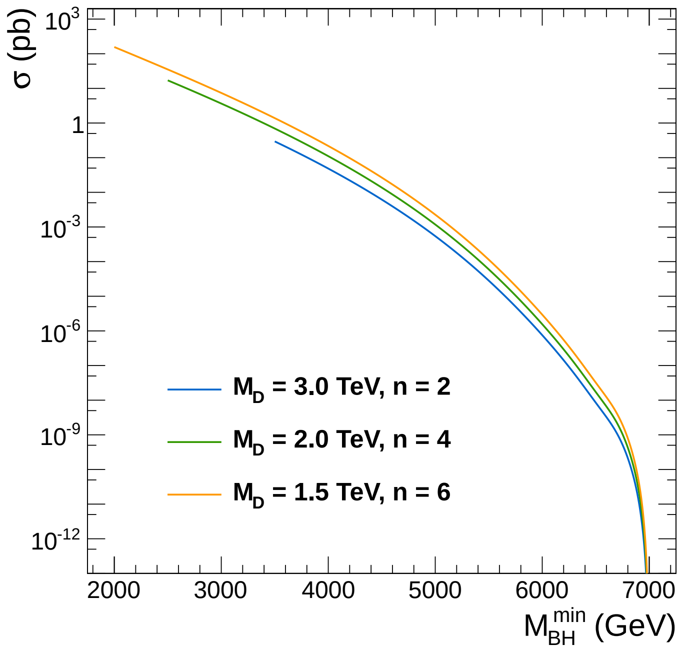

Figure 2.7: Integrated cross section of black hole production with minimum mass threshold ($M_{\rm BH}^{\rm min}$) at 7 TeV collisions.

Hawking temperature in $(4+n)$-dimensional space-time is given by [55]:

$$T_H = \frac{n+1}{4\pi r_s}.$$

As shown in Fig. 2.8, the Hawking temperature of a TeV-scale black hole is in the range of few hundred GeV, corresponding to a very short lifetime 10^{-27} s [59].

Given that the microscopic black hole radiates mainly on the brane (4-dimensional space-time), other than in the bulk ($(4+n)$-dimensions) [60], and gravitons radiated on the brane is suppressed by a factor of $(r_s/R)^n$ [60], decay products are mostly standard model particles in 4-dimensional space-time, which are detectable by collider experiments. The average multiplicity of decay products, using statistical mechanics for black body radiation, is estimated by $\langle N\rangle = \langle M_{\rm BH}/\epsilon\rangle$, where ϵ is the

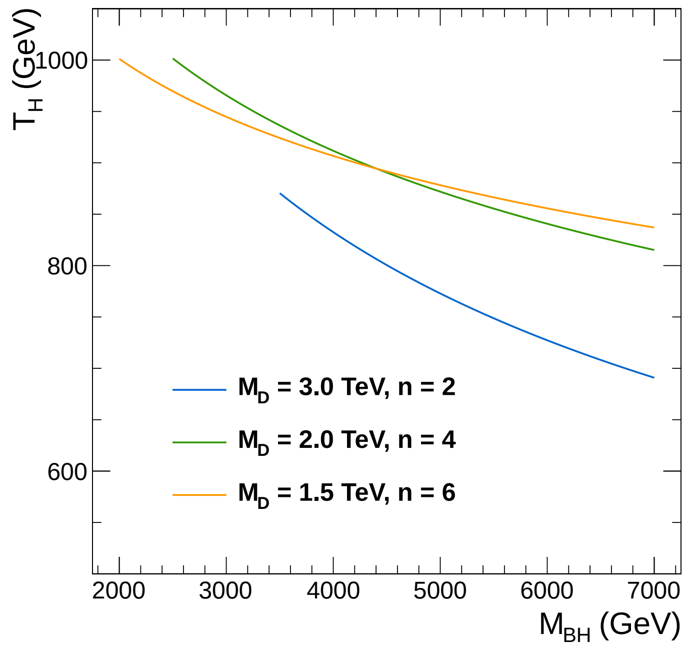

Figure 2.8: Hawking temperature of TeV-scale black hole in various scenarios.

energy spectrum of decay products. The number density is given by

$$n(\epsilon)d\epsilon = \frac{g(\epsilon)d\epsilon}{e^{\beta(\epsilon-\mu)} + c},$$

where $g(\epsilon)$ is the density of states, $\beta = 1/T_H$ is defined at thermal equilibrium, μ is the chemical potential, assumed to be zero, and the constant $c = 0, \pm 1$ for Boltzmann, Fermi-Dirac, and Bose-Einstein statistics respectively. Density of states is $g(\epsilon) \sim \epsilon^2$, since most decay products are on the brane [60]. The expectation value of inverse energy is

$$\begin{aligned} \left\langle \frac{1}{\epsilon} \right\rangle &= \frac{\int_0^\infty d\epsilon \frac{\epsilon}{e^{\beta\epsilon}+c}}{\int_0^\infty d\epsilon \frac{\epsilon^3}{e^{\beta\epsilon}+c}} \\ &= \frac{1}{T_H} \frac{\int_0^\infty dx \frac{x}{e^x+c}}{\int_0^\infty dx \frac{x^3}{e^x+c}} \\ &= \begin{cases} \frac{0.46}{T_H}, c = +1 \\ \\ \frac{1}{2T_H}, c = 0 \\ \\ \frac{0.68}{T_H}, c = -1 \end{cases} . \end{aligned}$$

Roughly, the average multiplicity can be expressed as [1]

$$\begin{aligned} \langle N \rangle &\approx \frac{M_{\mathrm{BH}}}{2T_H} \\ &= \frac{2\sqrt{\pi}}{n+1} \left(\frac{M_{\mathrm{BH}}}{MD} \right)^{\frac{n+2}{n+1}} \left[\frac{8\Gamma\left(\frac{n+3}{2}\right)}{n+2} \right]^{\frac{1}{n+1}} . \end{aligned}$$

The above formula is valid only when $\langle N \rangle \gg 1$. At very low multiplicity, the Planck spectrum is truncated at $E = M_{\mathrm{BH}}/2$ due to the kinematic limit. The multiplicity of decay particles increases with $M_{\mathrm{BH}}/M_{\mathrm{D}}$ as shown in Fig. 2.9. Since Hawking radiation is a thermal process, the decay products are in equal probabilities to all standard model degrees of freedom (democratic decay). Due to the large number of color degrees of freedom, quarks and gluons are the dominant products of black hole evaporation. The remaining are leptons, $W^{\pm}/Z$ bosons, photons, and possibly Higgs bosons and gravitons. Although standard model particles are emitted democratically near the event horizon, the emission spectra are not the same for all types of particles. This is because particles are subjected to a strong gravitational potential near the black hole, each type of particles has different probability to reach the observer, similar to the quantum tunneling effect in alpha decay. The Planck emission spectrum of black body radiation is therefore multiplied by a transmission factor, called the greybody factor, which was calculated numerically for scalar, fermion, and gauge fields with or without rotation at different number of extra dimensions [61, 62, 63, 64, 65, 66, 67]. Note that greybody factor of graviton emitted in rotating black hole is an unresolved problem in general relativity.

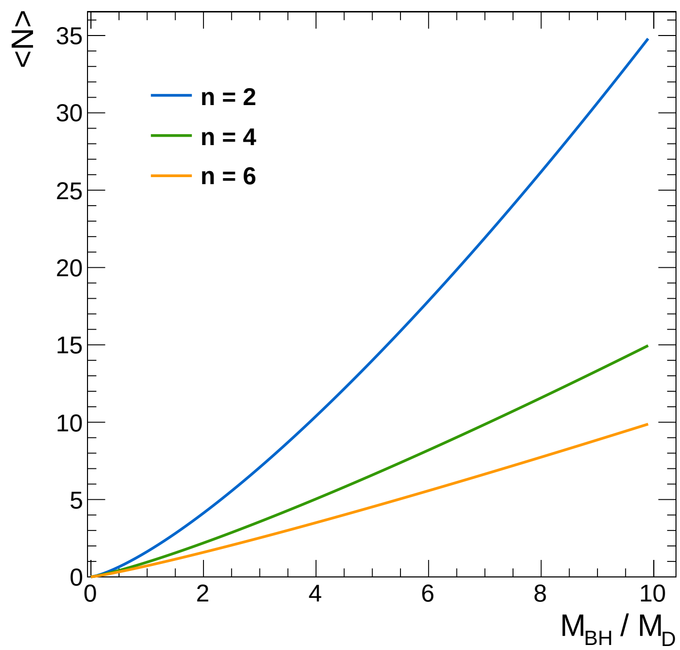

Figure 2.9: Average multiplicity of black hole decay particles as a function of $M_{\mathrm{BH}}/M_{\mathrm{D}}$ for extra dimensions $n = 2, 4, 6$.

Theoretically, all symmetries from standard model $SU_c(3) \times SU_L(2) \times U_Y(1)$, and possibly additional symmetries in bulk space [68], are applied on microscopic black hole evaporation. Therefore, decay products are constrained by the conserved quantities imposed by the symmetries. However, the average multiplicity is usually high, and for simplified simulation, equal probability of each standard model particle is assigned regardless of symmetries.

2.2.3 Cross Section Calculation

The validity of semi-classical approximation for microscopic black hole cross section using $\sigma \approx \pi r_s^2$ was criticized by Voloshin [69, 70], arguing that it should be exponentially suppressed. All later studies [71, 72, 73, 74, 75, 76, 77] show contradictory conclusions, because of an invalid assumption in the original paper [78]. Indeed, enhancement of cross section of black hole production at collider in higher dimension was found by Yoshino and Nambu [74, 75], and further improved by Yoshino and Rychkov [77].

The calculation is based on hoop conjecture, proposed by Thorne [79], stating that an object gets compressed into a black hole, if and only if its circumference in all directions is less than the Schwarzschild circumference, i.e.

$$\frac{C}{2\pi r_s} \leq 1,$$

where C is the minimum length of hoop enclosing all mass. An extension of hoop conjecture to $4+n$ dimensions is stated as follows [80]:

$$\left(\frac{V_{n+1}}{r_s^{n+1}\Omega_{n+1}}\right)^{\frac{1}{n+1}} \leq 1,$$

where V_{n+1} is the minimum hyper-volume in $(n+1)$-dimensions enclosing all masses of the system, and $r_s^{n+1}\Omega_{n+1}$ is the volume of $(n+1)$-sphere calculated by Schwarzschild radius. In 4-dimensional space-time ($n=0$), the above statement is equivalent to the hoop conjecture. Consider a two-particle system with two equal masses m, each of them is modeled as plane-fronted gravitational shock wave with characteristic wavelength $r_s(m)$ by E'Eath and Payne [81, 82, 83]. A black hole of Schwarzschild radius $r_s(2m)$ is formed if two shock waves collide with an impact parameter b. The hyper-volume enclosing two shock waves is an $(n+1)$-ellipsoid with length b in one dimension and $r_s(m)$ in all other dimensions. The volume can be estimated roughly as $V_{n+1} \approx b r_s^n(m)\Omega_{n+1}$. Suppose the higher dimensional version of hoop conjecture holds, i.e.

$$\left[\frac{b r_s^n(m)\Omega_{n+1}}{r_s^{n+1}(2m)\Omega_{n+1}}\right]^{\frac{1}{n+1}} \leq 1,$$

it implies that impact parameter b is bounded from above by the following inequality:

$$\begin{aligned} \frac{b}{r_s(2m)} &\leq \frac{r_s^n(m)}{r_s^n(2m)} \\ &\propto 2^{-\frac{1}{n+1}}. \end{aligned} \tag{2.8}$$

Therefore, the cross section for black hole production in a two-particle system is

$$\begin{aligned} \sigma &= \pi b_{\max}^2 \\ &= F(n)\pi r_s^2, \end{aligned}$$

where $F(n)$ is a dimensional dependent factor improving semi-classical cross section approximation. Numerical studies of two colliding particles were done by Yoshino and Nambu [75], using apparent horizon formation calculation of two shock waves calculated by Eardley and Giddings [73]. Results from simulations are numerically consistent with Equation 2.8 (Fig. 2.10), and the form factors are given in Table 2.2. An improved calculation, by Yoshino and Rychkov [77], shows a 40%-70% increase in black hole production cross section.

n	0	1	2	3	4	5	6	7
$b_{\max}/2r_s(2m)$	0.402	0.480	0.526	0.559	0.583	0.603	0.619	0.632
$F(n)$	0.647	1.084	1.341	1.515	1.642	1.741	1.819	1.883

Table 2.2: Form factor of black hole production cross section, as a function of extra dimensions n, in a two-particle system. Numbers are quoted from Yoshino and Nambu [75].

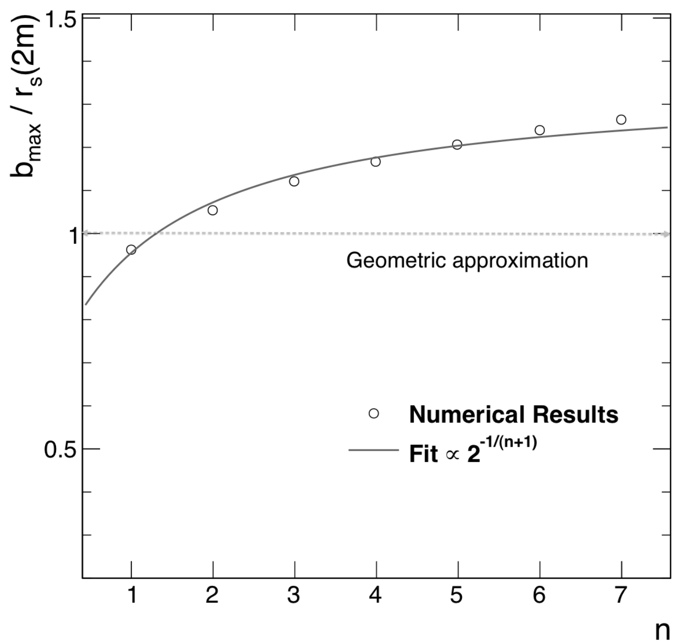

Figure 2.10: Simulated results of maximum impact parameter in unit of Schwarzschild radius. Fitting curve shows power law of $2^{-1/(n+1)}$. Data are obtained from Yoshino and Nambu [75].

2.2.4 Black Hole Generators

The signatures of microscopic black hole evaporation from proton-proton collision with center-of-mass energy of 7 TeV are simulated by BlackMax v2.01.3 [5] and CHARYBDIS 2 v.1.03 [6], using MSTW2008lo68 PDF. General assumptions such as democratic decay of standard model particles and black hole mass beyond Planck scale are discussed in the previous section. No symmetries are imposed except for baryon number conservation, since it is required for proper description of the hadronization process that is used later in detector simulation. Graviton emission is heavily suppressed on brane, and hence excluded from the simulation. Furthermore, the effect of time evolution is ignored. Sudden decay of black hole from its original mass at constant Hawking temperature are assumed. Both generators provide output saved in the Les Houches Event Files [84] (LHE) format, which is a standard XML structure containing information about all particles radiated from a black hole. General properties of microscopic black hole simulation are demonstrated in this section by using LHE outputs from BlackMax and CHARYBDIS. Hadronization and detector simulation results are shown in Analysis Chapter.

Non-rotating and rotating black holes are generated by BlackMax. The average multiplicity of particles from Hawking radiation is given in Fig. 2.11. The properties of decay particles are shown in Figs. 2.12- 2.13 (non-rotating) and Figs. 2.14-2.15 (rotating). Under the Monte Carlo particle numbering scheme (PDG id [16]), particles are labeled as positive numbers, antiparticles negative numbers: quarks (d, u, s, c, b, t) are numbered from 1 to 6; leptons $(e^-, \nu_e, \mu^-, \nu_\mu, \tau^-, \nu_\tau)$ are 11 - 16; gauge bosons (g, γ, Z, W^+, H) are 21 - 25. The variable S_{T} is defined as a scalar sum of the transverse momenta (i.e. the momenta perpendicular to the beam axis) of the decay particles. Note that BlackMax cross section contains a geometric factor similar to Yoshino-Nambu estimation [75] by default, which enhances the semi-classical estimation πr_s^2 by a factor of 1.36, 1.59, and 1.78 for n =2, 4, and 6, respectively. The range of M_{BH} is a few times of M_{D}, and the average multiplicity of black hole radiation is about 3 to 8 varying with the $M_{\mathrm{BH}}/M_{\mathrm{D}}$ ratio (Fig. 2.11). The main difference of black hole evaporation between the non-rotating and rotating scenarios is the emission spectrum. Greybody factors suppress average multiplicity for a rotating black hole (Fig. 2.11b), with higher reduction for $n = 2$ extra dimensions. At very low multiplicity, the emission spectrum is truncated at kinetic limit $M_{\mathrm{BH}}/2$, resulting in two-body decay as shown in Fig. 2.15a. As expected, the decay particles are dominated by quarks and gluons, and are uniform in ϕ.

At the final stage of black hole evaporation, some models predict that black hole stops radiating when its mass reaches M_{D}, forming stable non-interacting and non-accreting remnant (in short, a stable remnant). Since BlackMax does not provide stable remnant simulation, CHARYBDIS generator is used. Option of cross section enhancement factors from Yoshino and Rychkov [77] is applied in CHARYBDIS simulation, on top of the standard calculation πr_s^2. The general properties of decay particles with stable remnant are generated by CHARYBDIS (Figs. 2.16 - 2.17). The stable remnant, with energy close to M_{D} at a few TeV (Fig. 2.18a), does not interact with the detector, and appears as missing energy. The stable remnant, together with neutrinos, are measured by the detector as missing transverse energy. This missing transverse energy is calculated from the vector sum of all transverse momentum from all visible particles. Figure 2.19b shows the distribution of the magnitude of the missing transverse energy ($\not{E}_T$). The mass calculated from all visible particles does not provide good estimation of the generated black hole mass(Fig. 2.19c), as reconstruction of mass depends on the 4-momentum of all particles, which is not completely measured by $\not{E}_T$. In this case, the scalar sum of all visible transverse momentum ($S_{\mathrm{T}}^{\mathrm{visible}}$) and $\not{E}_T$, provides a more robust result (Fig. 2.19d), and therefore plays an important role in searching black hole evaporation signatures.

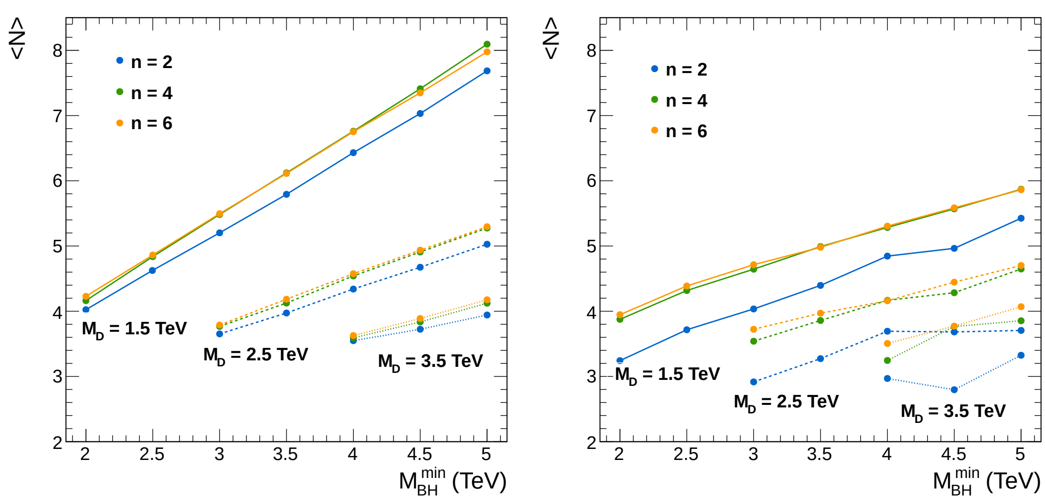

(a) Non-rotating **(b)** Rotating

Figure 2.11: Average multiplicity of particles radiated from black hole simulation by BlackMax.

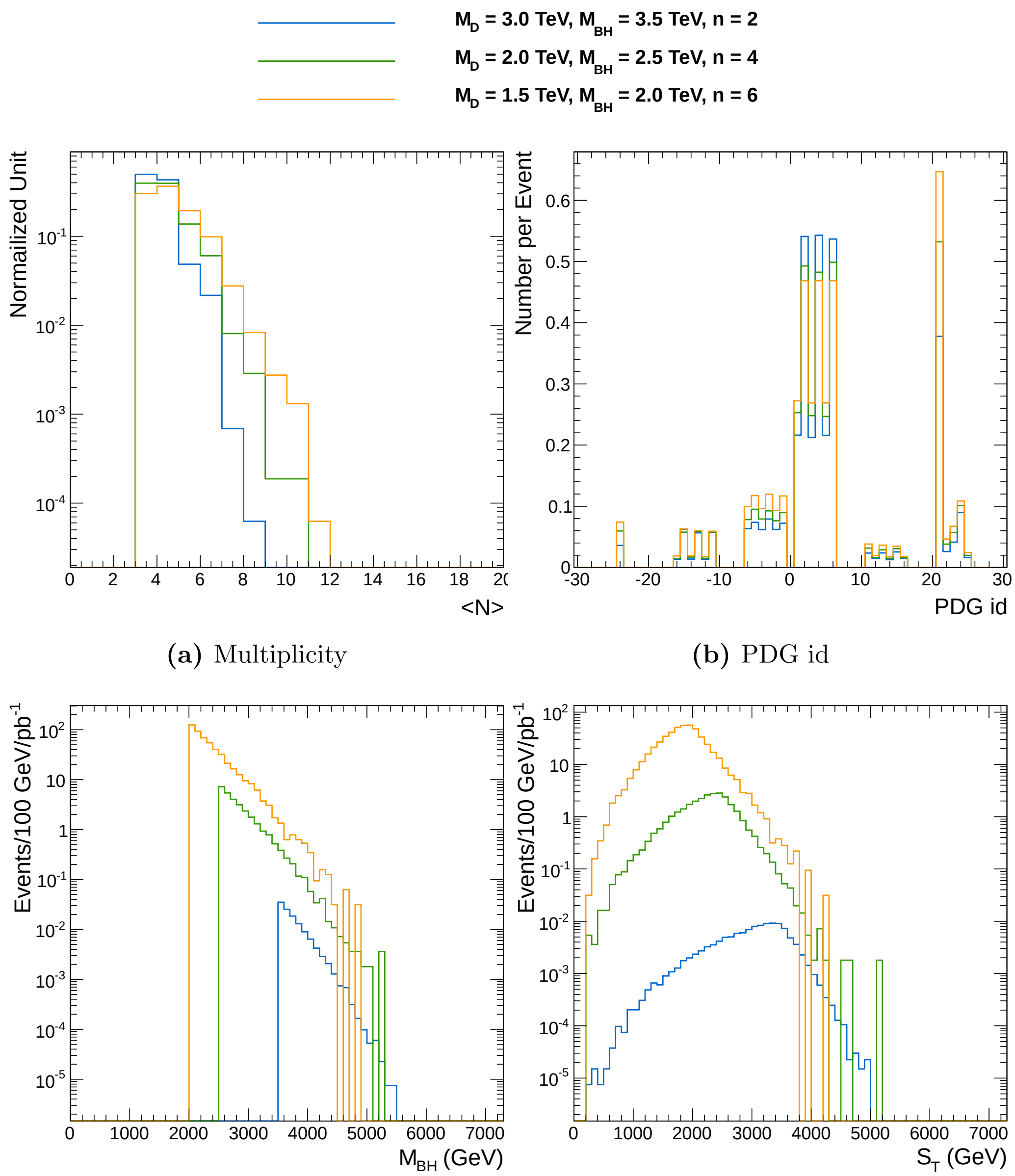

(a) Multiplicity

(b) PDG id

(c) Mass

(d) Scalar p_{T} sum

Figure 2.12: Properties of non-rotating black hole events generated by BlackMax.

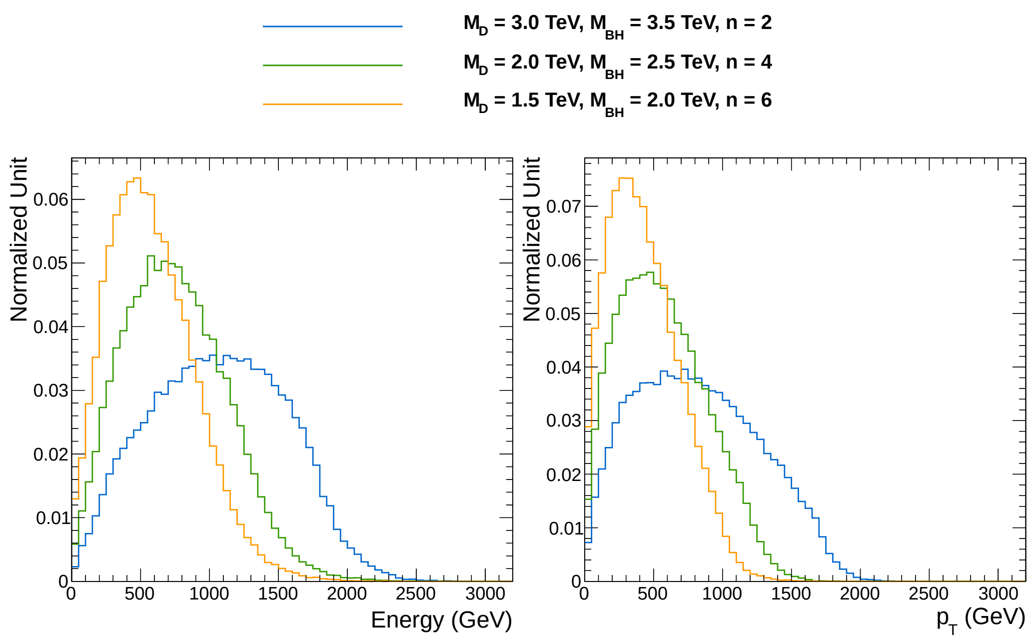

(a) Energy spectrum **(b)** Transverse momentum

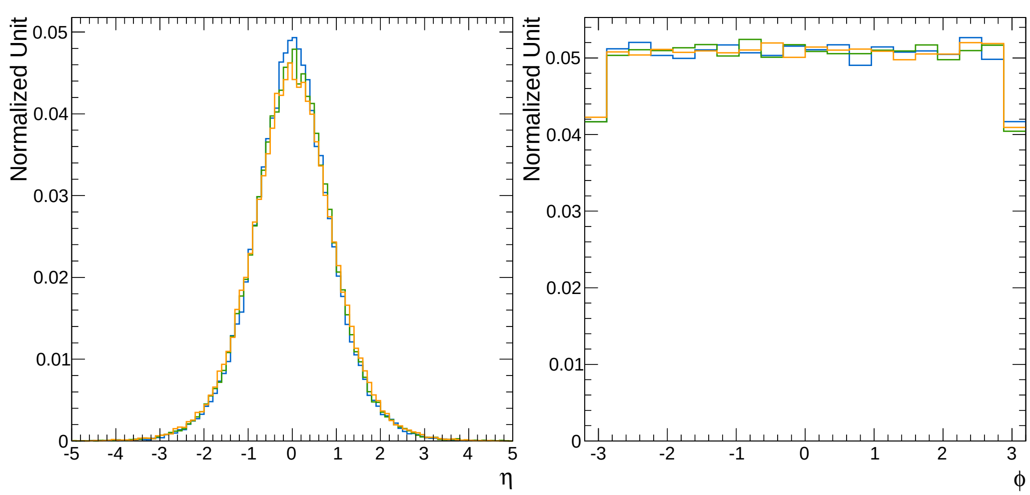

(c) Pseudorapidity **(d)** Azimuthal angle

Figure 2.13: Properties of particles radiated from non-rotating black hole events generated by BlackMax.

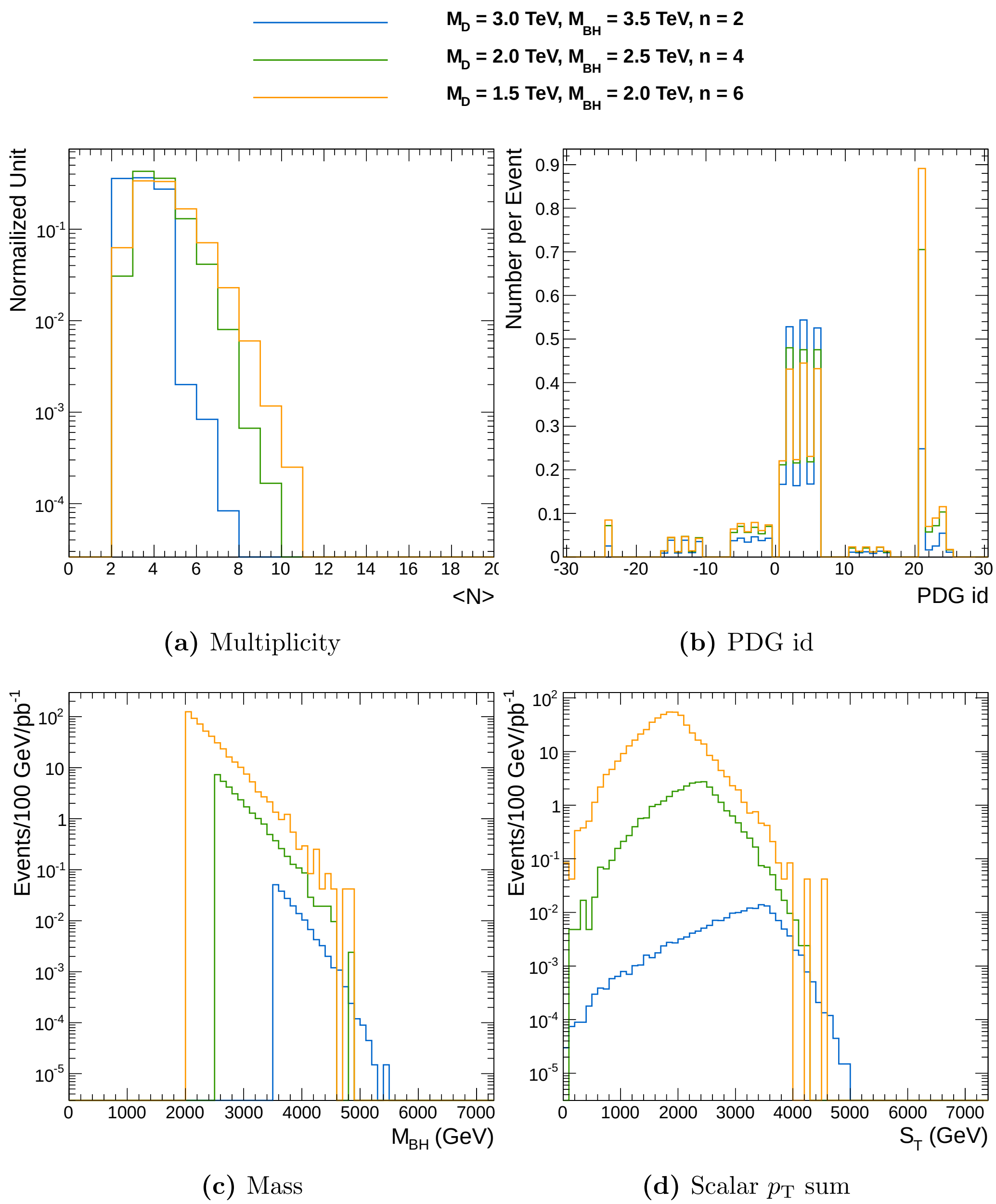

(a) Multiplicity **(b)** PDG id

(c) Mass **(d)** Scalar p_T sum

Figure 2.14: Properties of rotating black hole events generated by BlackMax.

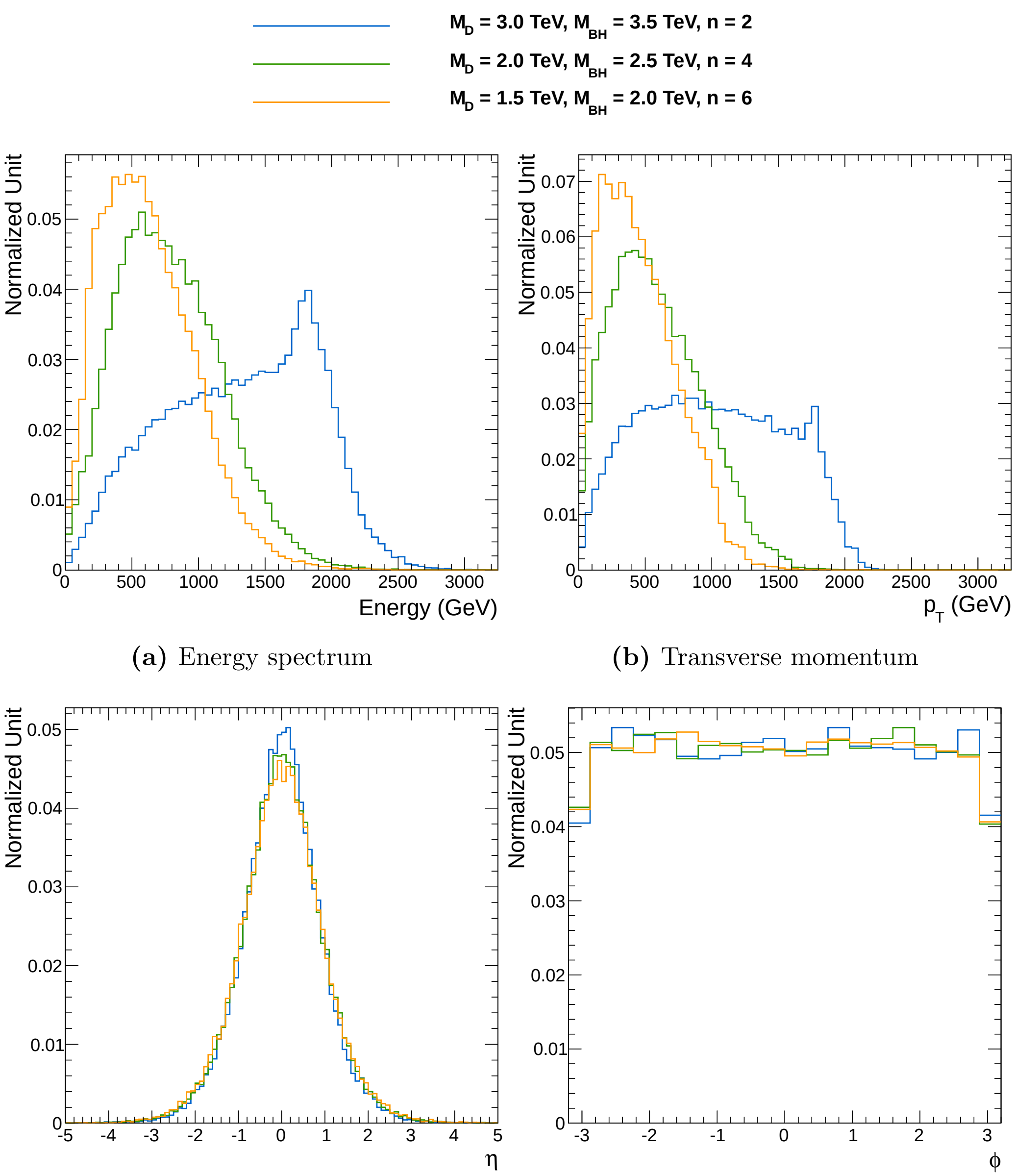

(a) Energy spectrum

(b) Transverse momentum

(c) Pseudorapidity

(d) Azimuthal angle

Figure 2.15: Properties of particles radiated from rotating black hole events generated by BlackMax.

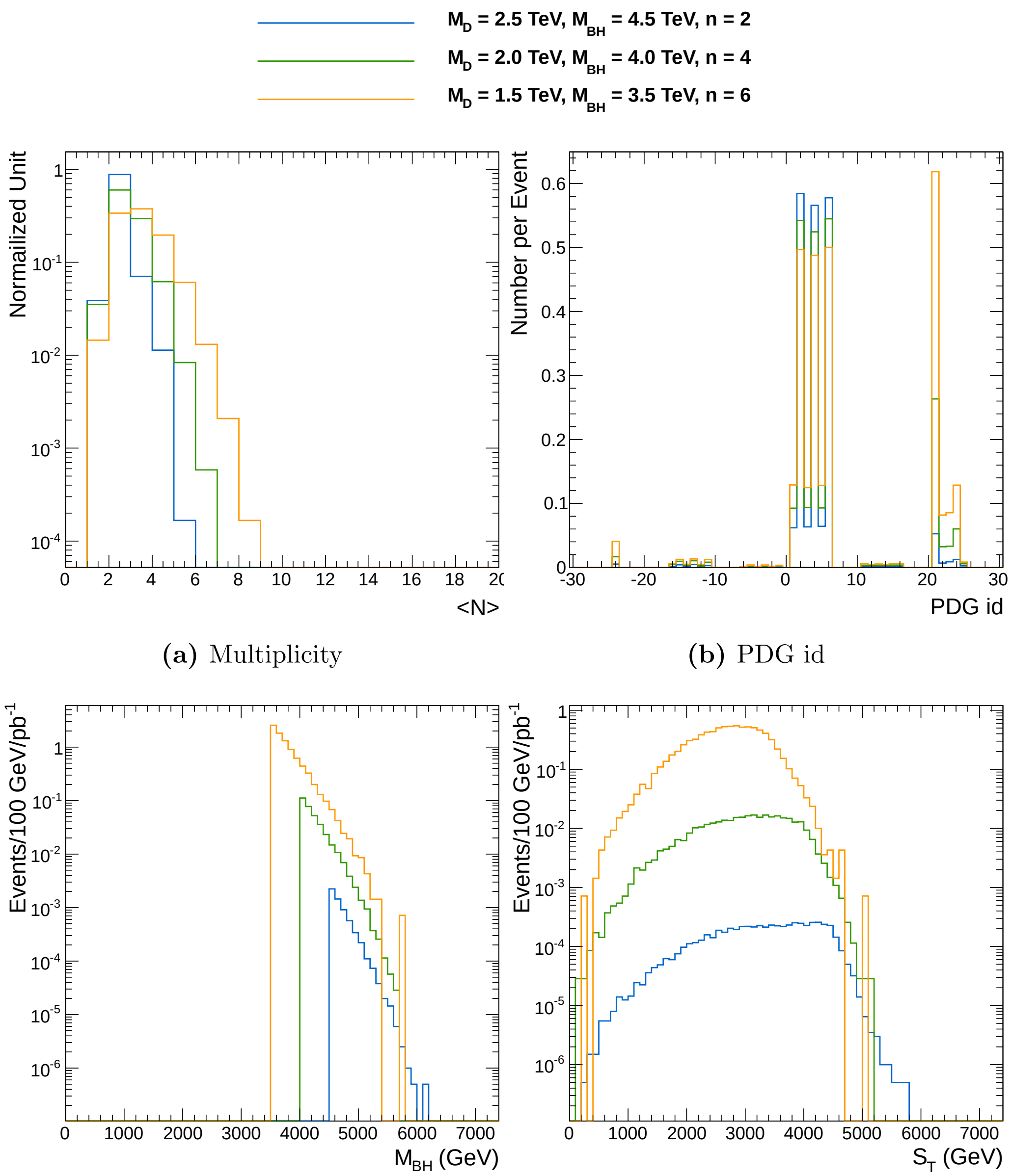

(a) Multiplicity

(b) PDG id

(c) Mass

(d) Scalar p_{T} sum

Figure 2.16: Properties of black hole with stable remnant events generated by CHARYBDIS.

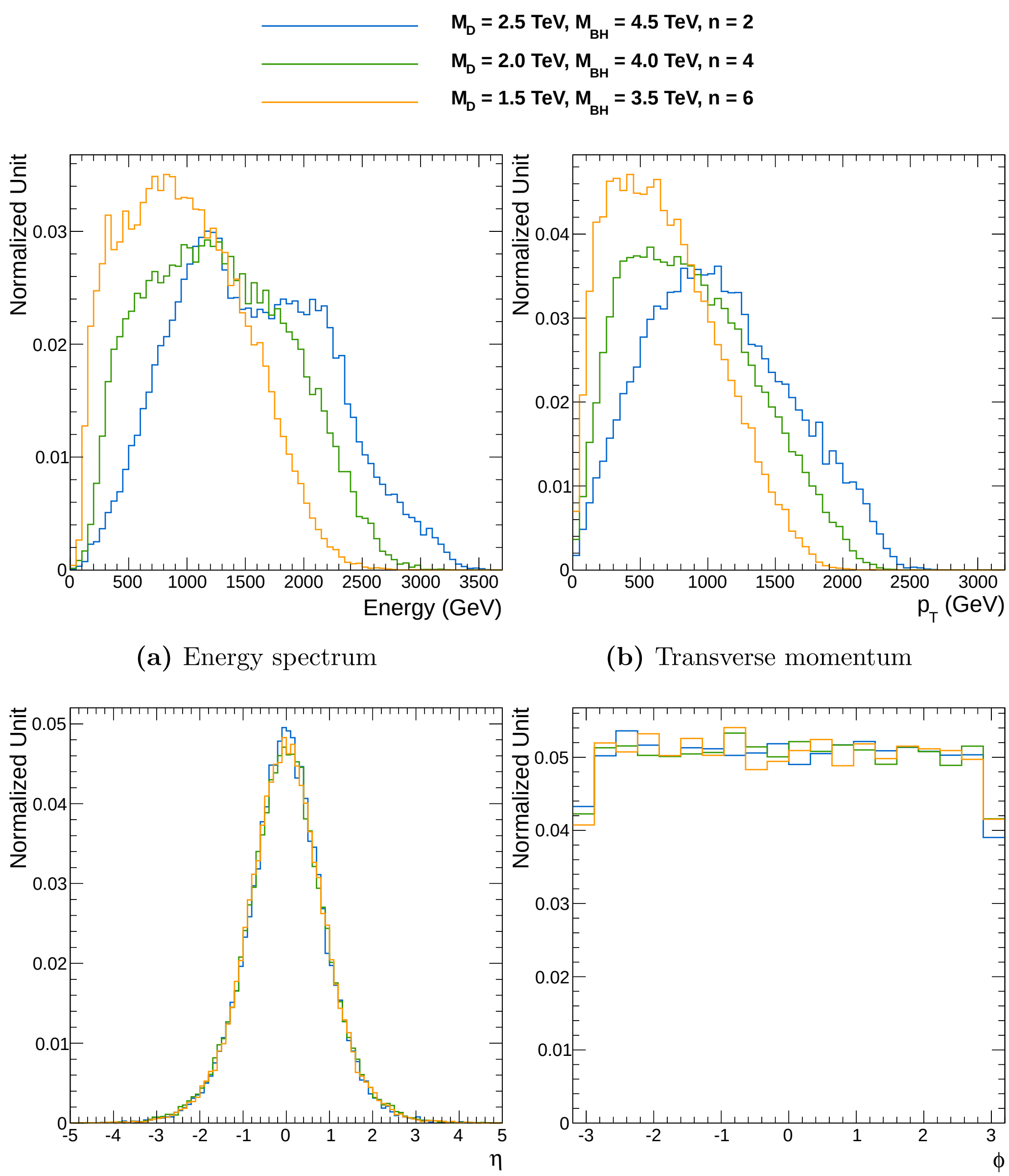

(a) Energy spectrum

(b) Transverse momentum

(c) Pseudorapidity

(d) Azimuthal angle

Figure 2.17: Properties of particles radiated from black hole events with stable remnant generated by CHARYBDIS.

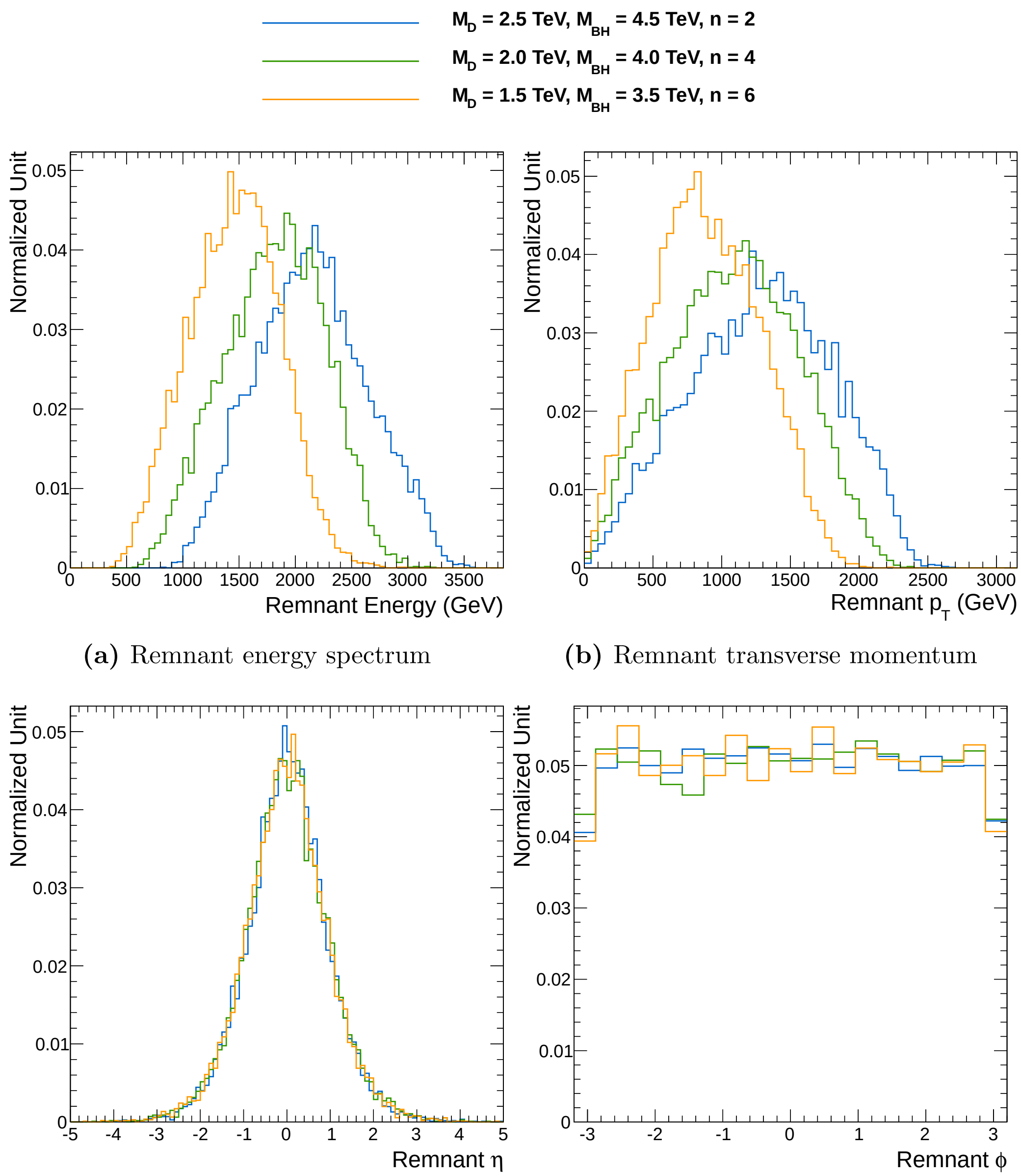

(a) Remnant energy spectrum

(b) Remnant transverse momentum

(c) Remnant pseudorapidity

(d) Remnant azimuthal angle

Figure 2.18: Properties of stable remnant from black hole events generated by CHARYBDIS.

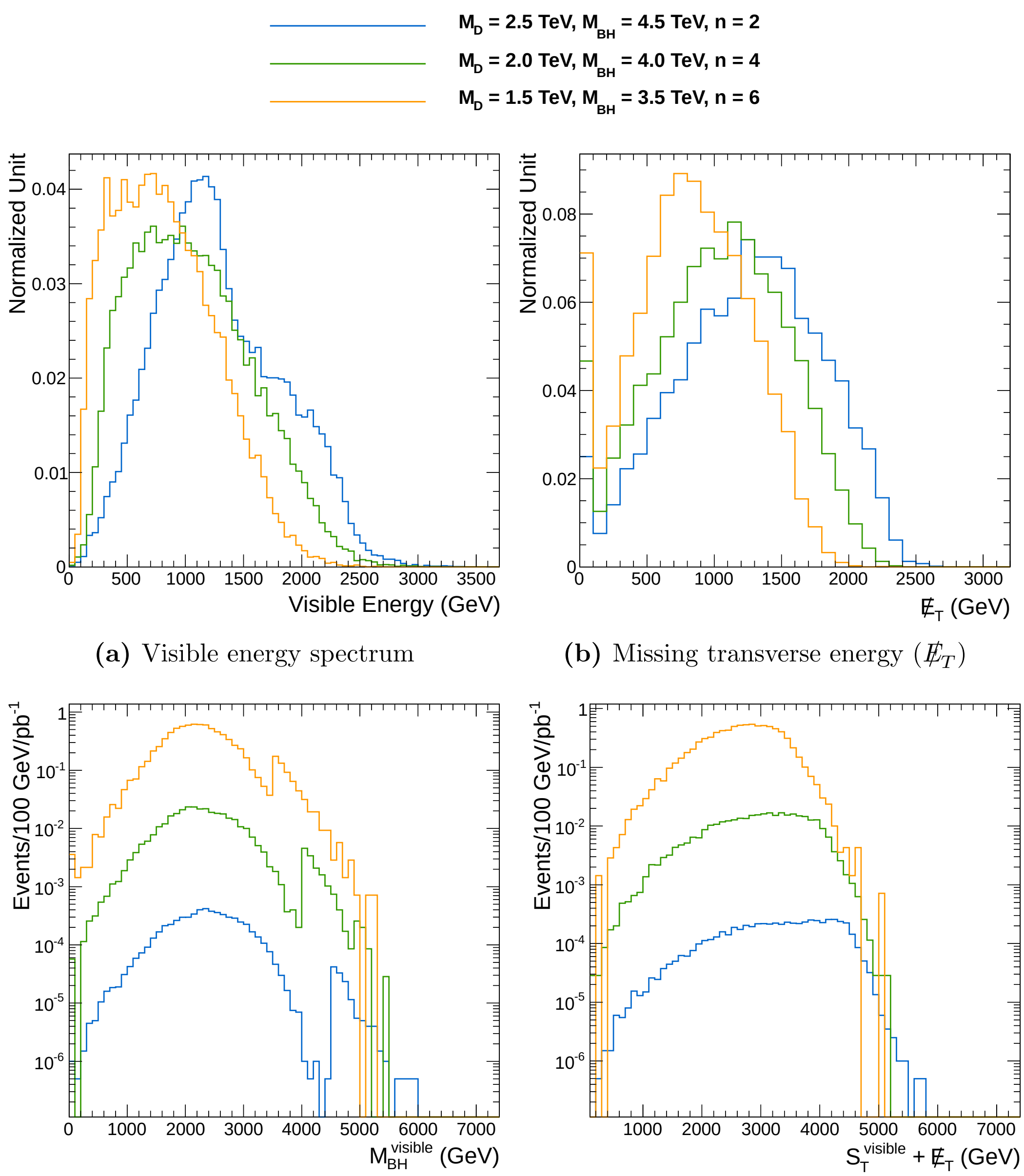

(a) Visible energy spectrum

(b) Missing transverse energy ($\not{E}_T$)

(c) Mass from visible energy and $\not{E}_T$

(d) S_{T} from visible particles plus $\not{E}_T$

Figure 2.19: Properties of visible particles from black hole with stable remnant generated by CHARYBDIS.

Chapter 3

Accelerator and Detector

3.1 Large Hadron Collider

The Large Hadron Collider (LHC) is a particle accelerator and collider facility, built by the European Organization for Nuclear Research (CERN) near northwest suburbs of Geneva on the Franco-Swiss border (Fig. 3.1). The main purpose is to accelerate two proton beams up to 7 TeV in opposite direction around an underground ring of 27 km in circumference, and collide them at several interaction points. The LHC is also capable for heavy ion collisions with lead ion ($^{208}Pb^{82+}$) beams, up to energy of 2.76 TeV/nucleon. The LHC tunnel was constructed between 1984 and 1989, originally for CERN's previous machine Large Electron-Positron Collider (LEP). As shown in Fig. 3.2, four major experiments A Toroidal LHC ApparatuS [85] (ATLAS), A Large Ion Collider Experiment [86] (ALICE), the Compact Muon Solenoid [87] (CMS), and Large Hadron Collider beauty [88] (LHCb) detectors, are located at interaction points labeled as Point 1, 2, 5, and 8, respectively. The ATLAS and

CMS experiments are two general-purpose detectors located in the experimental halls, which are new construction for the LHC project. The ALICE and LHCb, located where the original LEP infrastructure was built, are designed for heavy ion physics and B-physics, respectively.

The LHC injector complex is shown in Fig. 3.3. Protons are injected into linear accelerator (LINAC2), and accelerated to 50 MeV. Then protons go through a chain of three synchrotron accelerators: Proton Synchrotron Booster (PSB) - Proton Synchrotron (PS) - Super Proton Synchrotron (SPS), where protons are accelerated from 50 MeV to 1.5 GeV, then to 25 GeV, and finally to 450 GeV just before injecting into the LHC ring, where protons are further accelerated to nominal 7 TeV. The proton beam at SPS output contains 2808 bunches (out of 3564 available RF buckets), with 1.15×10^{11} protons per bunch. The bunch spacing is 24.95 ns, which gives basic unit of time for the LHC operation, denoted as bunch crossing (BX) time. The LHC consists of thousands of superconducting magnets, operated at a temperature under 2 K. There are 1232 dipole magnets to bend proton beam in circle, and 4800 multipole corrector magnets to focus proton beam to high intensity.

The LHC machine luminosity ($\mathcal{L}$) depends only on beam parameters, and it is given by the equation [90]:

$$\mathcal{L} = \frac{N_b^2 n_b f_{\mathrm{rev}} \gamma_r}{4\pi \epsilon_n \beta^*} F,$$

where N_b is the number of protons per bunch, n_b is the number of bunches per beam, f_{rev} is the frequency of revolution, γ_r is the relativistic gamma factor, ϵ_n is the normalized transverse beam emittance, β^* is the beta function at the collision point, and F is the geometric luminosity factor due to crossing angle at interaction point. At the nominal beam setup, the designed LHC luminosity is $10^{34}\ \mathrm{cm}^{-2}\,\mathrm{s}^{-1}$.

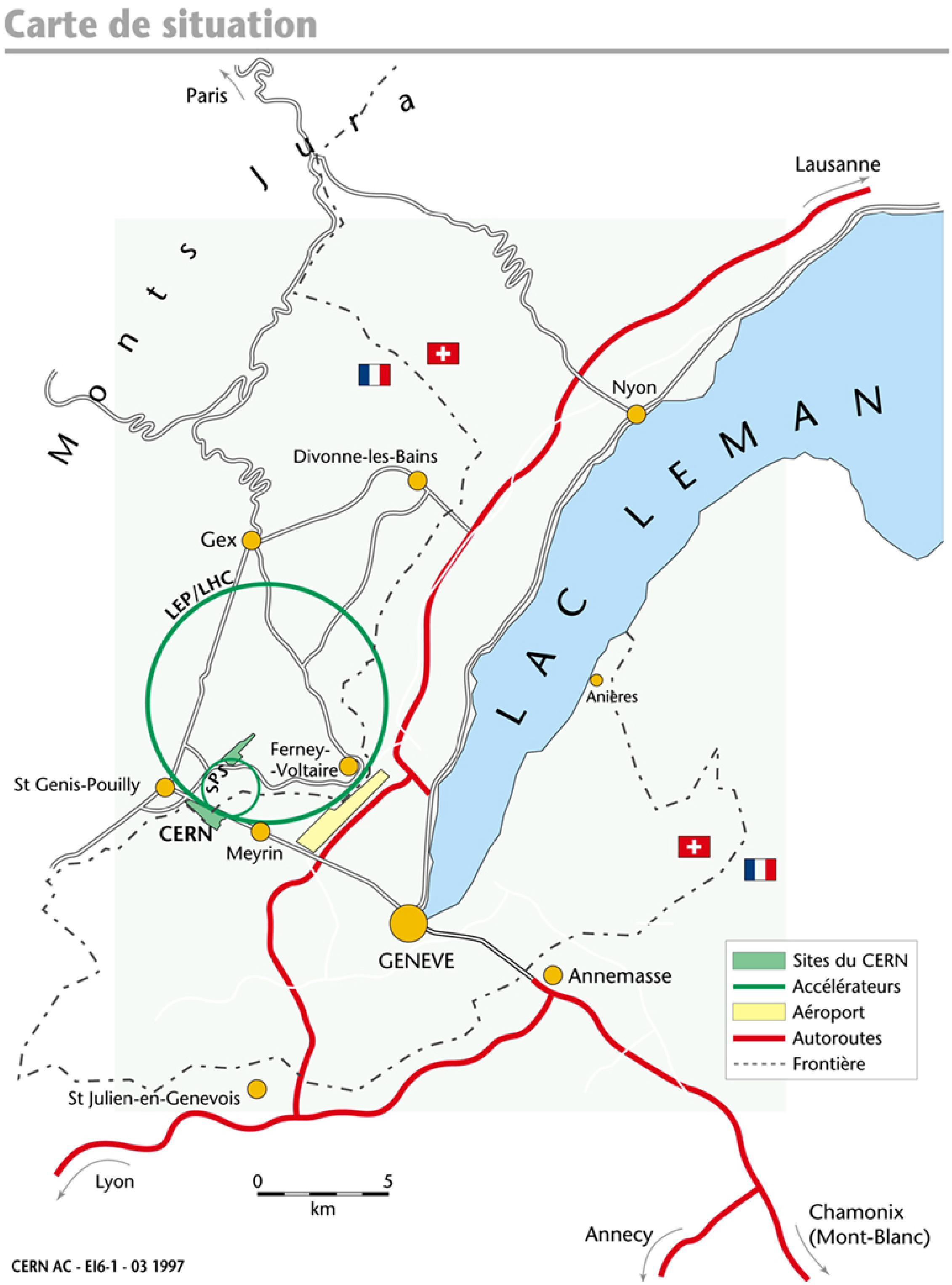

Figure 3.1: Map of Geneva region and LHC. [89]

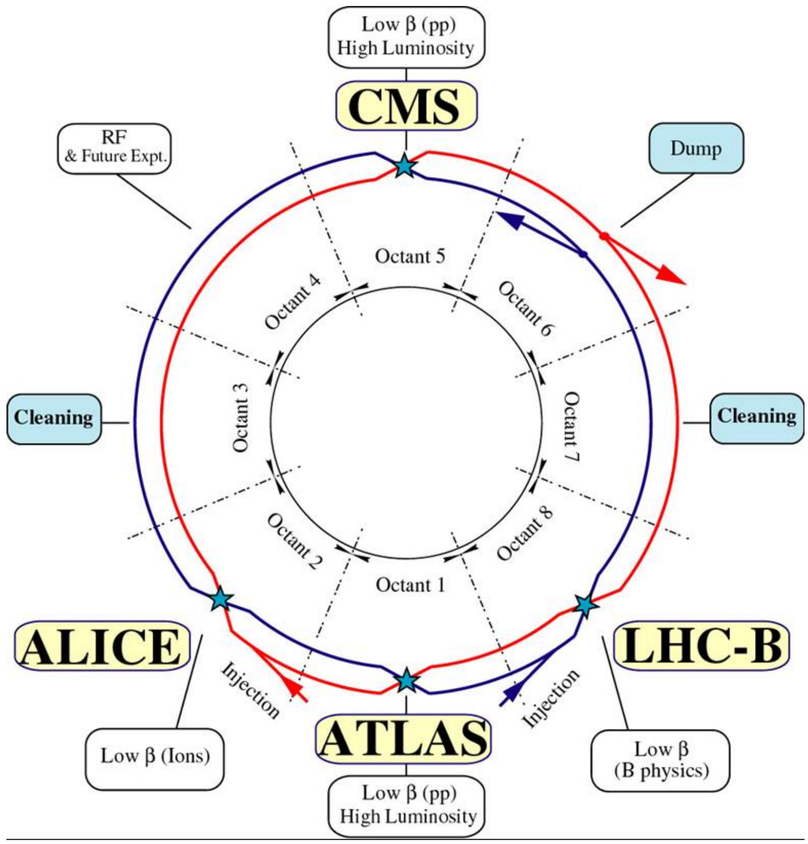

Figure 3.2: Schematic layout of LHC and locations of major experiments at different interaction points [90].

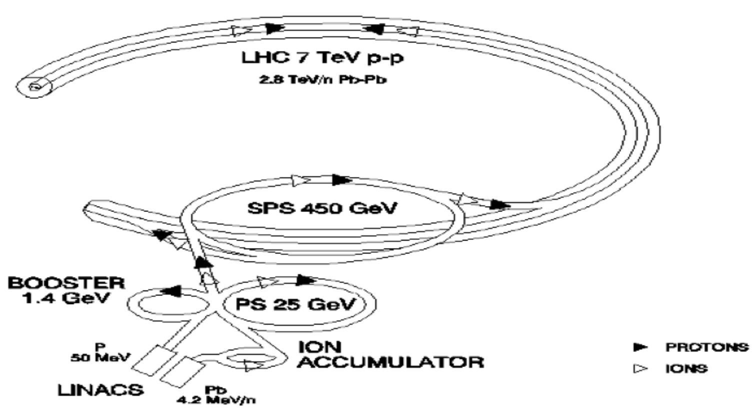

Figure 3.3: The LHC injector complex [90].

The first protons circulated at LHC ring on 10-Sep-2008, however, the collisions planned were postponed due to a failure of a connector between two superconducting magnets in sector 3 - 4, causing a leak of liquid helium. The first collision did not happened until 23-Nov-2009, when all four detector recorded collisions at 450 GeV per beam. On 30-Nov-2009, LHC achieved a new energy record of 1.18 TeV per beam, beating previous record of 0.98 TeV held by Tevatron, a proton-antiproton collider at the Fermi National Accelerator Laboratory near Batavia, Illinois, U.S. The first 7 TeV (3.5 TeV per beam) collisions occurred on 30-Mar-2010, and the machine since was kept running until the beginning of November 2010. During that period, almost $50\,\mathrm{pb}^{-1}$ of integrated luminosity of proton-proton collisions were delivered to the experiments (Fig. 3.4), and a peak luminosity of $2 \times 10^{32}\,\mathrm{cm}^{-2}\,\mathrm{s}^{-1}$ was recorded [91]. The ALICE, designed for heavy-ion collisions, was operating at low luminosity to keep the detector from being overwhelmed by the high proton collisions rate. The LHC switched to a heavy ion run from 8-Nov-2010 to 6-Dec-2010, and then shut down until Spring 2011. The LHC will operate at half of the design energy for 2 more years due to the safety concern about the connectors. After that, a year-long shutdown has been scheduled for LHC upgrade to prepare the full-energy operation in 2014.

3.2 The Compact Muon Solenoid

The Compact Muon Solenoid (CMS) is a multi-purpose detector located at Point 5 of the LHC at CERN. It is designed to study physics from 14 TeV proton-proton collisions at luminosity $10^{34}\,\mathrm{cm}^{-2}\,\mathrm{s}^{-1}$, and heavy lead ion collision (2.76 TeV per nucleon) at $10^{27}\,\mathrm{cm}^{-2}\,\mathrm{s}^{-1}$. This Section describes the main components used for the analysis in this dissertation. A detailed review of CMS experiment can be found in

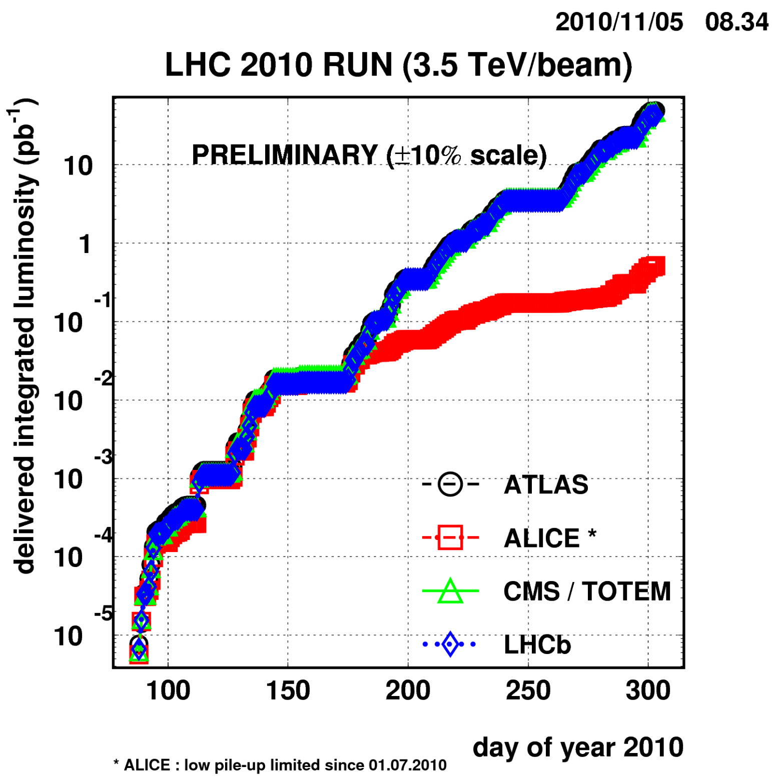

Figure 3.4: Delivered integrated luminosity for 2010 LHC 7 TeV run.

Ref. [87].

3.2.1 Overview

The CMS detector is cylindrical in shape, and placed at the center of the LHC interaction point about 100 m underground, as shown in Figs. 3.5 and 3.6. The length of CMS is 21.6 m and the radius is 7.3 m. The central feature of the CMS detector is a superconducting solenoidal magnet operated at 3.8 T in a free bore 6 m in diameter and 12.5 m in length. The magnetic field returns through a steel yoke comprising 5 wheels and 2 endcaps, each made of 3 disks. The main detector components of CMS are the inner tracking system or tracker, two calorimeters (electromagnetic and hadronic), and the muon system, which is embedded in the return yoke. All other

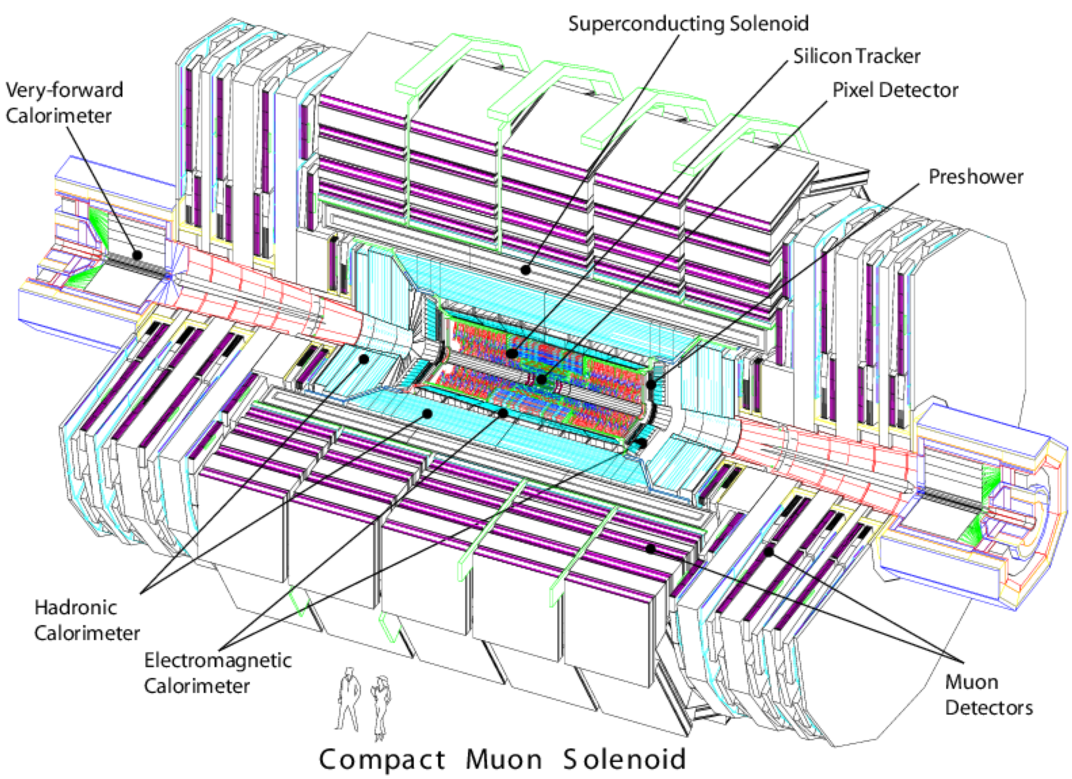

Figure 3.5: Layout of CMS and its component.

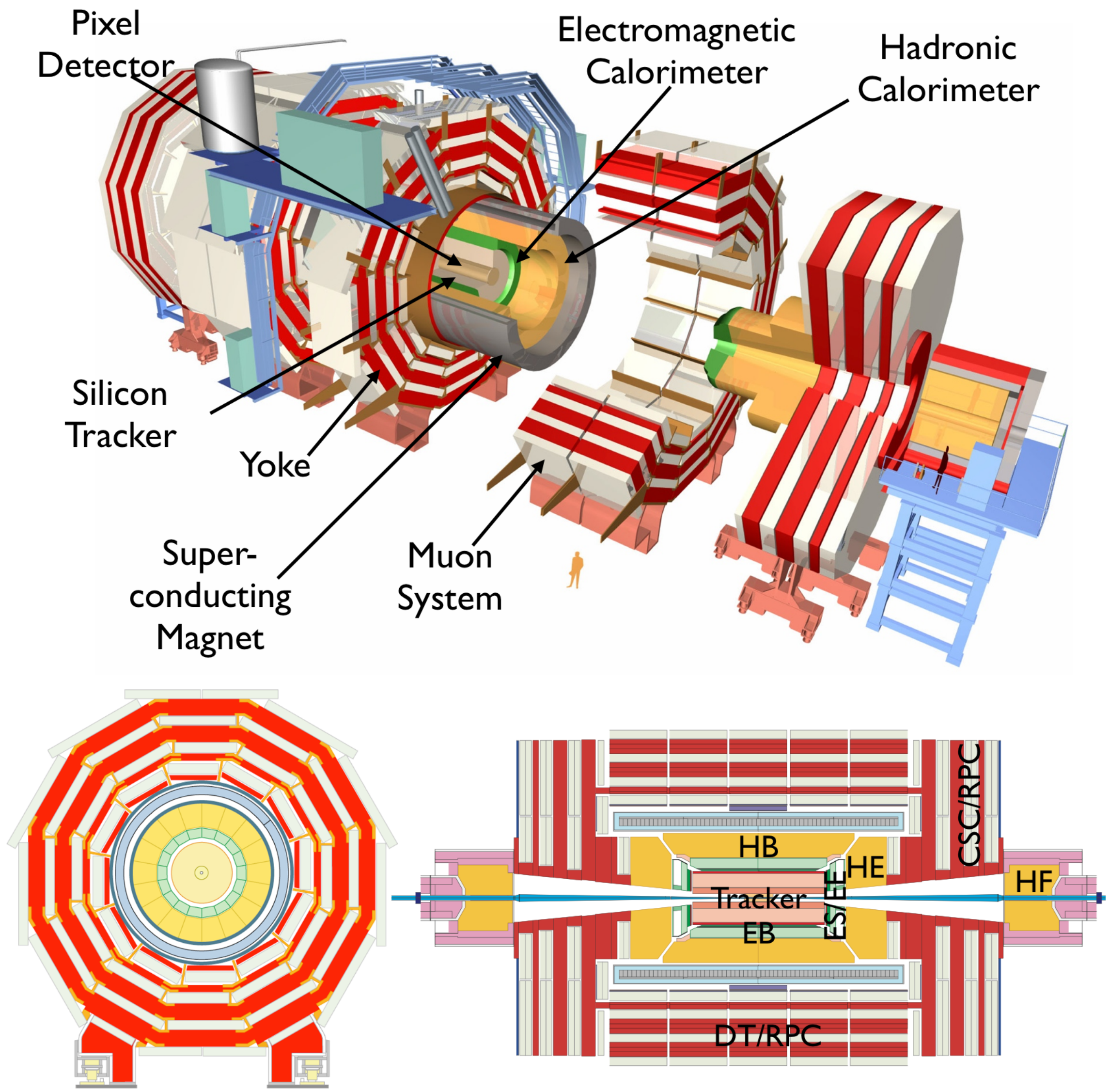

Figure 3.6: The color render layout of CMS in different views.

detector components, except forward calorimeter, are enclosed by the magnet.

The coordinate system of CMS has the origin at the nominal collision point. The z-direction points along the counterclockwise proton beam direction, toward the Jura mountain. The x-axis points toward the center of LHC ring, while the y-axis points vertically upward. The longitudinal direction is the same as z-direction, while the transverse direction refers to the projection on $x-y$ plane. In polar coordinates, the azimuthal angle ϕ is measured from the x-axis in the $x-y$ plane; the polar angle θ is measured from the z-axis; the radial distance is measured from the origin. The rapidity y is often used instead of the polar angle θ:

$$y = \frac{1}{2} \ln \left(\frac{E + p_z}{E - p_z} \right),$$

where E is the particle energy and p_z is the momentum in z-direction. Rapidity is used instead of polar angle (θ) because the difference in rapidity is Lorentz invariant against the boost along the beam axis, while difference in θ is not. For ultra-relativistic particles $E \gg m$, the rapidity y can be approximated by the pseudorapidity η,

$$\eta = -\ln \left(\tan \frac{\theta}{2} \right).$$

3.2.2 Inner Tracking System

The CMS inner tracking system, known as tracker, located inside a superconducting coil with nominal 3.8 T solenoidal magnetic field, is designed to measure trajectories of charged particles produced in the LHC proton-proton collisions, and to reconstruct secondary vertices (Fig. 3.7). The CMS tracker is composed of two sub-detectors: pixel detector and silicon strip tracker. Figure 3.8 shows CMS tracker resolutions in different regions.

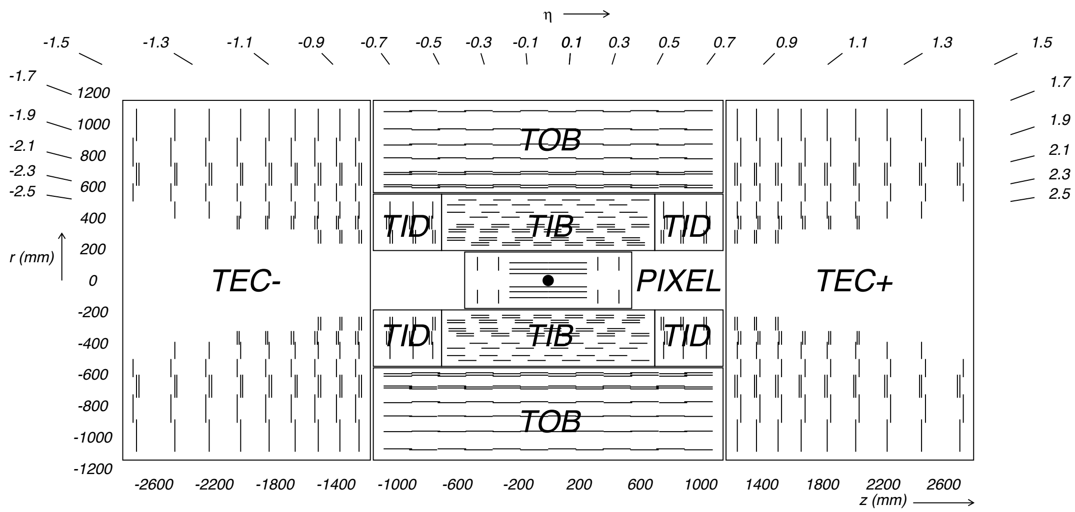

Figure 3.7: Layout of CMS tracker and its components. Single lines represent a single detector module, while double lines correspond to back-to-back modules. [92].

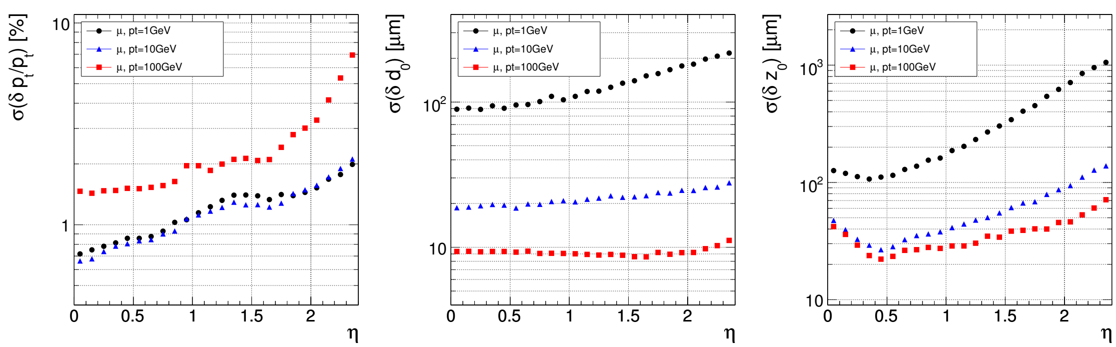

Figure 3.8: Resolution of transverse momentum (left), transverse impact parameter (middle), and longitudinal impact parameter (right) of for a single muon at different transverse energies [92].

The pixel detector (Fig. 3.9) consists of three barrel layers and four endcap disks, two on each side of barrel, covering the pseudorapidity range $|\eta| < 2.5$. It is the closest detector to the interaction point. The pixel detector measures tracking points precisely. Its small impact parameter resolution gives good secondary vertex reconstruction. Three barrel layers enclose the interaction point cylindrically at mean radii 4.4 cm, 7.3 cm, and 10.2 cm respectively and a length of 53 cm. The endcap disks are located on each side at 34.5 cm and 46.5 cm away from interaction point, which extending from about 6 to 15 cm in radius. The pixel detector contains 66 million pixel cells (48 million for barrel layers, 18 million for endcap disks), each pixel size of $100 \times 150\ \ \mu\mathrm{m}^2$, covering a total area of $1.06\ \ \mathrm{m}^2$ ($0.78\ \ \mathrm{m}^2$ for barrel, $0.28\ \ \mathrm{m}^2$ for endcap).

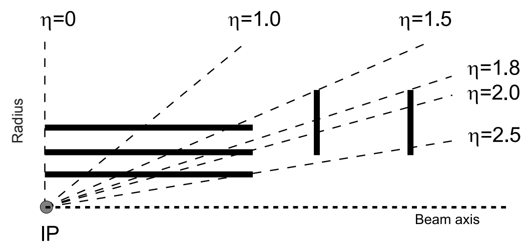

Figure 3.9: Layout of CMS pixel detector and its geometric coverage on barrel and endcap. [92].

The silicon strip tracker is composed of Tracker Inner Barrel (TIB), Tracker Outer Barrel (TOB), Tracker Inner Disk (TID) and Tracker Endcaps (TEC), occupying radial region between 20 cm and 116 cm. The TIB consists of four concentric cylinders at radii of 255.0 mm, 399.0 mm, 418.5 mm and 498.0 mm, with total length of 1400 mm. The two innermost layers of TIB are built with double-sided modules, while the outer two equipped with single-sided modules. Tracker Inner Disk detector is built three disks located at each end of TIB between 800 mm and 900 mm in the z-direction. Each disk is made of three rings, which span radius from 200 mm to 500 mm. The two innermost rings host double-sided modules, while the outermost one only host single-sided modules. The pseudorapidity coverage of TIB/TID is up to $\eta = 2.5$. The TIB/TID is enclosed by TOB, which consists of layers of concentric cylinders at radii of 608, 692, 780, 868, 965, and 1080 mm. Except the two innermost layers, where two-sided modules are hosted, all four outer layers are mounted with single-sided modules. Two endcaps, placed at ± 1240 mm to ± 2800 mm along z-direction, close the both end of barrel system (TIB/TID/TOB). Each TEC consists of 9 disks, with radii from 220 mm to 1135 mm, where each disk is divided into several rings. As shown in Fig. 3.7, not every ring is populated with the silicon strip modules. The endcaps extend pseudorapidity range of whole tracker up to $|\eta| \approx 2.5$.

3.2.3 Electromagnetic Calorimeter

The CMS electromagnetic calorimeter (ECAL), as shown in Fig. 3.10, is a hermetic homogeneous calorimeter, comprised of three parts: ECAL barrel (EB), ECAL end-cap (EE), and the preshower detector (ES). The ECAL provides measurement of energy of particles via electromagnetic interactions with lead-tungstate ($PbWO_4$) crystals. It provides information for electron and photon identification, and contributes to jet and missing transverse energy measurements. Lead-tungstate has high density (8.28 $\mathrm{g\,cm^{-3}}$), short radiation length (0.89 cm), and a small Molière radius (2.2 cm), which is an ideal material for a fine granularity and a compact calorimeter.

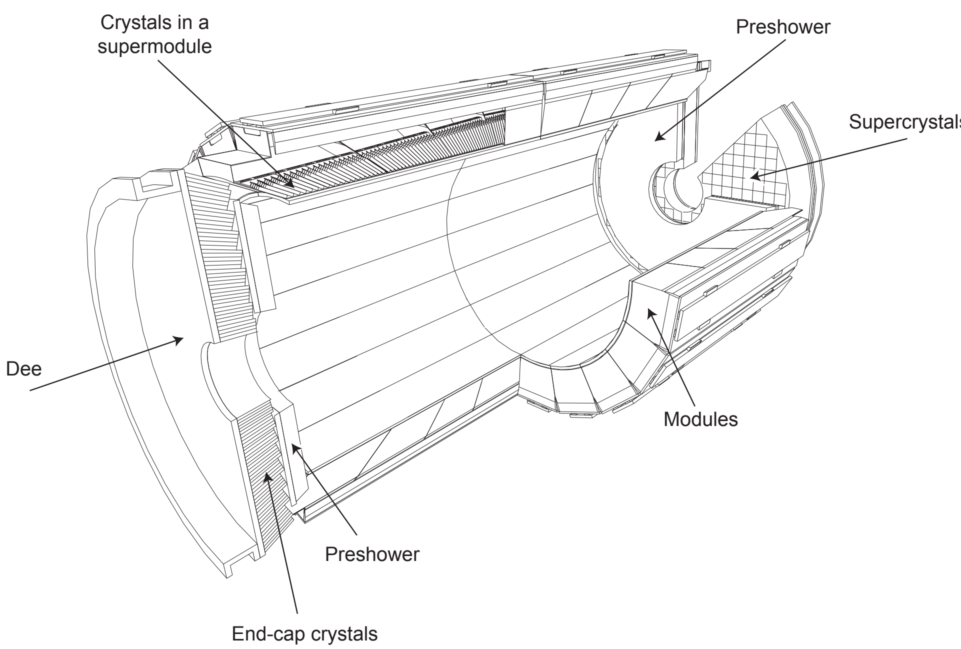

Figure 3.10: Layout of electromagnetic calorimeter [93].

The barrel, central part of ECAL, covering pseudorapidity range $|\eta| < 1.479$, is made up of 61200 lead-tungstate crystals. The radius of EB is 1.29 m and it is 6 m long in the z-direction. The granularity of EB is 360-fold in ϕ and (2x85)-fold in η, where the crystal cross section gives approximately 0.0174×0.0174 in $\eta - \phi$ or

$22 \times 22\ \text{mm}^2$ at the front face, and $26 \times 26\ \text{mm}^2$ at the rear face. The total crystal length is $230\ \text{mm}$, which is equivalence to 25.8 radiation lengths.

The endcaps, located on each side of EB, extend pseudorapidity range to $1.479 < |\eta| < 3.0$. The crystals in the endcap, which have identical shape, with rear face cross section of $30 \times 30\ \text{mm}^2$ and front face cross section of $28.62 \times 28.62\ \text{mm}^2$, are grouped to a supercrystals (SCs) in mechanical units of 5×5 crystals. Each endcap is divided into 2 halves (called Dees), where each Dee contains 3662 crystals, arranged in 138 standard SCs and 18 special partial SC on the inner and outer circumference. The EE has a total length of $220\ \text{mm}$, or 24.7 radiation length.

The preshower detector (ES), covering a fiducial region $1.653 < |\eta| < 2.6$, aims to identify neutral pions in the endcaps. The ES is a sampling calorimeter, containing two alternating layers of lead and silicon-strip sensors. Incoming photons or electrons initiate electromagnetic showers, and deposit energy in silicon strip sensors after each radiator. The total thickness of ES is $20\ \text{cm}$, giving 2 radiation length before reaching the first sensor plane, and further 1 radiation length before reaching the second sensor plane.

The ECAL energy resolution (σ/E) for a given energy E, can be parameterized in the following form:

$$\left(\frac{\sigma}{E}\right)^2 = \left(\frac{S}{\sqrt{E}}\right)^2 + \left(\frac{N}{E}\right)^2 + C^2,$$

where S, N, and C represent stochastic, noise, and constant terms respectively. The stochastic term is characterized by event-to-event fluctuations in the lateral shower containment, photostatistic contribution, and energy fluctuations in the preshower absorber with respect to the preshower silicon detector. The source of the noise term, which is negligible at high energies, originates from electronics, digitization, and pileup noises. The last, constant term takes into account non-uniformity of longitudinal light collection, intercalibration errors, and leakage of energy from the back of the crystals. The energy resolution is determined in the test beams by measuring the energy of electrons from 20 to 250 GeV, with an array of 3×3 crystals centered on a reference crystal:

$$\left(\frac{\sigma}{E}\right)^2 = \left(\frac{2.8\%\,\mathrm{GeV}^{\frac{1}{2}}}{\sqrt{E}}\right)^2 + \left(\frac{0.12\,\mathrm{GeV}}{E}\right)^2 + (0.30\%)^2\,.$$

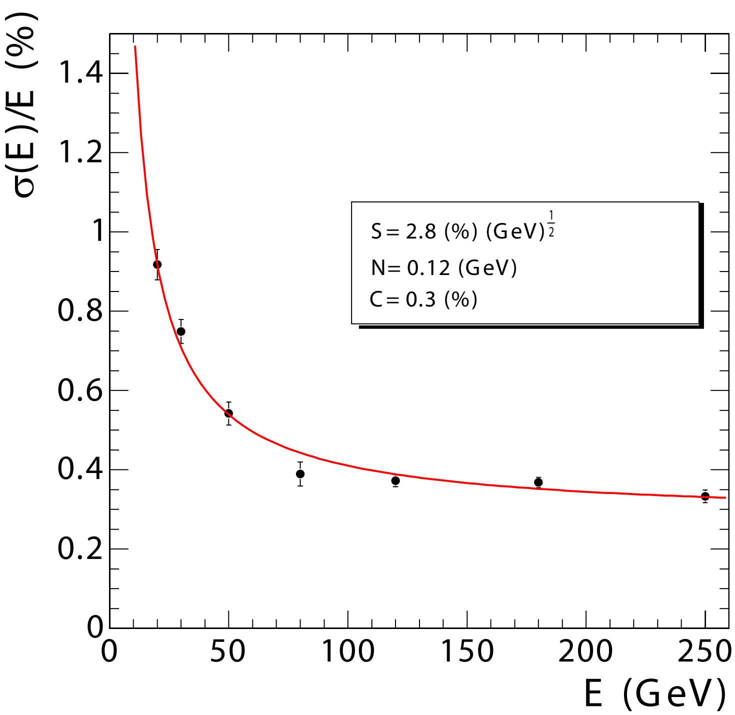

Figure 3.11: Energy resolution of ECAL as a function of electron energy E. The data points are parameterized by stochastic (S), noise (N), and constant (C) terms [87].

3.2.4 Hadron Calorimeter

The hadron calorimeter (HCAL) of CMS is located between the outer extent of ECAL, and the inner extent of the magnet coil, radially between 1.77 m and 2.95 m

(Fig. 3.12). The hadron calorimeter is a sampling calorimeter made of alternating layers of brass absorbers and scintillators.

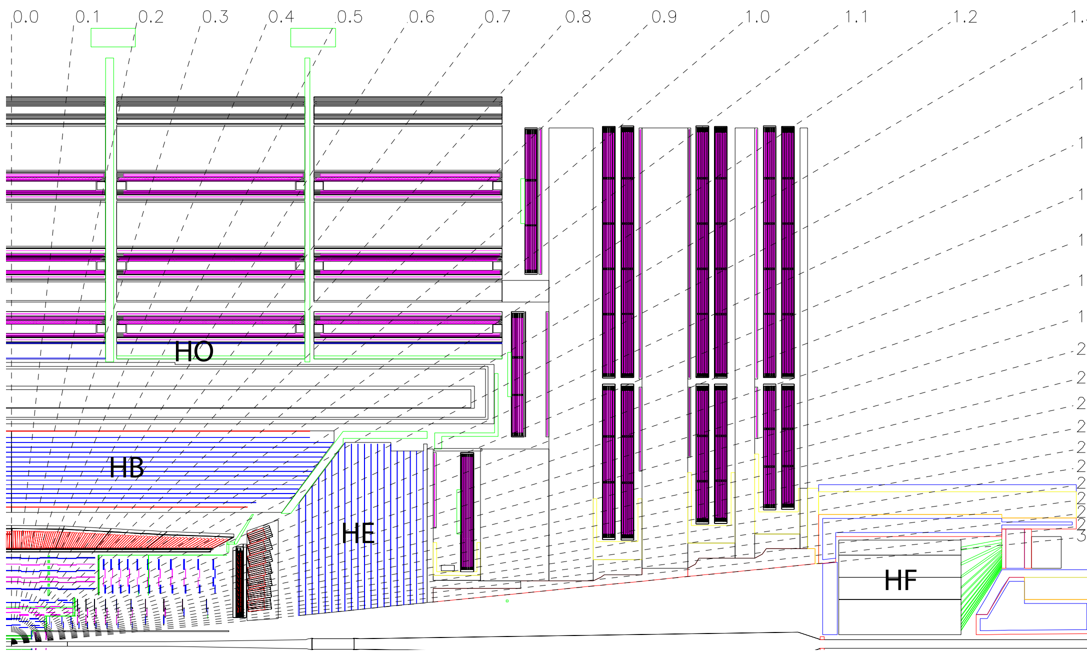

Figure 3.12: Layout of hadronic calorimeter [87].

The hadron calorimeter barrel (HB) covers pseudorapidity range $|\eta| < 1.3$, and is divided into two half sections (HB+,HB-). There are 36 identical azimuthal wedges from two half-barrels, where flat brass absorber plates are aligned parallel to the beam axis. The plastic scintillator is divided into 16 sectors in the η-coordinate, which results in a granularity of 0.087×0.087 in $\eta - \phi$. The thickness of the absorber corresponds to 5.82 interaction lengths for a particle that is coming normal to the absorber plates, and has an 10.6 interaction lengths at larger $|\eta|$, as the effective thickness increases with the polar angle. Additional 1.1 interaction lengths is added from ECAL crystals.

Since the stopping power of the HCAL and ECAL in the central region does not provide sufficient containment for hadron showers, an additional outer calorimeter (HO) is extended outside the solenoid. The HO roughly maps the layers of HB in same geometry, with a tower granularity of 0.087×0.087 in $\eta - \phi$. The total thickness of the whole calorimeter is increased to a minimum of 11.8 interaction lengths in the barrel region.

The hadron calorimeter endcap (HE) is a similar device to HB, which covers pseudorapidity range of $1.3 < |\eta| < 3$, and is inserted into the ends of the solenoidal magnet. Each HCAL endcap is divided into 14 sectors in η, numbering from 16 to 29, and 36 azimuthal segments. The ECAL endcap and preshower detector are attached at the front face of HE. The HE η-tower 16 overlaps with the last tower of HB. The granularity of HE is $\Delta\eta \times \Delta\phi = 0.087 \times 0.087$ for $|\eta| < 1.6$ and $\Delta\eta \times \Delta\phi \approx 0.17 \times 0.17$ for $|\eta| \geq 1.6$. Together with the ECAL material, the HE thickness is about 10 interaction lengths.

The forward hadron calorimeter (HF), is located outside steel magnetic return yokes, 11.2 m from the interaction point, and extends over the pseudorapidity range of $3 \leq |\eta| \leq 5.2$. The HF consists of a steel absorber of depth 165 cm (about 10 interaction length). There are two set of alternating quartz fibers, provide readouts at a depth of 22 cm from the front of the detector known as short fibers (S), and at full depth of the absorber for long fibers (L). Since there is no ECAL covering in forward region, the readout from the long and short fibers gives an estimation for electromagnetic and hadronic shower energy fractions. Each side of HF is divided into 13 rings in η and 36 azimuthal wedges. Every segment is bundled with a pair of long and short fibers into a tower 0.175×0.175 in $\eta - \phi$.

The energy resolution σ/E of HCAL can be modeled with a stochastic term S and a constant term C,

$$\left(\frac{\sigma}{E}\right)^2 = \left(\frac{S}{\sqrt{E}}\right)^2 + C^2. \tag{3.1}$$

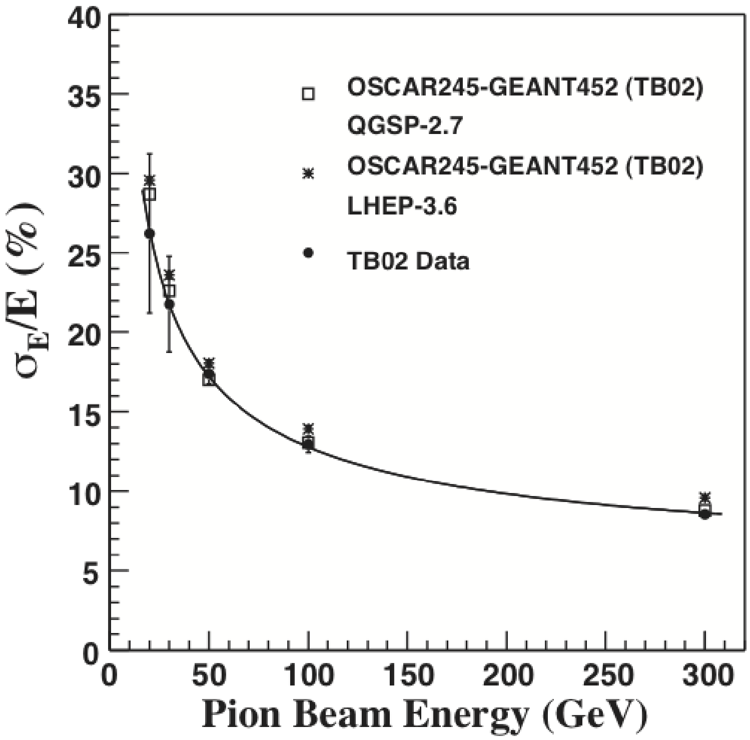

Figure 3.13: Energy resolution of HB as a function of pion energy E [94].

Extensive measurements have been made by using test beams at 20 - 300 GeV pions. Energy deposited in a 5x5 HB tower array centered on pion beam position are summed. Energy deposited in the corresponding ECAL region is less than 2 GeV. Figure 3.13 shows the energy resolution for HB [92, 94]:

$$(\frac{\sigma}{E})^2 = (\frac{115.3\%}{\sqrt{E}})^2 + 5.5\%^2. \tag{3.2}$$

Similar measurements have been done on HF with pion and electron test beams [95]. Energy deposited in long and short fibers are measured with various beam energy, which gives $S = 198\%$, $C = 9\%$ for electromagnetic energy resolution, and $S = 280\%$, $C = 11\%$ for hadronic energy resolution.

3.2.5 Muon System

The drift tube (DT) chambers of the CMS are in the barrel region of muon system, covering the pseudorapidity range of $|\eta| < 1.2$. The DT chambers are arranged in four stations, labeled as MB1, MB2, MB3 and MB4, forming a set of concentric cylinders around the beam line. Each station is divided into 5 wheels, following the yoke segmentation, where one wheel consists of 12 azimuthal sectors. There are 60 drift chambers in the 3 inner stations, and 70 chambers in the outer. A drift cell is a rectangular box, $13 \times 42\ \mathrm{mm}^2$ at transverse face, filled with Ar/CO_2 (85%/15%) gas mixture. Four adjacent drift cells form a superlayer (SL), where 3 superlayers are put inside a DT chamber at 3 inner stations. Wires in the middle layer are orthogonal to the beam line to measure in the z-direction, while wires in the outer layers are parallel to the beam line to measure the track momentum at the ϕ-direction. For the outermost station, there are only 2 superlayers on each chamber without z-direction measurement.

The endcap of muon system is made of cathode strip chambers (CSC). Each endcap consists of 4 disk-like stations (ME1 to ME4), mounted on the iron disks enclosing the CMS magnet, where the disks are perpendicular to the beam direction. Each disk is divided into 2 concentric rings (labeled as ME2/1, ME2/2,...,ME4/2), except ME1 which has 3 rings (ME1/1, ME1/2, ME1/3). The innermost ring has 36 chambers of 10° azimuthal sectors, while there are 18 chambers on each outer rings. A CSC chamber is a multiwire proportional device made of 6 anode wire planes interleaved among 7 cathode panels in trapezoidal shape. A gas mixture of $Ar/CO_2/CF_4$ (40%/50%/10%) is filled between 6 gas gaps. Each of the chambers, except those in ME1/3, overlaps its adjacent neighbors to provide a full coverage in ϕ. At least 3 chambers are expected to detect signals coming from a muon path in

$1.2 < |\eta| < 2.4$. The endcap CSC system has an overlap region $0.9 < |\eta| < 1.2$ with barrel DT system.

Resistive plate chambers (RPC) are gaseous parallel-plate detectors, covering both muon barrel and endcap regions. A RPC module consists of 2 gas gaps, filled with 3 components: $C_2H_2F_2/iC_4H_10/SF_6$ (96.2%/3.5%/0.3%). As the tagging time of RPC for an ionizing event is about 1-4 ns, much shorter than one LHC bunch crossing (25 ns), the RPC is capable to act as a muon trigger system during collision. In the barrel region, resistive plate chambers are located internally and externally to each DT chamber in the first and second stations, labeled as RB1 and RB2. At the third and fourth stations, 2 RPC modules are placed on the inner side of each DT chamber, namely RB3+, RB3-, RB4+, RB4-. One exception is sector 4 of the fourth station, four RPC are attached to the inner DT chambers. Like the barrel, three RPC stations (RE1, RE2 and RE3) are mounted on CSC chambers. However, only the innermost rings are staged at the beginning of LHC collisions, which cover pseudorapidity up to 1.6.

3.2.6 Trigger

For the nominal LHC luminosity of 10^{34} $\mathrm{cm^{-2}\,s^{-1}}$, approximately 20 proton-proton at 14 TeV collisions occur for every beam crossing interval of 25 ns, corresponding to a frequency of 40 MHz. Given an event size of 1.5 MB, it is impossible to store every single event on disk. The purpose of a trigger system is to decide whether accept or reject an event every 25 ns, benchmarked by the expected particle production at the design LHC luminosity (Fig. 3.14). The trigger system of the CMS has two levels: Level-1 (L1) Trigger and High-Level Trigger (HLT). The Level-1 Trigger is made of custom-design programmable electronics to reject at least a factor of 10^3 of the incoming events. The maximum output rate for L1 Trigger is 100 kHz. Events accepted by L1 Trigger (L1 Accept or L1A) are passed to HLT, where decisions are made by event reconstruction software run on computer farm. Events accepted by HLT, at a maximum rate of 300 Hz, are stored on disk for further analysis.

Level-1 Trigger is designed to gather readouts from all subdetectors and make L1A decisions for every 25 ns continuously. Field Programmable Gate Arrays (FPGA) are used in most of the trigger hardware, together with Application Specific Integrated Circuits (ASICs), and programmable Lookup Tables (LUTs), to provide a flexible development platform and fast-response electronic systems. The buffer size of L1 system is 128 BX, allowing a maximum latency of 32 μs for communication and some room for slower detectors, such as DT. As shown in Figure 3.15, L1 Trigger consists of two parts: calorimeter and muon triggers.

Calorimeter Trigger

The decision of the calorimeter trigger is based on the energy deposited in the ECAL and the HCAL. In the barrel region $|\eta| < 1.479$, each side is divided into 17×72 trigger towers in $\eta - \phi$, so that each trigger tower covers uniformly on $\Delta\eta \times \Delta\phi = 0.087 \times 0.087$. One trigger tower corresponds to a HB tower and 5×5 EB crystals. In the endcap region $1.479 < |\eta| < 3.000$, there are 11×72 trigger towers on each side. The granularity is the same as barrel trigger towers up to $|\eta| \approx 2$, and the size of trigger tower increases at higher η, as shown in Figure 3.16. For $|\eta| > 1.74$, HE tower size is twice the dimension in ϕ of a trigger tower. Hence an HE tower in this region is split into two trigger towers in ϕ, each one shares half of the HE tower energy. In the forward region where ECAL is absent, 12 HF towers grouped in $3\eta \times 2\phi \times 2$ fibers (long/short) are combined into one trigger tower (Fig. 3.17).

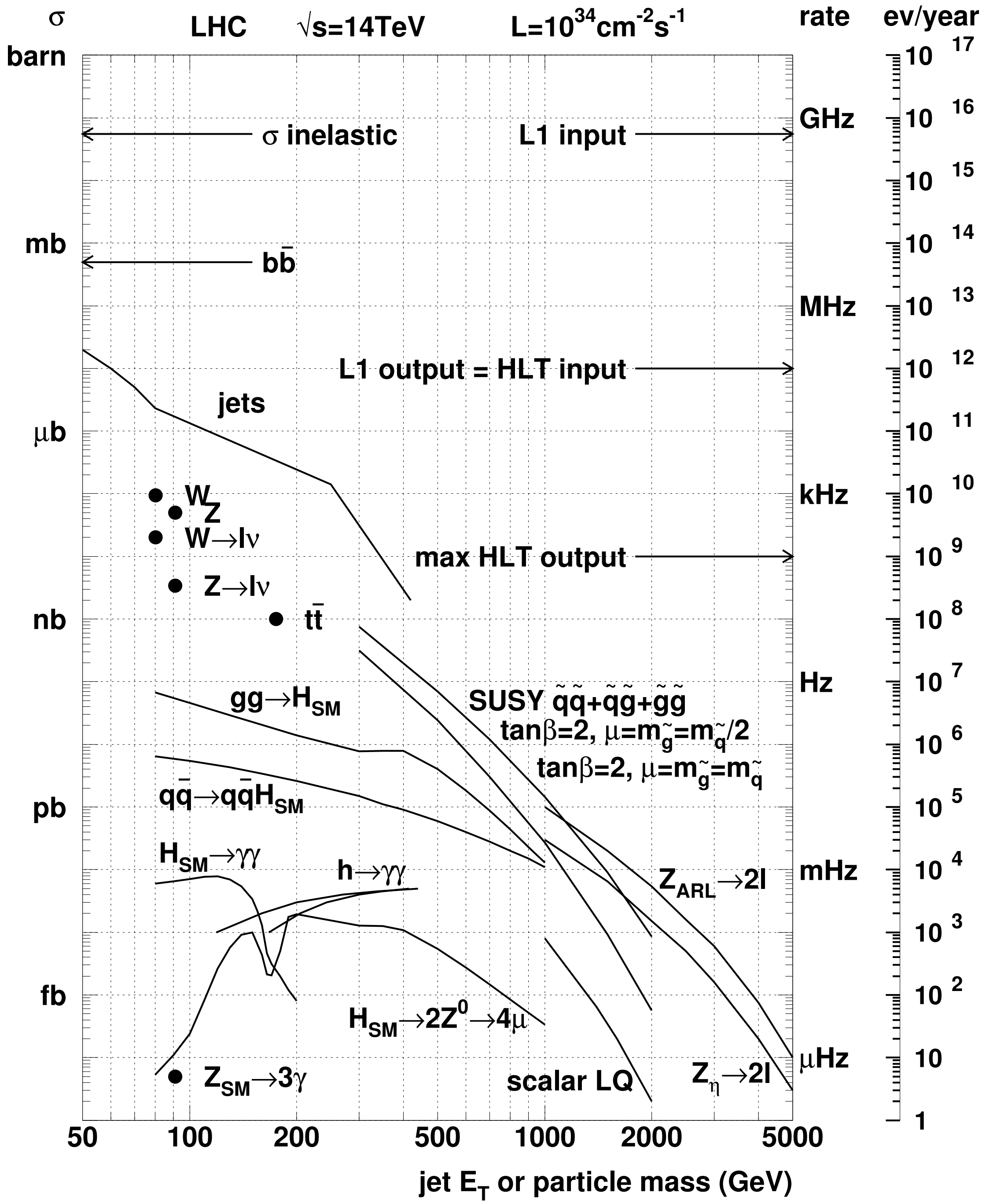

Figure 3.14: Cross sections and rates of particle production of LHC 14 TeV proton-proton collision at designed luminosity 10^{34} $\mathrm{cm}^{-2}\,\mathrm{s}^{-1}$ [93].

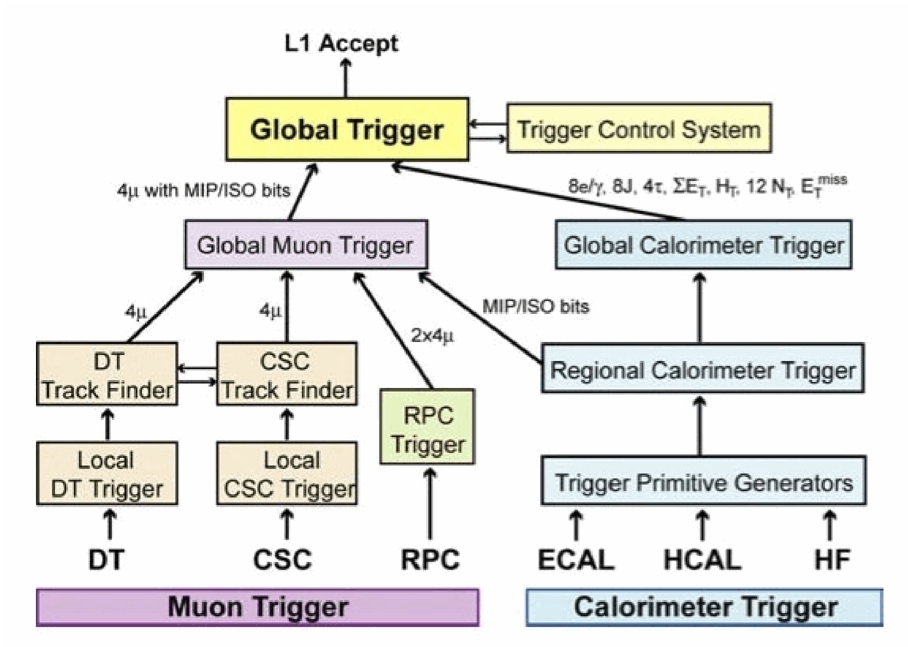

Figure 3.15: Overview of CMS Level-1 Trigger system [87].

As a result, there are $4\eta \times 18\phi$ trigger towers on each HF side, where a trigger tower has dimensions $\Delta\eta \times \Delta\phi = 0.500 \times 0.348$.

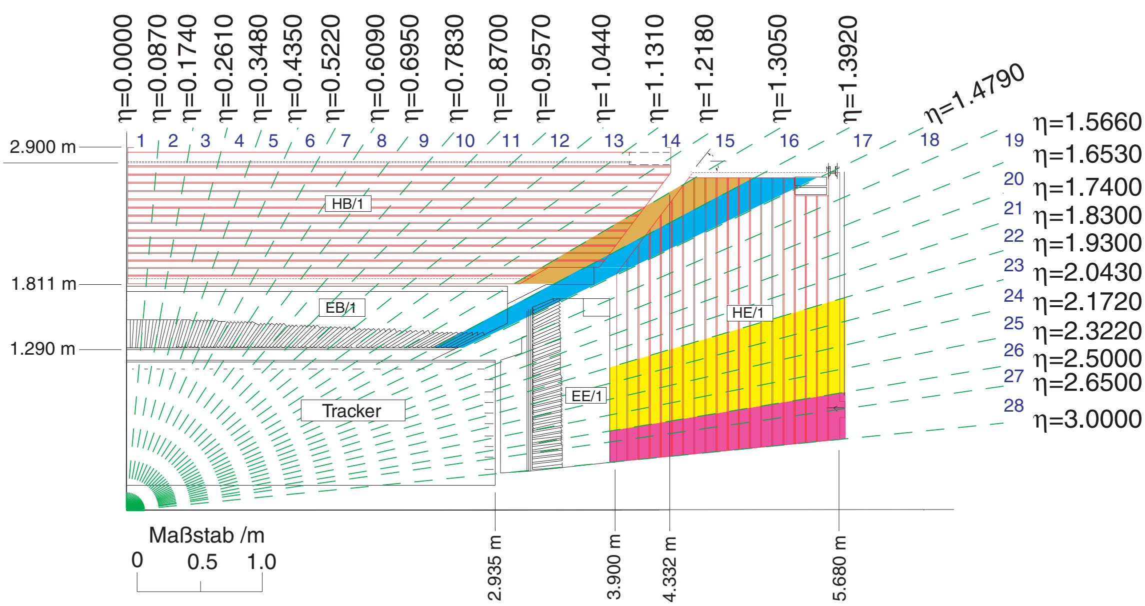

Figure 3.16: Layout of calorimeter trigger towers [93].

Trigger Primitives (TPs) generated by local calorimeter trigger tower readout, are then sent to Regional Calorimeter Trigger (RCT). Every 4×4 HCAL/ECAL trigger

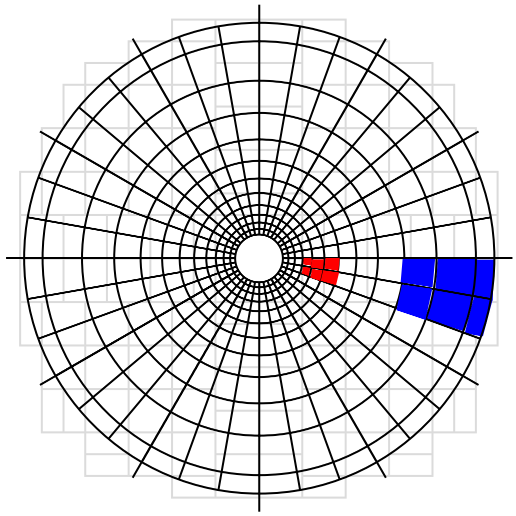

Figure 3.17: Layout of calorimeter trigger towers in HF [93].

towers are combined into a RCT region, except in HF where one trigger tower is a RCT region. The RCT outputs are sent to Global Calorimeter Trigger (GCT), where jet and electron/photon algorithms are performed. The jet finding algorithm (Fig. 3.18) is based on a sliding sum of the ECAL and the HCAL energy in a 3×3 RCT region. A τ-jet is defined as none of the 9 RCT region contains more than two active ECAL/ECAL trigger towers in a 4×4 region. The electron/photon algorithm (Fig. 3.19) starts looking for the ECAL trigger tower with highest energy deposit for every RCT region. Then the highest energy in the four board side neighbors is added. A non-isolated electron/photon candidate has to pass two vetos: energy must be deposited in a 2×5 crystals array in that ECAL trigger tower, indicated by the fine-grain bit of the ECAL TPG, and the HCAL-to-ECAL energy ratio must be less than a predefined threshold (typically 5%). An isolated electron/photon candidate requires passing vetos for all eight neighboring towers, and at least one quiet corner around the hit tower. The 4 highest transverse energy trigger candidates (central jets, forward jets, τ-jets, isolated/non-isolated), the missing transverse energy, and the total energy sum are sent to Global Trigger (GT), where L1A decision is made.

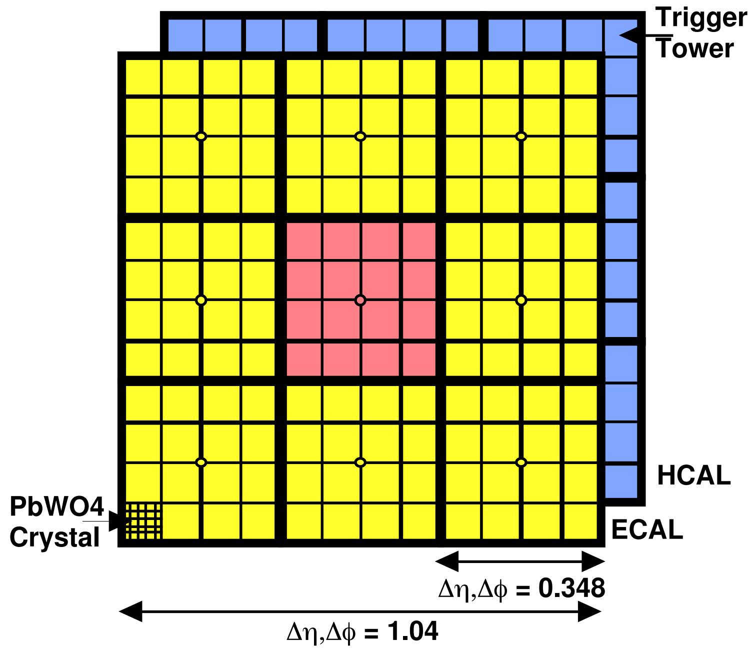

Figure 3.18: Level-1 jet trigger algorithm [93].

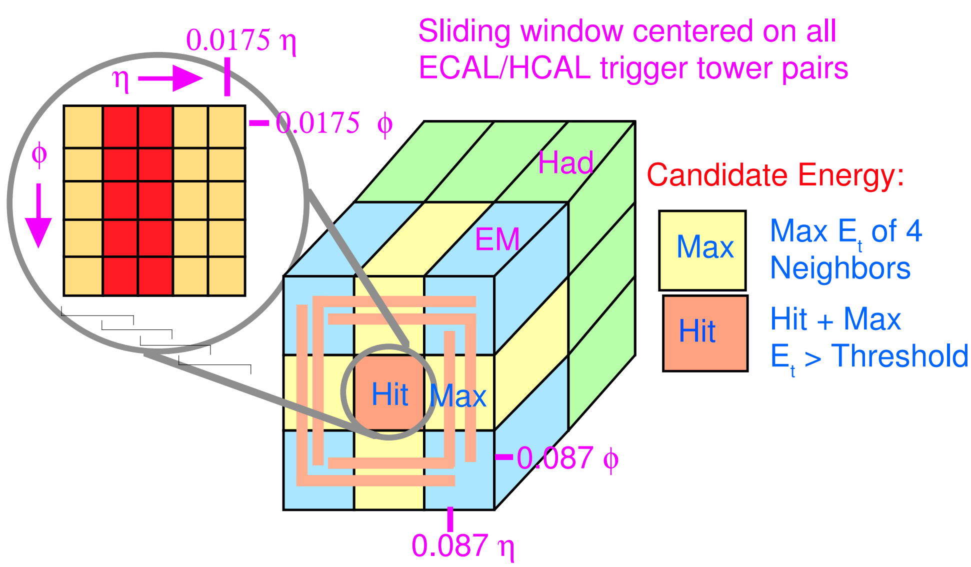

Figure 3.19: Level-1 electron/photon trigger algorithm [93].

Muon Trigger

The muon trigger involves the whole muon system, including DT, CSC, and RPC. The DT local trigger (Fig. 3.20) reconstructs muon candidates from DT chambers in the form of track segments in the ϕ-projection and hit patterns in the η-projection. Bunch and Track Identifier (BTI) identifies the rough muon track for each station, given that at least three hits present in different planes of superlayer. The BTI has a resolution of 1.44 mm on the impact position and 60 mrad on track direction. Track Correlator (TRACO) further improves angular resolution to 10 mrad by correlating track segments information from two Φ-type superlayers (measuring in the ϕ coordinate), and provides trigger information, such as transverse momentum, position in the detector, and bending angle of the track. There are 25 TRACO units, where each one sends at most two reconstructed track segments per bunch crossing to Trigger Servers (TS). Trigger Servers process output from TRACO for ϕ position, as well as output directly from BTI readout of Θ-type superlayers. Track segments are transmitted to Drift Tube Track Finder (DTTF), where full muon path is reconstructed.

A CSC consists 6 layers of cathode strips to measure the ϕ-coordinate, and anode wires to identify the muon passing time at high efficiency. The muon track segment is reconstructed by the Local Charge Tracks (LCT), as demonstrated in Figure 3.21. The best two track segments of LCT, measured in the ϕ-coordinate, bending angle, η-coordinate and bunch crossing number, are sent to the CSC Track Finder (CSCTF).

The track finder algorithms (Fig. 3.22) of DTTF and CSCTF work in similar way by joining and extrapolating segments from local triggers. A pairwise matching is done for segments at consecutive stations. An extrapolated coordinate is then calculated using first hit position and bending angle. Two segments are consider as

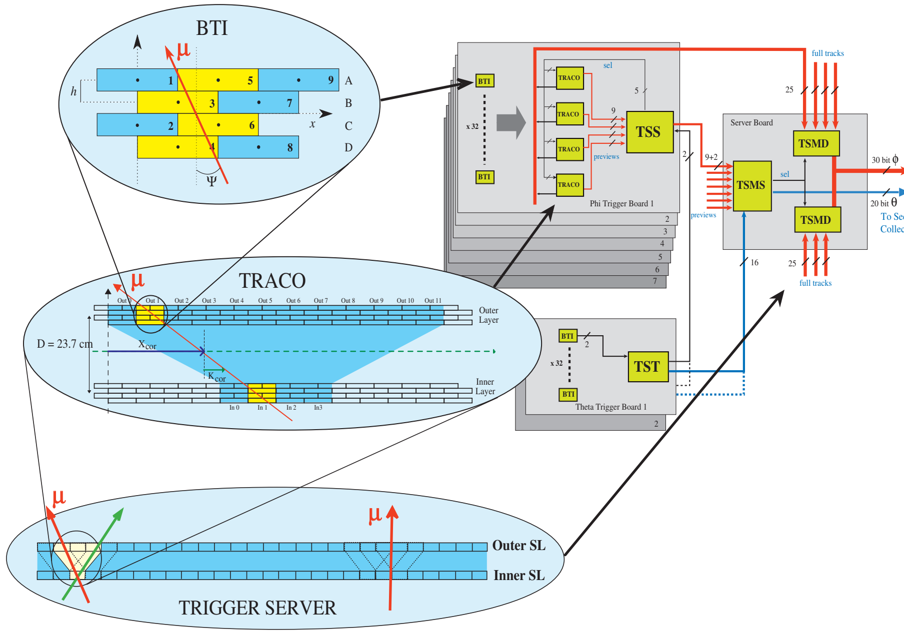

Figure 3.20: Layout of Drift Tube Local Trigger [87].

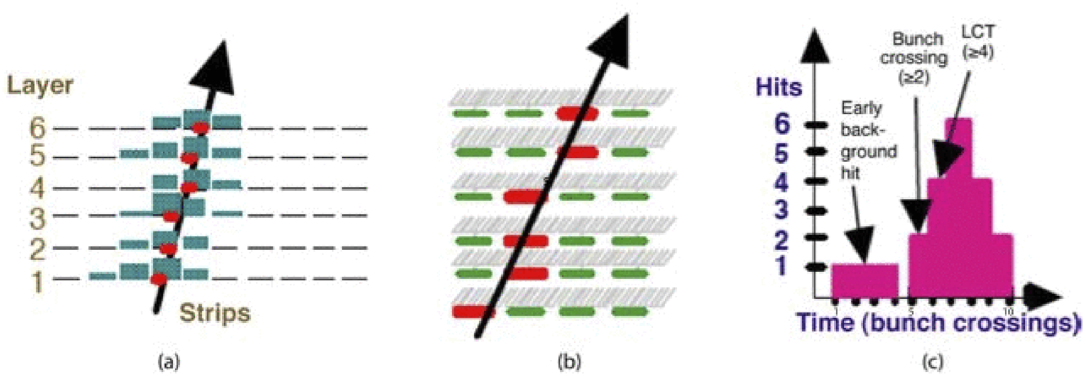

Figure 3.21: Layout of Cathode Strip Chamber Local Trigger and its Local Charge Tracks. (a) Showers from cathode strips. (b) Hit patterns from anode wires. (c) Bunch crossing assignment. [87].

a match if the second hit was found in the extrapolated region by the first hit. The matching-extrapolation procedures are performed for every pairs, where segments are assembled as a muon candidate. Each of DTTF and CSCFT sends at most four muon candidates, with track momentum, position and a quality word, to the Global Muon Trigger (GMT).

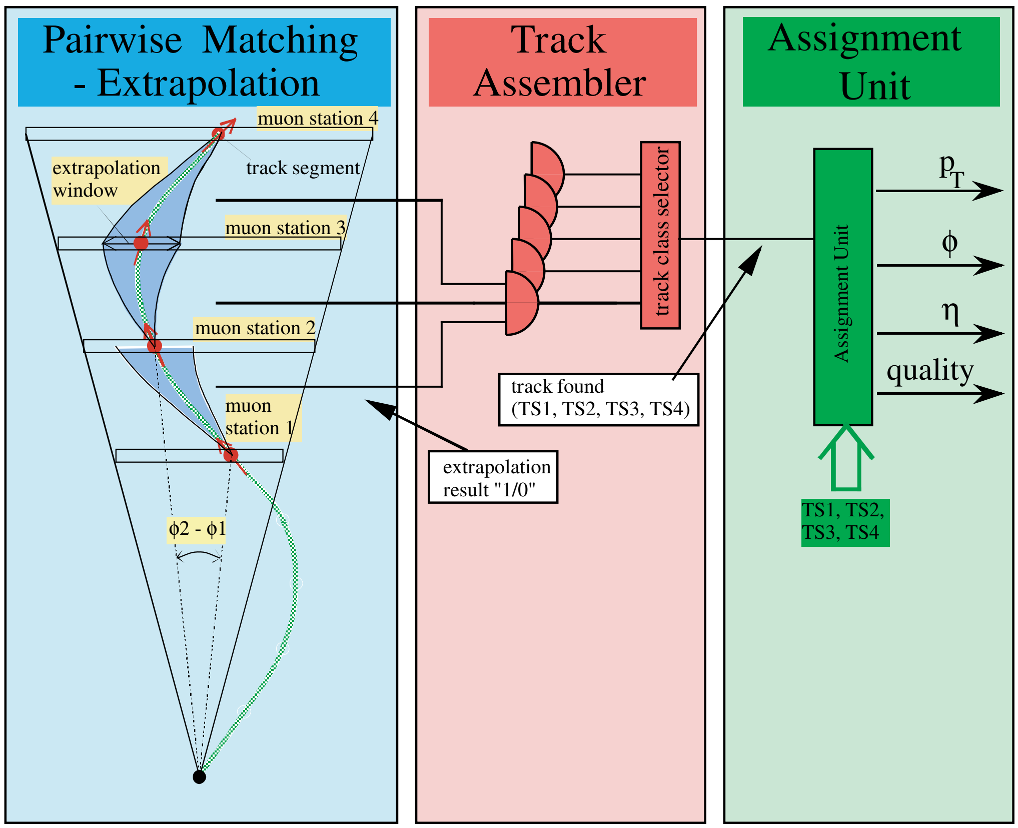

Figure 3.22: Level-1 muon track finder algorithm. [93]

The output of RPC is directly feed to the GMT without track finding. It requires three coincidence hits out of four stations, and does a pattern recognition by the Pattern Comparator Trigger (PACT). The pattern is predefined to assign muon momentum and charge, and loaded into the PACT. At most four candidates, along with the DT and the CSC muon candidates, are sent to the GMT. The best muon candidate requires either DT/RPC or CSC/RPC coincidence, or high quality word in a single muon system. The GMT sorts and sends at most four muon candidates to the GT, ranked by their transverse momentum and quality.

3.2.7 Data Acquisition and Computing

The Data Acquisition (DAQ) system of the CMS collects data from the LHC collisions at a bunch crossing frequency of 40 MHz. The architecture of the CMS DAQ system is shown in Fig. 3.23. Once an event is accepted by the Level-1 trigger system, readout from all detector front-ends are transmitted to an event builder network of a data flow rate of 100 GB/s. Given an average event size of 1.5 MB, a strict limitation on Level-1 output at 100 kHz is required to avoid overflow of the DAQ system. The event readout from about 650 data sources is distributed to a software filter system, i.e. High Level Trigger (HLT), to further reduce rate of stored events to 100 Hz. The HLT runs fast offline reconstruction to select event based on the properties of the trigger objects. Some common trigger selection criteria is to select events with trigger candidates above a certain (transverse) energy thresholds. Trigger candidates can be a single physics object, such as jet, electron, photon and muon; energy sum, such as missing transverse energy (MET) and sum of transverse energy of all jet above a threshold (HT); multiple objects, such as four jets, HT plus MET,etc. The HLT is also set to direct pass-through of particular L1 bits, which allows local system to select events for calibration purpose. Events passed by HLT are stored into several data streams, or primary data set, according to trigger conditions. Some common data stream for physics analysis are Jet, Electron/Photon (EG), Muon (Mu), as well as MET and forward jets (METFwd).

Event stored by DAQ system are in RAW format, where all readout from every system are recorded. The metadata of RAW event also provide a record of trigger decision, number of runs and events. All RAW data are stored permanently at Tier-0

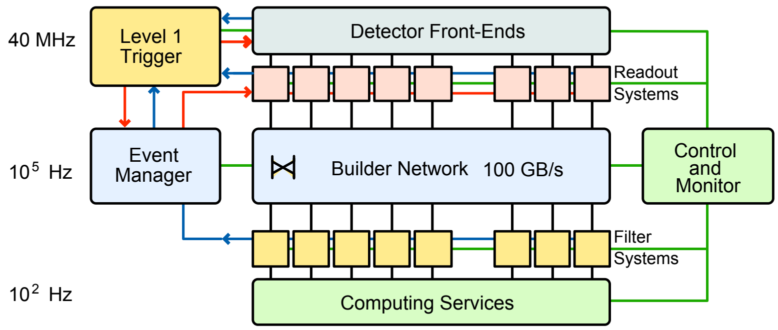

Figure 3.23: Architecture of the CMS Data Acquisition system [87].

center hosted at CERN. A Tier-0 center accepts data from online system with small latency, and carries out prompt reconstruction from RAW data. The reconstructed (RECO) data contains high-level physics objects, and a full record of reconstructed hits and clusters that used in reconstruction algorithms. A skimmed version of RECO format, Analysis Object Data (AOD), is designed to keep certain high-level physics objects parameters in 100 kB per event, which boost user performance for analyzing large amount of data. A few Tier-1 centers are hosted around the world at national labs (e.g. Fermilab) and computing centers. Tier-1 centers store backup copies of RAW from CMS, and hold a full copy of AOD data, as well as a fraction of simulated events and RECO data. Tier-2/3 centers are hosted at local CMS institutes, which provide local storage and computing power for local users.

3.2.8 Luminosity Measurement

The measurement of luminosity by the CMS is not only for monitoring the LHC performance, but also plays an important part in overall normalization for physics analysis, such as precise cross section measurement of physics process. There are two techniques of online luminosity measurement by HF: zero counting and energy sum.

The zero counting method calculates the fraction of quiet HF towers per bunch crossing and estimate the average number of interactions. The number of inelastic and diffractive interactions n per bunch crossing is given by a Poisson distribution

$$p(n|\mu) = \frac{\mu^n e^{-\mu}}{n!}, \tag{3.3}$$

where μ is the average number of interactions. The fraction of quiet HF towers can be used to estimate the probability of observing zero number of interaction $p(0)$, which implies

$$\mu = -\ln p(0). \tag{3.4}$$

On the other hand, the number of interactions can be calculated by a given instantaneous luminosity $\mathcal{L}$, cross section of inelastic and diffractive interactions $\sigma = 80$ mb, and the effective bunch crossing rate $f_{\mathrm{BX}} = 2808/3564 \times 40$ MHz, as the following equation

$$\mu = \frac{\sigma \mathcal{L}}{f_{\mathrm{BX}}}, \tag{3.5}$$

which implies that the fraction of quiet HF towers is directly proportional to the instantaneous luminosity, as shown in Figure 3.24. The zero counting method does not perform well at high luminosity, because the systematic uncertainties become unmanageable as the fraction of zeros is very small. Therefore, the linear response drops at the LHC designed luminosity $\mathcal{L} = 10^{34}\,\mathrm{cm}^{-2}\,\mathrm{s}^{-1}$ (Fig. 3.24).

The second method of luminosity measurement is from the linear relation between the sum of the transverse energy in HF and the number of interactions (Fig. 3.25).

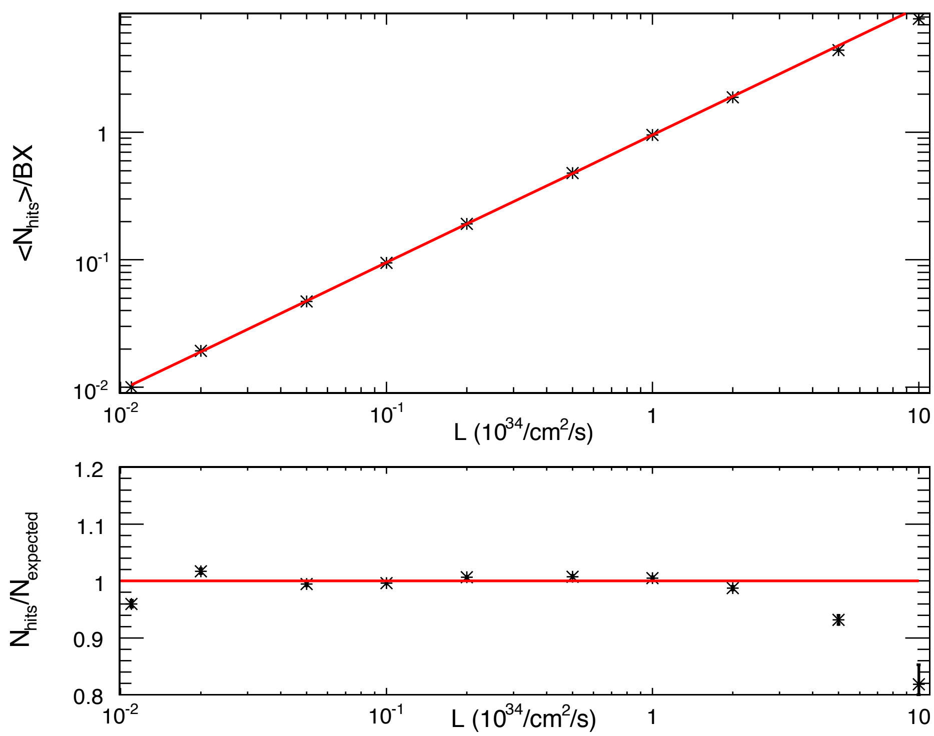

Figure 3.24: Luminosity measurement by zero counting method [96]. The upper panel shows the linearity of the fraction of quiet HF towers *vs.* the instantaneous luminosity. The lower panel shows the linear response as a function of instantaneous luminosity.

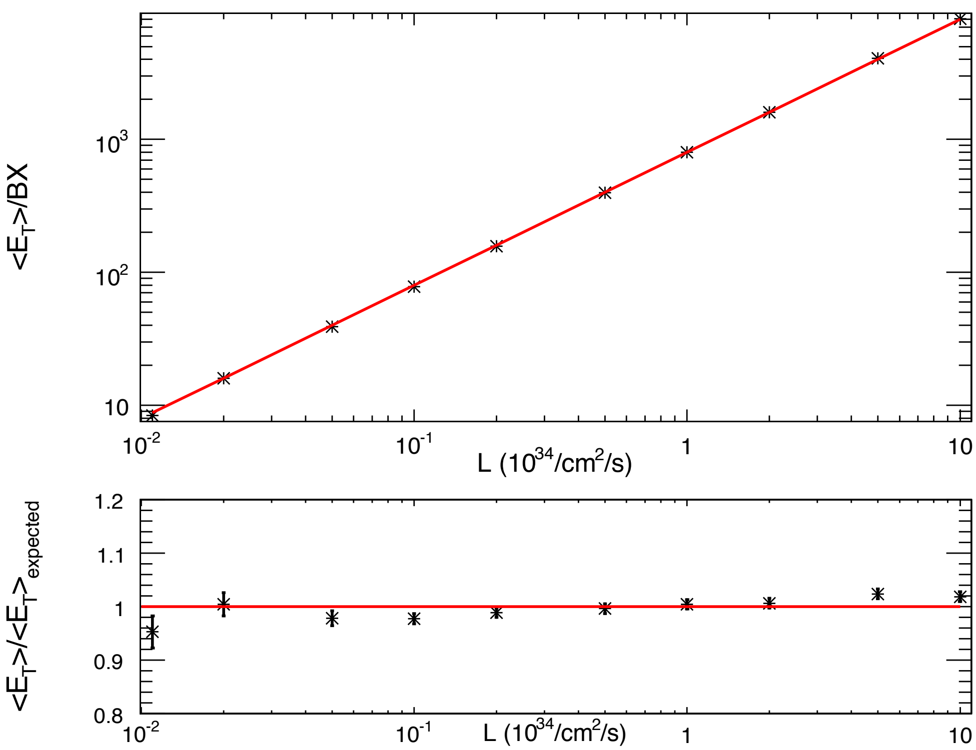

Figure 3.25: Luminosity measurement by summing the HF transverse energy [96]. The upper panel shows the linearity of the HF transverse energy sum *vs.* the instantaneous luminosity. The lower panel shows the linear response as a function of the instantaneous luminosity.

Chapter 4

Analysis

4.1 Particle Identification

As the evaporation of a microscopic black hole results in a wide variety of final states, all types of particles (jets, photons, electrons, muons, and $\not{E}_T$) are included in this analysis. Reconstructed particles are produced by standard CMS event reconstruction algorithms for generic physics analyses. Additional requirements on standard reconstructed candidates, recommended by CMS Exotica group and physics analysis object (POG) group, are applied for searching for new physics phenomena. Details of particle identification are discussed in this section.

Further cross-cleaning is imposed such that the separation of any two selected objects (jet, lepton, or photon) is required to be

$$\Delta R = \sqrt{\Delta\phi^2 + \Delta\eta^2} > 0.3. \tag{4.1}$$

In order to avoid double-counting in an event, overlapped objects are removed in the following order:

- an electron overlapped with muon is removed,
- a photon overlapped with electron is removed,
- a jet overlapped with an electron or a photon is removed.

The event multiplicity (N) is defined as the number of selected jets, leptons and photons with transverse energy above 50 GeV. The total transverse energy (S_{T}) is defined as the scalar sum of the transverse energies of all the selected objects with transverse energy above 50 GeV, including $\not{E}_T$. The 50 GeV transverse energy threshold is chosen to suppress the standard model background and minimize the effect from pile-up jets, while maintaining full efficiency for black hole decay products. Since tau has a very short lifetime, it is counted as an electron, muon, or a jet.

4.1.1 Muons

Muon candidates are required to pass Tight Muon Selection, as used in CMS electroweak analyses [97], within $|\eta| < 2.1$. The selection requires the muon candidate to be a global muon and a tracker muon. Global muon reconstruction (outside-in) starts from muon tracks in the muon spectrometer that are further matched with tracker tracks. A global-muon track is fitted by combining muon track and tracker hits. Track muon reconstruction (inside-out) takes all tracker tracks with $p_{\mathrm{T}} > 0.5\,\mathrm{GeV}$ and $p > 2.5\,\mathrm{GeV}$ as muon candidates. Extrapolated tracks with expected energy loss and uncertainty due to multiple scattering are then matched to at least one muon segment. The normalized χ^2 of global muon track fit must be less than 10.

At least one muon chamber hit is included in the final track fit, and matched to a muon segment in at least two muon stations. For the corresponding track tracker, it must contain at least 10 hits, including 1 pixel hit. To suppress muon from cosmic background, the transverse impact parameter must be with 2 mm of the primary vertex (Fig. 4.1).

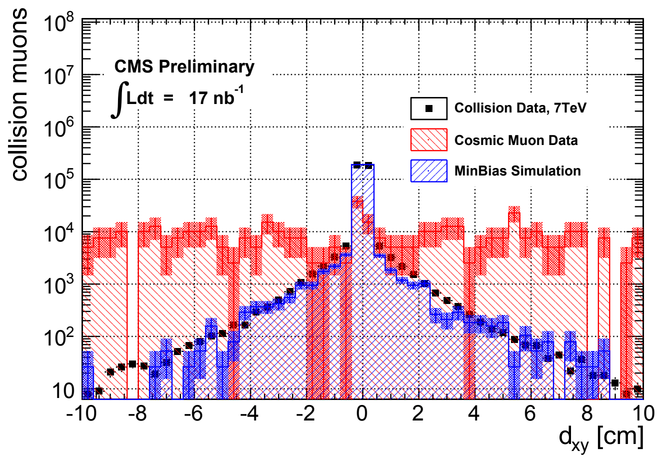

Figure 4.1: Transverse impact parameter of reconstructed muon from collision and cosmic rays with respect to primary vertex [98].

4.1.2 Electrons

Electrons and photons are reconstructed in the fiducial volume of the barrel ($|\eta| < 1.44$) and the endcap ($1.56 < |\eta| < 2.4$). The electron reconstruction is ECAL-driven: the algorithm starts with ECAL superclusters [96]. A supercluster is a group of energy clusters deposited in ECAL with narrow width in η coordinate, and spread in ϕ coordinate due to the bending of electrons in the magnetic field. With a selected supercluster, the algorithm searches the corresponding pixel hits (seeds), and reconstructs a track in the silicon tracker. The trajectory of the electron candidate is determined by fitting the supercluster and track with Bremsstrahlung energy loss model with the Gaussian Sum Filter (GSF) [99]. The reconstructed electron must be matched to its associated track with $|\Delta\eta_{\text{in}}| < 0.005$ (0.007) for barrel (endcap), and $|\Delta\phi_{\text{in}}| < 0.09$, where the track position is measured in the inner layer of the tracker. Since ECAL crystals in the endcap are larger in η-dimension, a maximum threshold of $\sigma_{i\eta i\eta} < 0.03$ is applied on the spread of energy in the 5×5 array. As an electron candidate deposits most of its energy in the ECAL, the hadronic energy fraction, measured in a cone of radius 0.15 centered on the electron's position, is relatively small ($H/E < 5\%$). To further reduce the misidentified electrons from jets, additional isolation cuts are applied. The hadronic isolation is defined as the sum of HCAL transverse energy, calculated separately for depth 1 and 2, in a shape of ring with the radius from 0.15 to 0.3 centered on the electron's position. For an electron candidate with transverse energy E_{T}, the hadronic depth 1 isolation are: less than $2 + 0.03 \times E_{\mathrm{T}}/\,\mathrm{GeV}$ in barrel; less than $2.5 + 0.05 \times \max(0, (E_{\mathrm{T}} - 50)/\,\mathrm{GeV})$ in endcap. The hadronic depth 2 isolation, only applicable to endcap, is less than $0.5/\,\mathrm{GeV}$. The sum of all tracks p_{T}, excluding the one matched to the electron candidate, within an annular region of radius between 0.04 and 0.3 is required to be less than 7 GeV (15 GeV) in barrel (endcap).

4.1.3 Photons

Similar to electrons, photons are reconstructed by ECAL-driven algorithm inside the ECAL fiducial volume. No tracker track, and hence pixel seed, is associated with photon candidate. Same hadronic energy fraction $H/E < 5\%$ requirement as for electrons is applied. The ECAL isolation, sum of ECAL transverse energy around the photon candidate with transverse energy E_{T} in an annular region of radius from 0.15 to 0.4, is required to be less than $4.2 + 0.006 \times E_{\mathrm{T}}/\,\mathrm{GeV}$. The HCAL isolation, sum of HCAL transverse energy (including depth 1 and 2) in an annular region of radius from 0.15 to 0.4, is required to be less than $2.2 + 0.0025 \times E_{\mathrm{T}}/\,\mathrm{GeV}$. The tracker isolation, sum of all tracks p_{T} within a hollow cone of radius from 0.04 to 0.4, is required to be less than $2.0 + 0.001 \times p_{\mathrm{T}}$. The requirement on energy spread in η coordinate is $\sigma_{i\eta i\eta} < 0.013$ (0.030) in barrel (endcap).

4.1.4 Jets

Jets are reconstructed by using the energy deposited in the HCAL and ECAL with $|\eta| < 2.6$, clustered using a collinear and infrared safe anti-k_T algorithm [100] with a distance parameter 0.5. Following jet quality selections [101] are applied to reject misreconstructed jets from calorimeters and readout electronic noises:

- Electromagnetic fraction greater than 0.01;
- The number of calorimeter cells containing 90% of jet energy is greater than 1;
- The fraction of jet energy in the hottest Hybrid Photodiode (HPD) of HCAL readout is less than 98%.

Jet energies are corrected in a sequence of factorization: offset, relative and absolute corrections. The offset correction aims to correct the excess energy due to electronics noise and pile. The relative correction removes variations of jet response in η coordinate with reference to the central control region. The absolute correction removes the variations as a function of jet p_{T}. The above corrections are derived using Monte Carlo simulation data, where raw reconstructed jets are corrected with respect to corresponding parton jets, as well as collisions data [102]. An extra correction, residual correction, is derived from data to remove any bias for jet p_{T} and η distributions with respect to MC simulation. All of the above corrections are provided by CMS JetMET group as "Spring10" corrections [102].

4.1.5 Missing Transverse Energy

Missing transverse energy $\not\!\!E_T$ is reconstructed as the negative of the vector sum of transverse energies in the calorimeter towers. Since muon deposits very little energy in the calorimeters, muon p_T measured by muon spectrometer is accounted for in the calorimetric $\not\!\!E_T$, while associated hits in the calorimeters are removed. To remove $\not\!\!E_T$ bias from non-linear response of the calorimeters and unclustered energies, further correction (type-I) is applied. The difference between $\not\!\!E_T$ and the negative vector sum of p_T of photons, electrons, muons, and corrected jets is parameterized as a function of $\not\!\!E_T$, and the average values are applied on top of raw calorimetric $\not\!\!E_T$.

4.2 Event Selection

Data taken by CMS are stored in primary datasets according to the trigger selection. In particular, H_T trigger, defined as the scalar sum of HLT jet transverse momenta above a threshold, provides the source of events for this analysis. At the HLT , jets are not cleaned via particle identification. Electrons and photons, interacted mostly with ECAL, are reconstructed as jets and thus counted toward H_T. Therefore, the H_T is a robust trigger for physics analysis using variable multiple final states. Special cases with high-p_T muons and high-$\not\!\!E_T$ are discussed in Section 4.6.1. In 2010 data, H_T is calculated without jet energy correction with a jet E_T threshold of 30 GeV. The HLT decisions are Boolean bits, which can be accessible by the trigger name, such as HLT_HT100U. The suffix 100U indicates the trigger threshold for $H_\mathrm{T} > 100$ GeV calculated from uncorrected jets. The trigger threshold was increased to 200 GeV at the end of 2010 in order to maintain reasonable trigger rate at high luminosity. Wildcard selection HLT_HT* is used to pick up all events triggered by H_T at various thresholds. The trigger efficiency of H_{T} is evaluated using minimum bias dataset, as shown in Fig. 4.2. For $S_{\mathrm{T}} > 600$ GeV, the efficiency of the H_{T} trigger is almost at 100%. Table 4.1 lists all datasets used in this analysis with H_{T}-triggered events, giving a total integrated luminosity of 34.7 ± 3.8 pb^{-1} of data. Since all types of particles are possible signatures for black hole evaporation, all CMS subdetectors are required to be in good operational conditions. Therefore, the total luminosity used in the analysis is less than the total luminosity delivered by LHC (~ 50 pb^{-1}). Lists of good events are provided by the CMS data certification group.

Table 4.1: Year 2010 dataset with H_{T}-triggered events.

Dataset	Run Number	$\int \mathcal{L}dt$ (nb^{-1})
/MinimumBias/		
Commissioning10-Sep17ReReco_v2/RECO	132440-135735	7.95
/JetMETTau/Run2010A-Sep17ReReco_v2/RECO	136035-141881	172.08
/JetMET/Run2010A-Sep17ReReco_v2/RECO	141956-144114	2895.80
/Jet/Run2010B-PromptReco-v2/AOD	146428-149294	31665.42
Total	132440-149294	34741.25

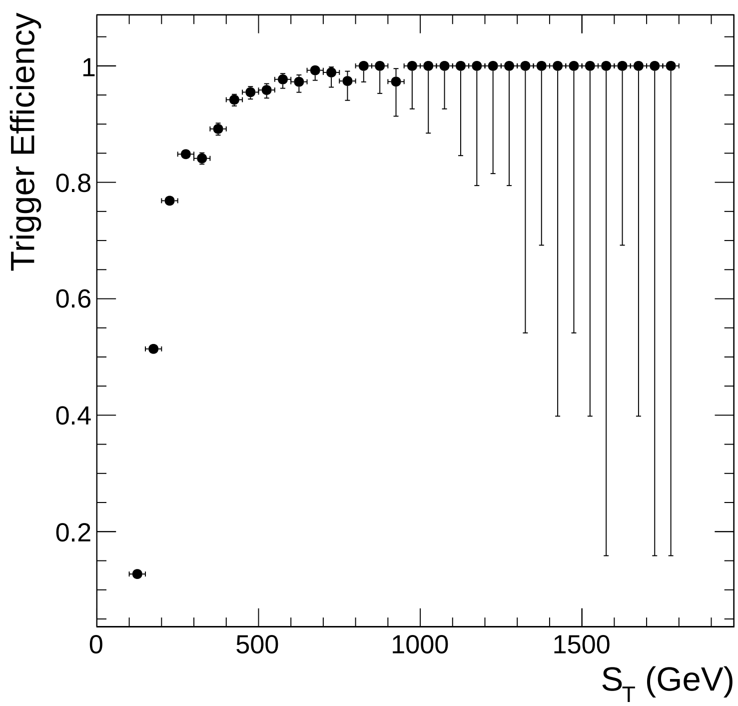

Figure 4.2: Trigger efficiency of HLT_HT* as a function of S_{T}.

4.3 Background Estimation

The dominant multi-jet background cannot be determined from Monte Carlo simulation because it requires non-perturbative higher order QCD calculations. Therefore, the QCD multi-jet background is estimated from data. The main contribution of QCD events is coming from the hard $2 \to 2$ parton scattering process, and the jet-splitting through initial state radiation (ISR) and final state radiation (FSR) forms multi-jet state, as illustrated in Fig. 4.3. The ISR/FSR jet-splitting is nearly collinear with incoming/outgoing partons, and hence the shape of S_{T} distribution is expected to be independent of event multiplicity, provided that S_{T} is sufficiently above the turn-on region.

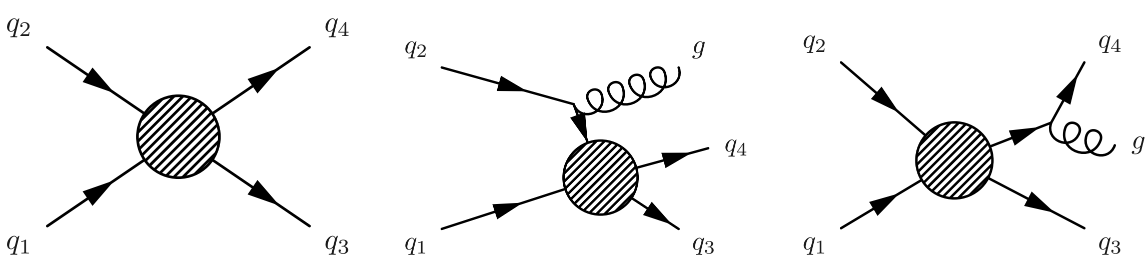

(a) QCD $2 \to 2$ **(b)** ISR **(c)** FSR

Figure 4.3: Illustrations of the hard $2 \to 2$ parton scattering process; jet splitting through initial state radiation (ISR) and final state radiation (FSR).

The assumption of the S_{T} shape invariance is confirmed with simulated QCD events, which are generated by PYTHIA or ALPGEN using CTEQ6L PDF set [103], and followed by full CMS detector simulation via GEANT4 [104]. Figure 4.4 shows the S_{T} distributions, up to an arbitrary scaling factor, for different PYTHIA event jet multiplicity. The shape of S_{T} distribution is invariant up to event multiplicity five, provided that S_{T} is greater than the turn-on region at about 1 TeV. The invariant mass distribution also exhibits similar invariance (Fig. 4.5). However the invariant mass (i.e. total energy in the event) is sensitive to pile-up and object threshold, which is not uniform in energy. Therefore, S_{T} is a more robust variable for this analysis.

Other sources of backgrounds, such as direct photon, W/Z+jets, and $t\bar{t}$ production were generated by MadGraph [105] with CTEQ6L PDF set, followed by pythia and full CMS detector simulation via geant4. These backgrounds are negligible and contribute less than 1% (Fig. 4.17). The number of expected background is completely determined by data-driven method. None of the above background simulations are included in the final analysis procedures.

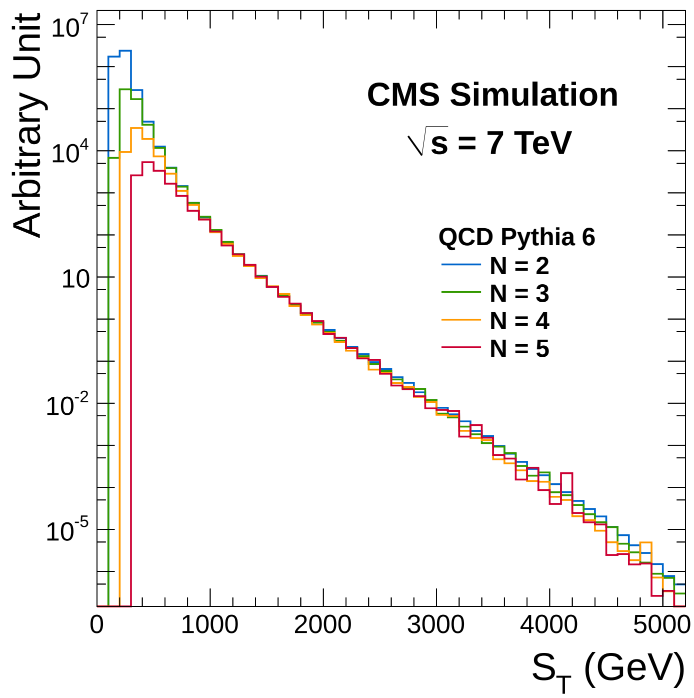

Figure 4.4: The S_{T} distribution of simulated QCD multi-jet events. The shape is independent of event multiplicity N.

4.3.1 Background Templates

To test the S_{T}-shape-invariance assumption in data, the background templates are modeled from event multiplicity $N = 2, 3$ exclusively. The S_{T} distribution of multiplicity $N = 2$ and $N = 3$ are obtained from data and fitted with the following parameterizations, inspired by CMS dijet analysis [106], in the range of $600\ \text{GeV} \leq S_{\mathrm{T}} < 1100\ \text{GeV}$:

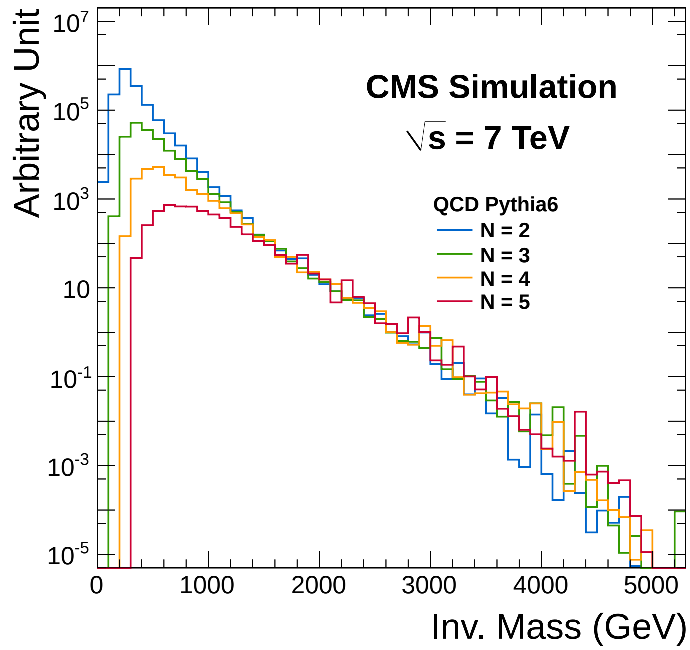

Figure 4.5: The invariant mass distribution of simulated QCD multi-jet events. The property of scaling invariant is similar to S_T distribution, but the invariant mass variable is sensible to pile-up and jet threshold.

0. $\frac{P_0(1+x)^{P_1}}{x^{P_2+P_3\log(x)}}$,

1. $\frac{P_0}{(P_1+P_2x+x^2)^{P_3}}$,

2. $\frac{P_0}{(P_1+x)^{P_2}}$,

where x is S_T (TeV) and P_i are the fit parameters. Table 4.2 and Figure 4.6 show the normalized χ^2 and fitting results for exclusive multiplicities $N = 2$ and $N = 3$. All three parameterizations model the S_T distribution very well at low multiplicity. To confirm the S_T-shape-invariance assumption, fitted curves for multiplicity $N = 2$ are rescaled in the normalization region 1.0 TeV $\leq S_\mathrm{T} < 1.1$ TeV, and overlaid with all parameterizations for multiplicity $N = 3$ (Fig. 4.7). The background uncertainty for S_T shape modeling is determined by the outer envelope of all parameterizations.

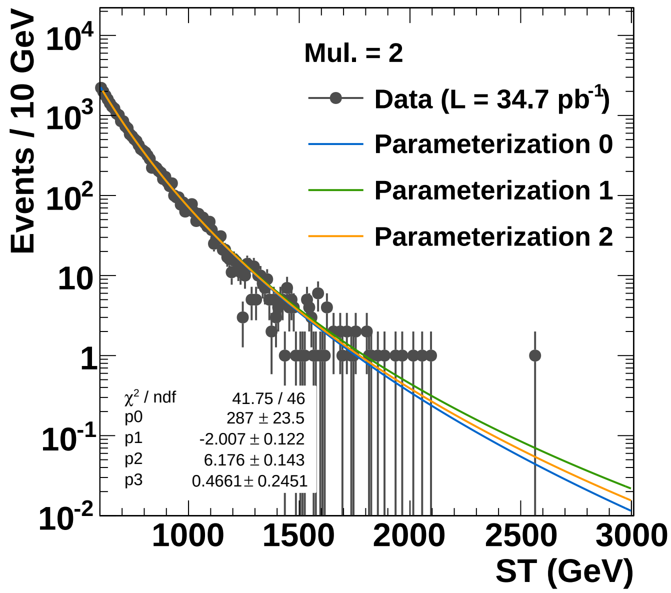

(a) $N = 2$

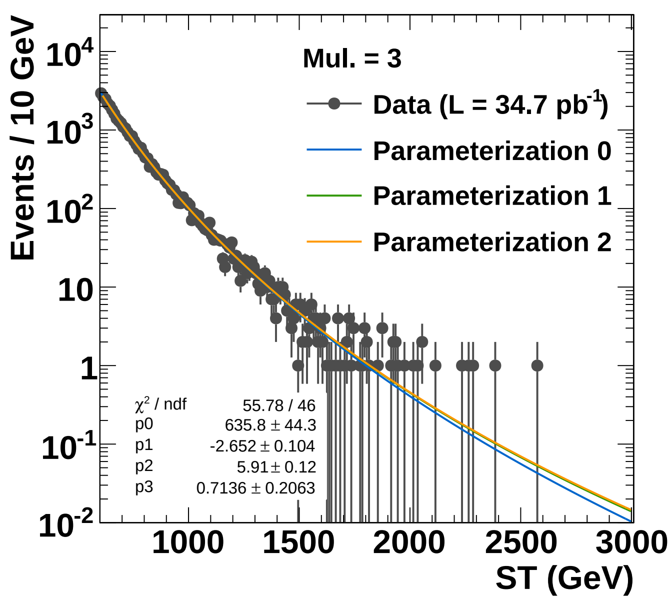

(b) $N = 3$

Figure 4.6: Background templates obtained from data for event multiplicity $N = 2$ and $N = 3$.

Multiplicity	Parameterizations	χ^2 / d.o.f.
2	0	41.75 / 46
	1	41.44 / 46
	2	41.62 / 47
3	0	55.78 / 46
	1	55.81 / 46
	2	55.82 / 47

Table 4.2: Table of χ^2 per degree of freedom (d.o.f.) of S_T parameterizations.

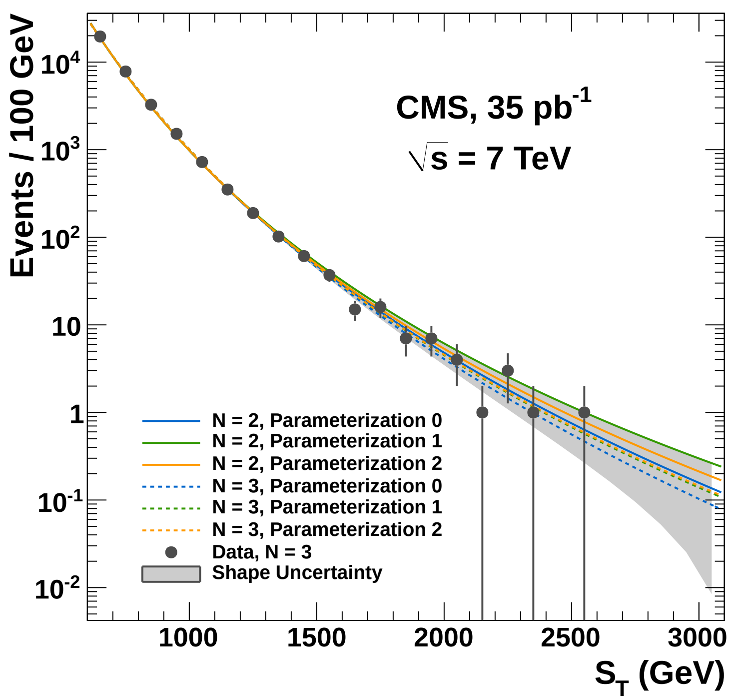

Figure 4.7: Overlays of all S_T parameterizations rescaled to event multiplicity $N = 3$. The shaded region is the uncertainty of shape modeling determined by the outline of all parameterizations.

4.3.2 Background Normalization

The background templates are rescaled to higher event multiplicity to estimate the number of multi-jet background events. The normalization region is chosen to be 1.0 TeV $\leq S_{\mathrm{T}} < 1.1$ TeV, such that it is far away from the S_{T} turn-on region, and does not overlap with the search window, assuming that the minimum black hole mass is 1.5 TeV or above. The rescaling factors and uncertainties are determined by maximum-likelihood estimation. The likelihood function is defined as

$$L = \prod_i \frac{(\lambda f_i)^{n_i} e^{-\lambda f_i}}{n_i!},$$

where i is the bin number of S_{T} histogram in normalization region, λ is the rescaling factor with respect to the template parameterization 0, f_i is the number of events estimated by the template in the i-th bin, and n_i is the number of events in the i-th bin obtained from data at higher event multiplicity. Figure 4.8 shows the log likelihood of rescaling for background estimation of $N \geq 3$ from template $N = 2$. The best estimator is the maximum of the log likelihood distribution, and its uncertainty can be determined by the full width at a half maximum in the log-likelihood $\Delta \ln(L) = -0.5$. Table 4.3 summarizes the rescaling factors of various templates $N = 2, 3$ normalized to data histograms with inclusive multiplicity $N \geq 3, 4, 5$. The total background uncertainty is a Gaussian sum of shape modeling uncertainty and rescaling uncertainty.

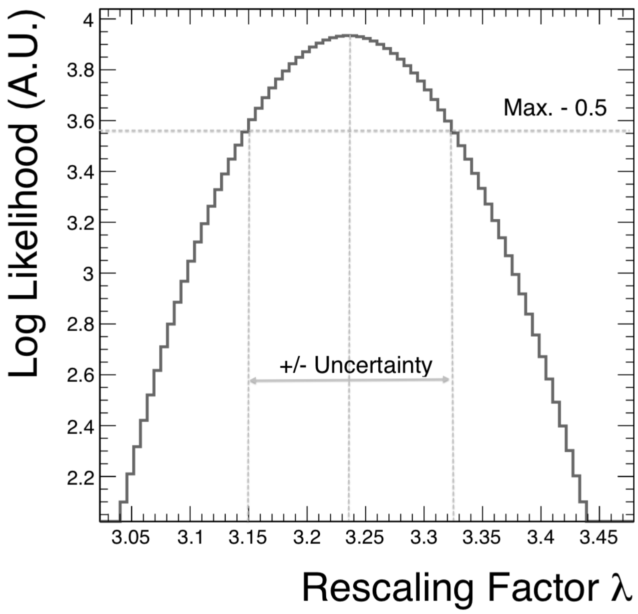

Figure 4.8: Log likelihood distribution of rescaling factor for background estimation of $N \geq 3$ from template $N = 2$.

Template multiplicity	Multiplicity	Rescaling factor
2	≥ 3	3.226 ± 0.112
	≥ 4	1.817 ± 0.084
	≥ 5	0.821 ± 0.057
3	≥ 3	2.286 ± 0.080
	≥ 4	1.288 ± 0.060
	≥ 5	0.582 ± 0.040

Table 4.3: Rescaling factors of various templates $N = 2, 3$ normalized to data histograms with inclusive multiplicity $N \geq 3, 4, 5$.

4.4 Signal Acceptance

Simulated black hole events are generated as described in Section 2.2.4, then followed by PYTHIA hadronization and fast simulation [107] of the CMS detector. The CMS fast simulation is a parametric simulation of detector response, which has been extensively validated for signal events with full simulation by GEANT4. The fast simulation runs 100 to 1000 times faster than full simulation in comparable accuracy [107] (Fig. 4.9). Simulated black hole events of non-rotating, rotating, and stable remnant scenarios are generated in three parameters: the Planck scale in extra dimensions $M_{\mathrm{D}} = 1.5, 2.0, ..., 5.0$ TeV; minimum black hole mass $M_{\mathrm{BH}}^{\mathrm{min}} = M_{\mathrm{D}}, ..., 5.0$ TeV; the number of extra-dimensions $n = 2, 4, 6$. Properties of black hole with fast simulation of CMS detector are shown in Figures 4.10 - 4.12.

In order to maximize discovery potential, thresholds on S_{T} and event multiplicity are optimized according to the significance estimator $n^{\mathrm{sig}}/\sqrt{n^{\mathrm{sig}} + n^{\mathrm{bkg}}}$, where n^{sig} and n^{bkg} are the number of signals and number of expected backgrounds respectively for $S_{\mathrm{T}} > S_{\mathrm{T}}^{\mathrm{min}}$ and $N \geq N^{\mathrm{min}}$. The number of expected backgrounds is estimated using data-driven technique as described in Section 4.3. For each signal model, the thresholds on $S_{\mathrm{T}}^{\mathrm{min}}$ and N^{min} are chosen such that the significance is maximum (Fig. 4.13). Lists of optimal thresholds are presented in Tables 4.5- 4.7.

4.4.1 Systematic Uncertainty

The uncertainty on signal efficiency is dominated by the jet-energy-scale uncertainty of $\approx 5\%$ [102], which roughly shifted S_{T} spectrum by $\pm 5\%$ (Fig. 4.14a). The effect on the signal acceptance uncertainty is in the order of 5% at the optimal selection

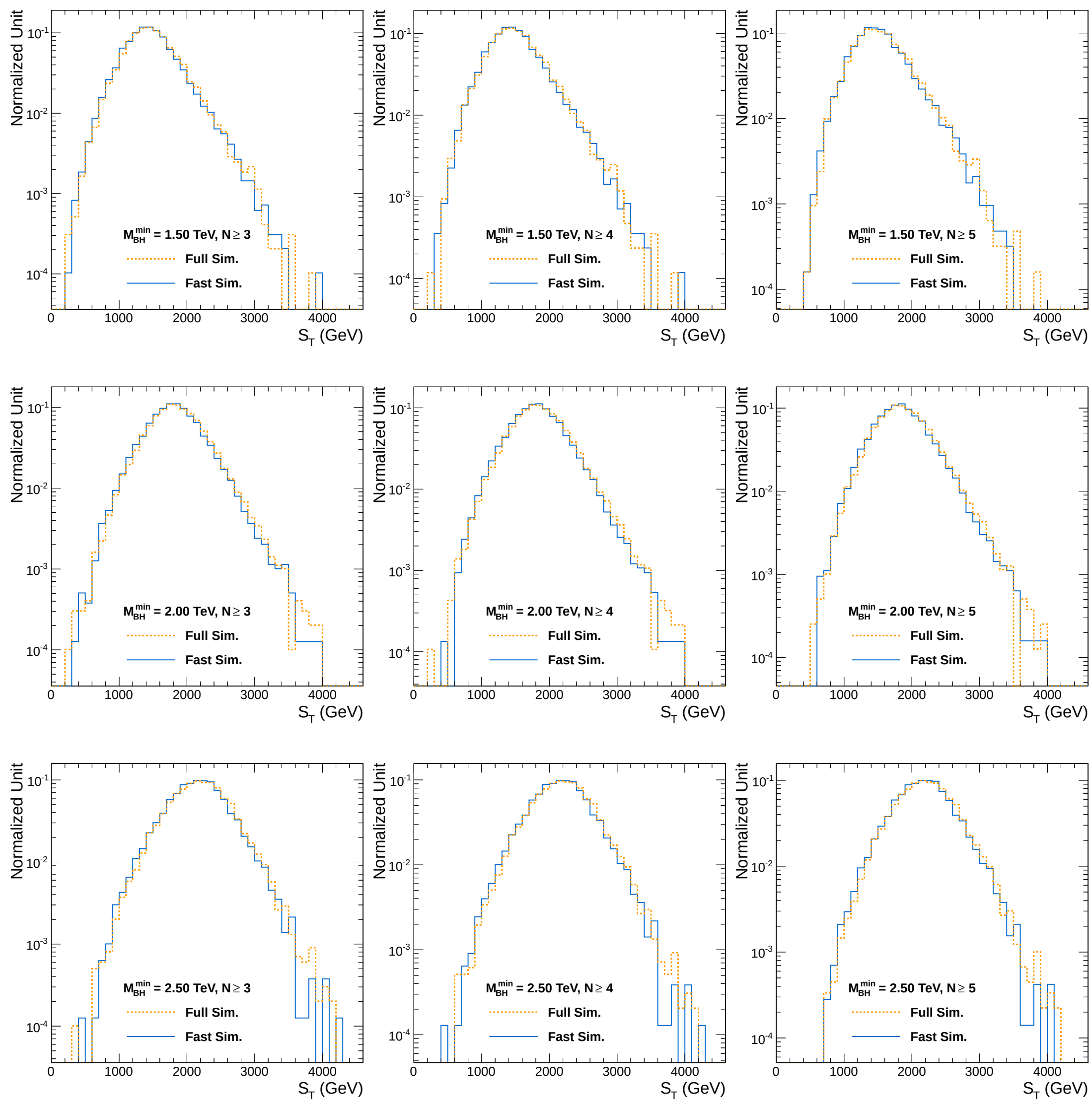

Figure 4.9: Full and fast simulations of CMS detector for simulated non-rotating black hole events with Planck scale $M_{\mathrm{D}} = 1.5$ TeV, extra-dimensions $n = 2$.

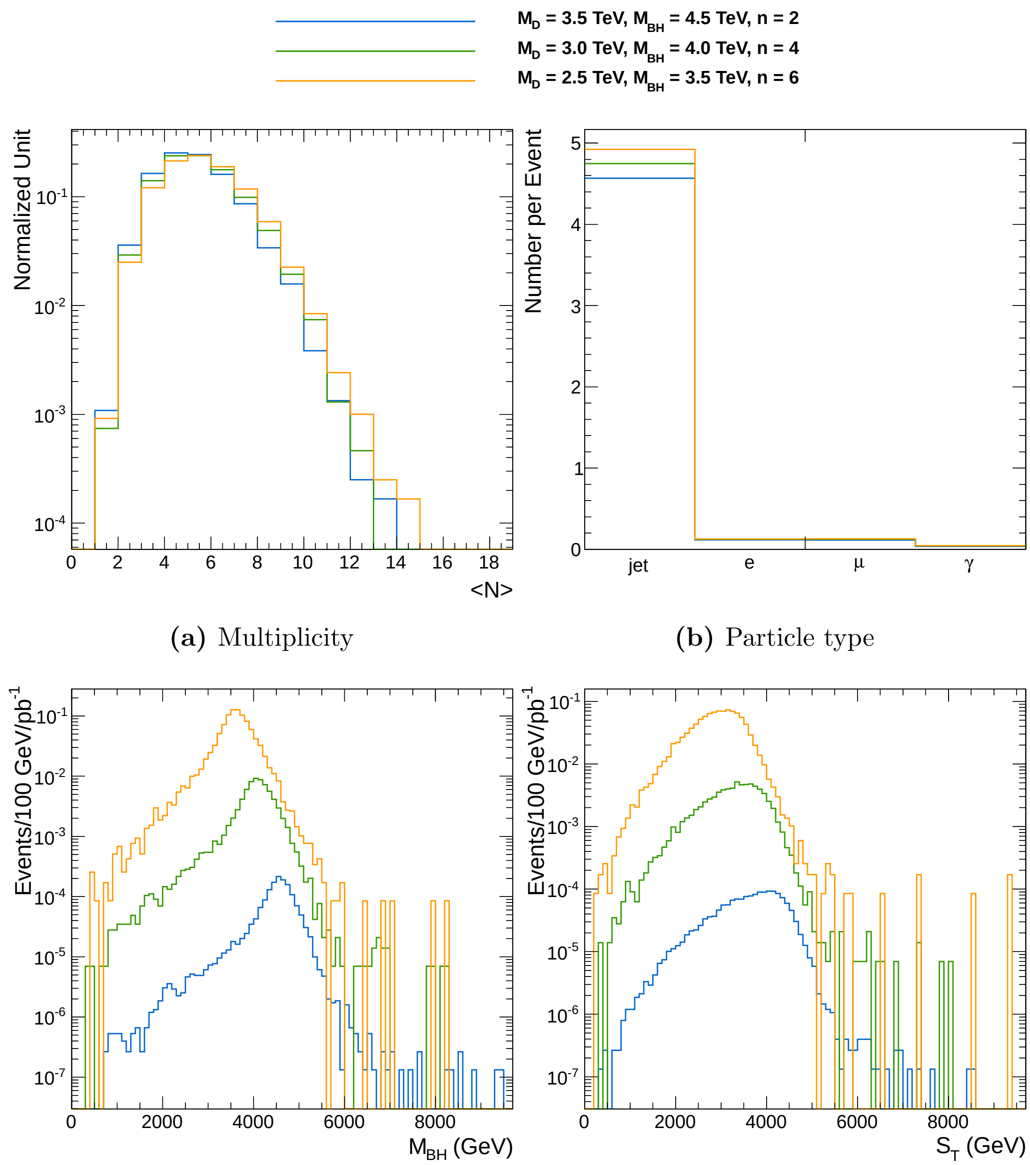

(a) Multiplicity

(b) Particle type

(c) Mass

(d) Scalar p_{T} sum

Figure 4.10: Properties of non-rotating black hole events generated by BlackMax, followed by fast simulation of CMS detector.

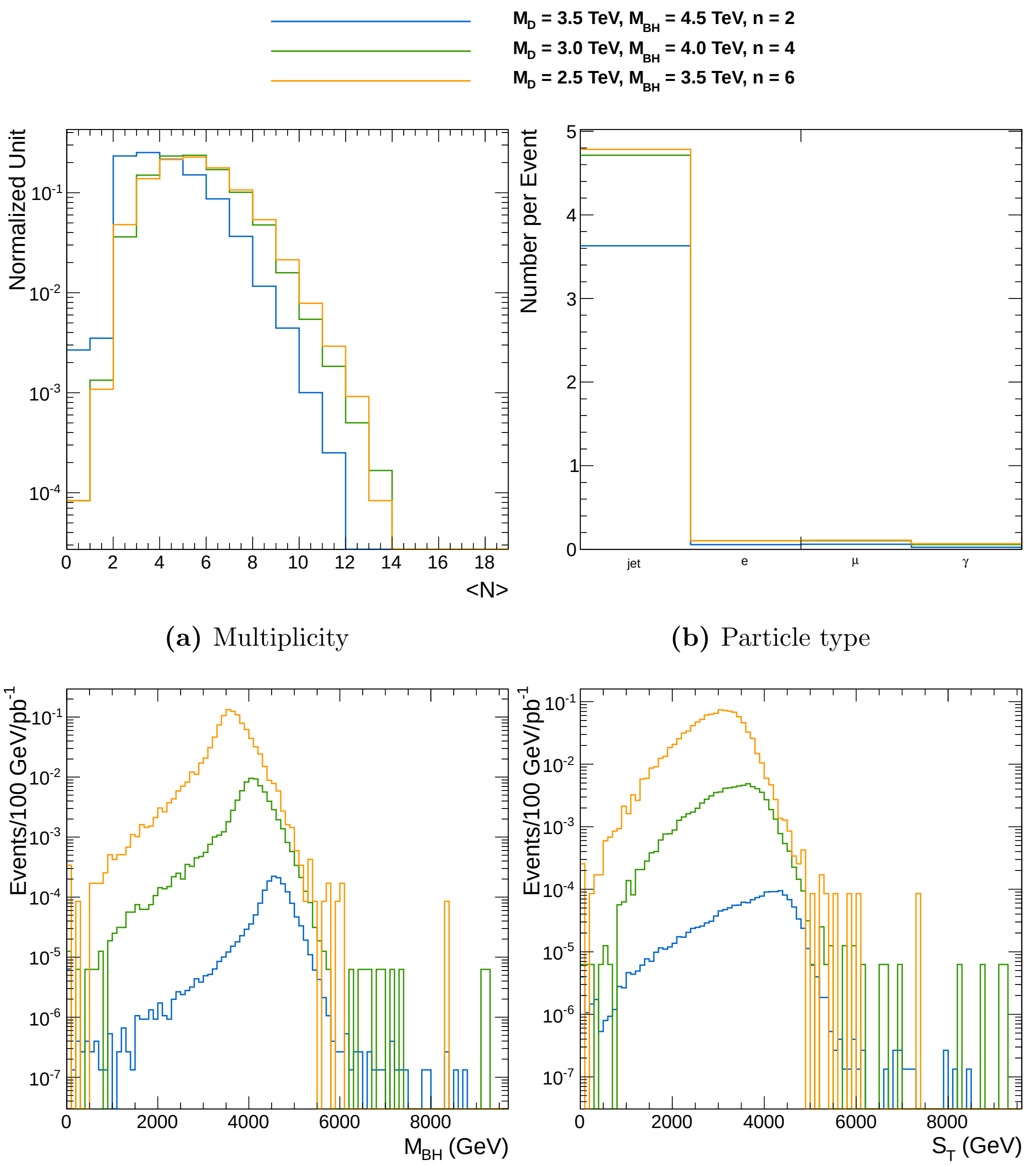

(a) Multiplicity

(b) Particle type

(c) Mass

(d) Scalar p_T sum

Figure 4.11: Properties of rotating black hole events generated by BlackMax, followed by fast simulation of CMS detector.

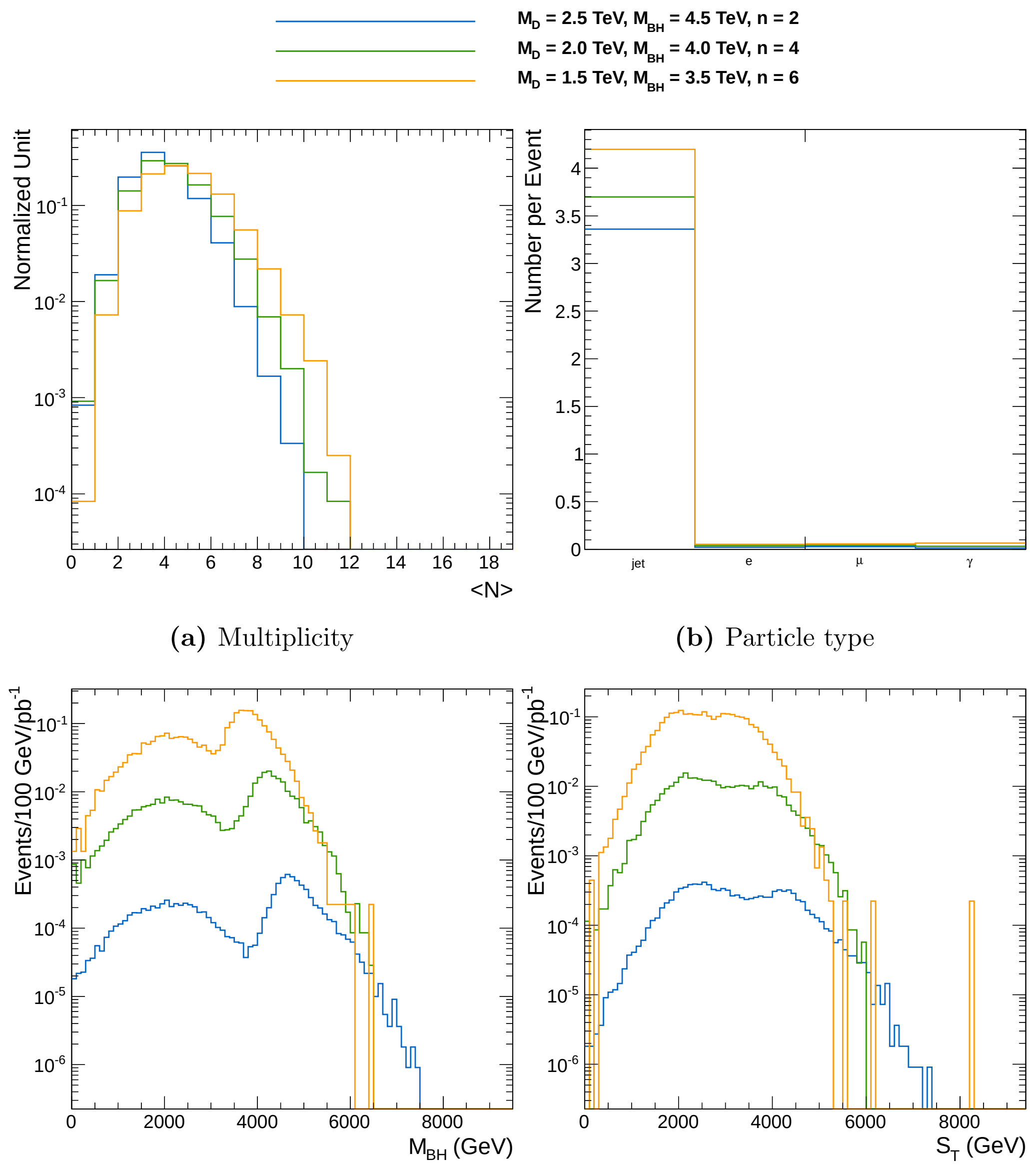

(a) Multiplicity

(b) Particle type

(c) Mass

(d) Scalar p_{T} sum

Figure 4.12: Properties of black hole with stable remnant events generated by CHARYBDIS, followed by fast simulation of CMS detector.

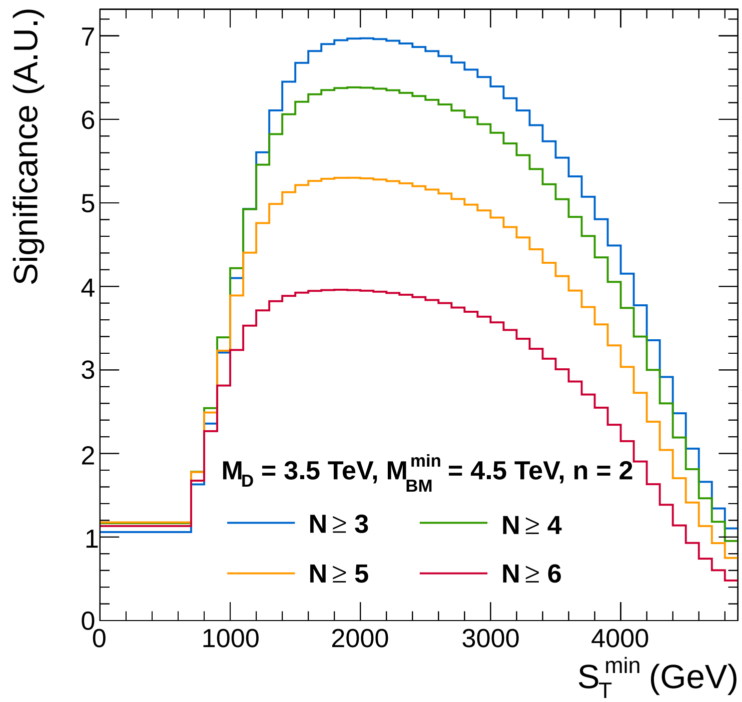

Figure 4.13: Cut optimization using significance estimator.

(Fig. 4.14). Other sources of energy-scale uncertainties, such as leptons, photon and $E_{\mathrm{T}}^{\mathrm{miss}}$, are negligibly small because of the multi-jet dominant nature of the events.

The second major source of uncertainty on signal efficiency is from the variations of parton distribution function (PDF) sets. Each event is weighted with respect to reference PDF set [108]:

$$w(x_1, x_2, Q) = \frac{f_1'(x_1, Q) \times f_2'(x_2, Q)}{f_1(x_1, Q) \times f_2(x_2, Q)},$$

where x_i are the momentum fractions carried by the two colliding partons, Q is the energy scale, f_i are the reference PDF associated with the flavor of the i-th parton, and f_i' are the corresponding new PDF sets. The reference PDF set, central values of MSTW2008lo68, is tested against the variations on MSTW2008lo69 error sets, and other two common PDF sets: CTEQ61 and CTEQ66. The signal acceptance is then calculated using reweighted events. The effects of PDF uncertainty are less than 2%

in various models, as shown in Fig. 4.16.

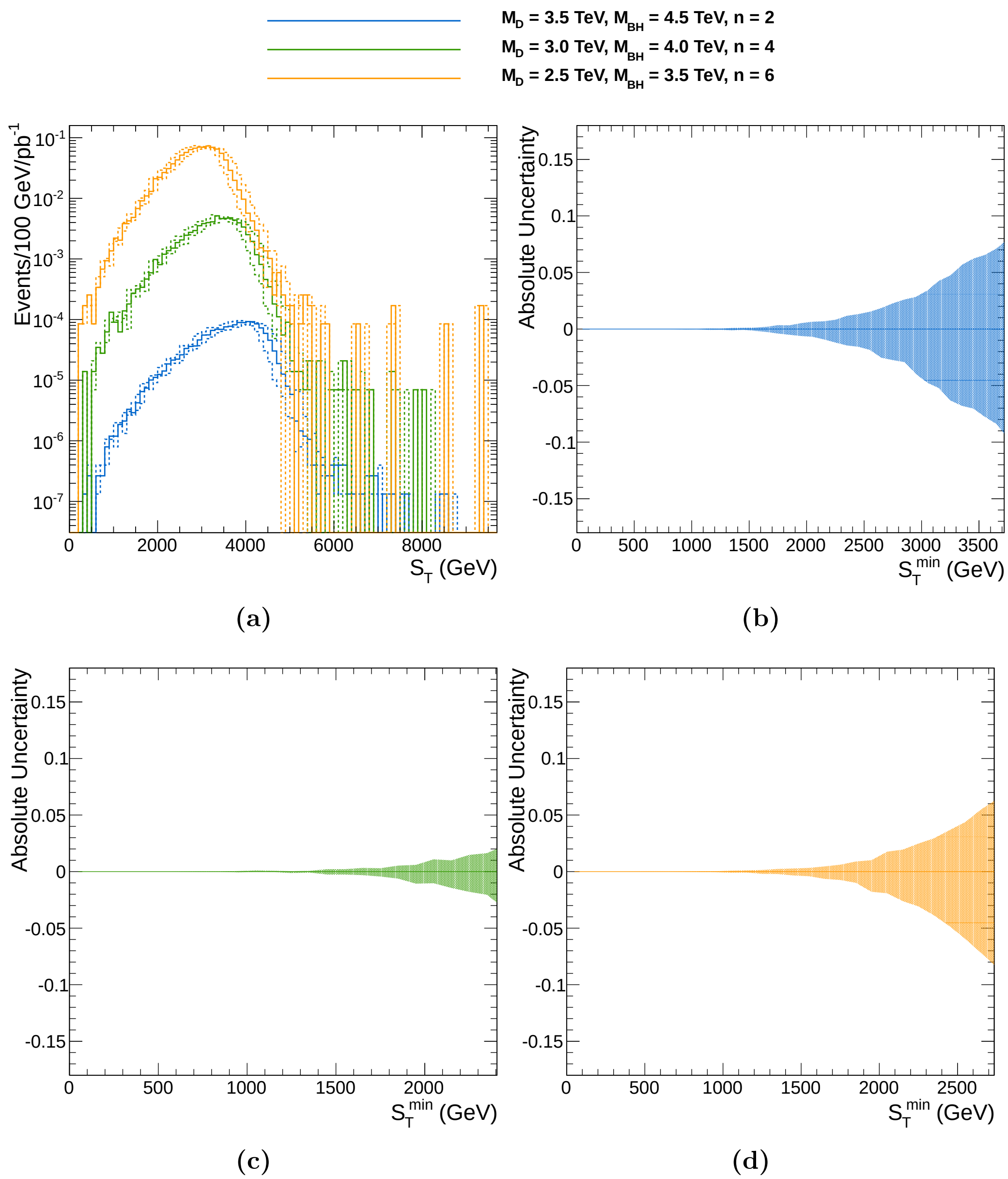

Figure 4.14: Effect of ±5% jet-energy-scale uncertainty on: (a) S_{T} distribution; (b)(c)(d) signal acceptance as function of $S_{\mathrm{T}}^{\mathrm{min}}$.

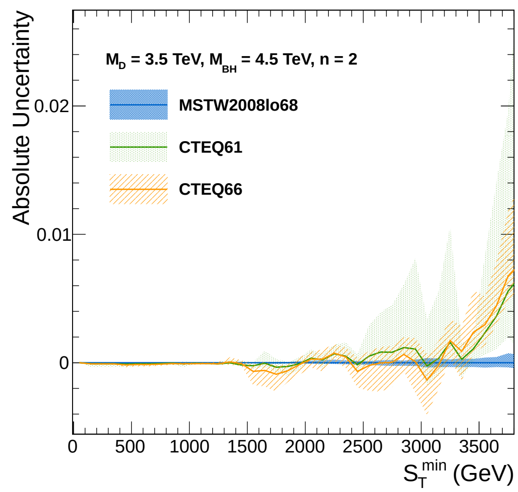

(a)

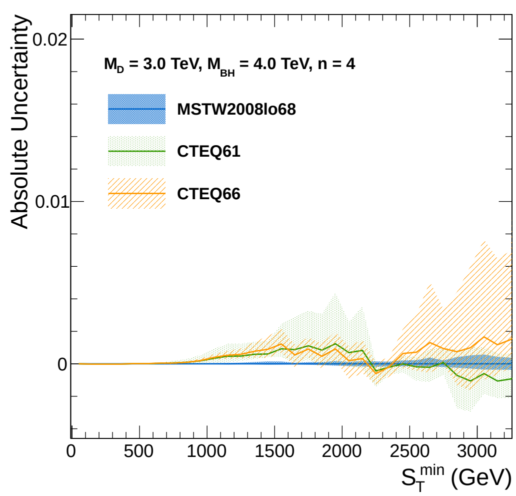

(b)

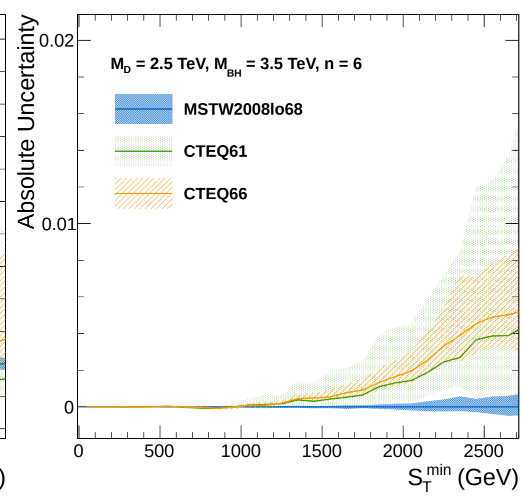

(c)

Figure 4.15

Figure 4.16: Effect of parton distribution function uncertainty on signal acceptance. The solid lines are variations with respect to the central values of three PDF sets: MSTW2008lo68, CTEQ61, and CTEQ66. Shaded regions represent the variations of PDF error sets.

4.5 Results

Figure 4.17 shows the S_T distribution for exclusive multiplicity $N = 2$ and $N = 3$. The background templates for these two multiplicities agree with each other within uncertainties, demonstrating the S_T shape invariant of the final-state multiplicity. The contribution of standard model backgrounds, other than multi-jet process, are negligibly small (less than 1%), as shown by colored histograms in Fig. 4.17. There is no signal contamination in the fitting and normalization region. Figure 4.18 demonstrates the S_T shape is indeed independent of the event multiplicity up to five objects final-state. No excess signal is observed above the predicted background.

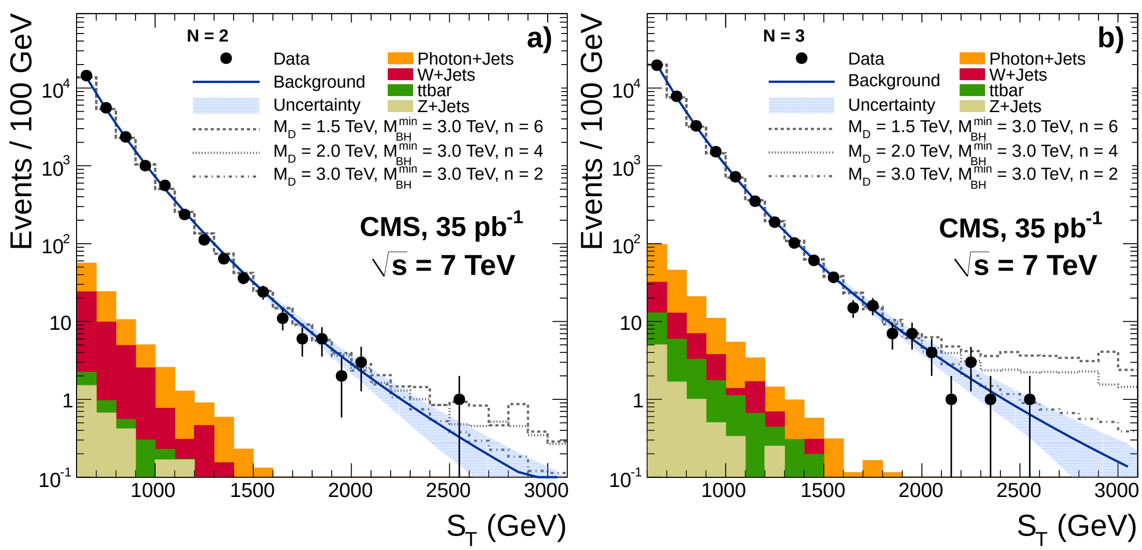

(a) $N = 2$

(b) $N = 3$

Figure 4.17: Total transverse energy S_T for exclusive event multiplicity $N = 2$ and $N = 3$.

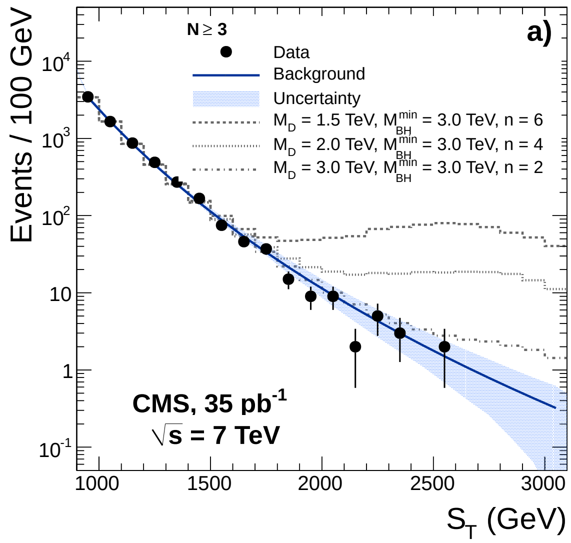

(a) $N \geq 3$

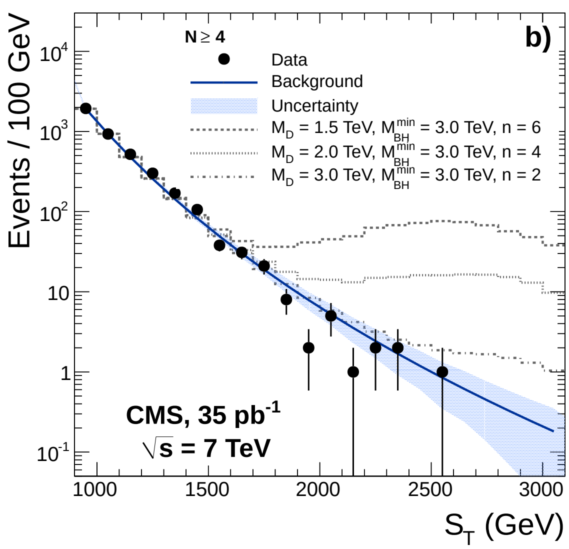

(b) $N \geq 4$

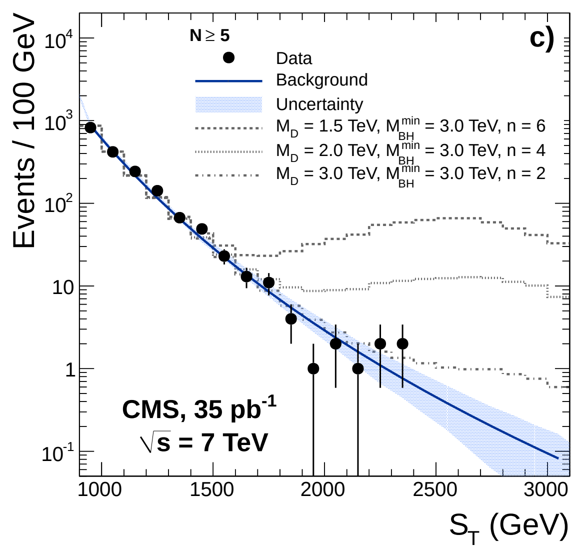

(c) $N \geq 5$

Figure 4.18: Total transverse energy S_T for inclusive event multiplicity $N \geq 3$, $N \geq 4$, and $N \geq 5$

.

4.5.1 Limits on the Minimum Black Hole Mass

The upper limit on the black hole production cross section is calculated by Bayesian method. The likelihood function of Poisson model is defined as

$$L(n|\sigma, \mathcal{L}, A, b) = \frac{(\sigma A\mathcal{L} + b)^n}{n!} e^{-(\sigma A\mathcal{L}+b)},$$

where n is the number of observed events, σ is the cross section of black hole, $\mathcal{L}$ is the measured integrated luminosity, A is the signal acceptance, and b is the number of expected backgrounds. The posterior probability, as a function of signal cross section σ, is the integral of all nuisance parameters $\boldsymbol{\lambda} = (A, \mathcal{L}, b)$ with a flat prior $\pi(\sigma)$ on signal cross section:

$$p(\sigma|n, \boldsymbol{\lambda}) = \frac{L(n|\sigma, \boldsymbol{\lambda})\pi(\boldsymbol{\lambda}|\sigma)\pi(\sigma)}{\int_0^\infty \int_0^\infty L(n|\sigma, \boldsymbol{\lambda})\pi(\boldsymbol{\lambda}|\sigma)\pi(\sigma) d\sigma d\boldsymbol{\lambda}}.$$

The prior for nuisance parameters is a product of log-normal distributions with estimated means $(\bar{A}, \bar{\mathcal{L}}, \bar{b})$ and the corresponding variances $(\sigma_A^2, \sigma_{\mathcal{L}}^2, \sigma_b^2)$:

$$\pi(\boldsymbol{\lambda}|\sigma) = \prod_{\lambda \in \{A, \mathcal{L}, b\}} \frac{1}{\lambda \sigma_\lambda \sqrt{2\pi}} e^{-\frac{\ln(\lambda - \bar{\lambda})^2}{2\sigma_\lambda^2}}.$$

The mean and variance of the number of expected backgrounds and signal acceptances are estimated as discussed in the last section. The uncertainty of integrated luminosity is 11% [109]. The particle identification efficiency does not affect the signal acceptance, since an unidentified electron would fall into a jet or photon category; an unidentified photon would be classified as a jet; a rejected muon would finally contribute to $\not{E}_T$. Therefore, the total sum of transverse energy S_{T} is virtually not affected. In addition, the trigger efficiency does not affect the signal acceptance as well, since for all black hole signals S_{T} ¿ 1 TeV or higher requirement is used, where

H_T trigger is fully efficient. Table 4.4 summarizes all systematic uncertainties on nuisance parameters.

Nuisance Parameter	Source of Uncertainty	Effect	Nominal Value
Signal Acceptance (A)	Jet Energy Scale	5%	5 %
	PDF	2%	
Integrated Luminosity ($\mathcal{L}$)	Luminosity Measurement	11%	11%
Background (b)	Shape Modeling	6 - 125%	7.2 - 125.6%
	Normalization	4 - 12%	

Table 4.4: Summary of systematic uncertainty on nuisance parameters.

For any given number of observed events n, the upper limit of black hole cross section $\sigma_{95}(n)$ at 95% confidence level (C.L.) is calculated from

$$\int_0^{\sigma^{95}(n)} p(\sigma|n, \boldsymbol{\lambda}) d\sigma = 0.95,$$

and the corresponding expected limit with zero signal is

$$\sigma^{95}_{\text{exp.}} = \sum_{n=0}^{\infty} \sigma^{95}(n) \times \frac{\bar{b}^n}{n!} e^{-\bar{b}},$$

where $\bar{b} = n^{\text{bkg.}}$ is the expected number of backgrounds obtained from data-driven method. The observed limit of black hole cross section with number of selected event from data n^{data} at 95% C.L. is $\sigma^{95}(n^{\text{data}})$. The upper limit, together with theoretical cross section, are plotted as a function of the minimum black hole mass ($M_{\text{BH}}^{\text{min}}$) (Fig. 4.19). The intersection of cross section curves with upper limit at 95% C.L. and theoretical predictions represents the upper limit on minimum black hole mass at 95% C.L. Any model with the minimum black hole mass less than the upper limit is excluded. The limit calculations are repeated for several benchmark scenarios of black hole production, as shown in Tables 4.5 - 4.7 and Figures 4.20 - 4.22. All the results are summarized in Figure 4.23, where the 95% confidence level limits on the minimum black hole mass $M_{\text{BH}}^{\text{min}}$ as a function of extra dimensional Planck scale

M_D. The area below each curve is excluded by this search. The limits on minimum black hole mass are in the range of 3.5 - 4.5 TeV. There is no major difference for the excluded region of non-rotating, rotating, and stable remnant scenarios, which also demonstrate the robustness of S_T variable in multiple final-state searches.

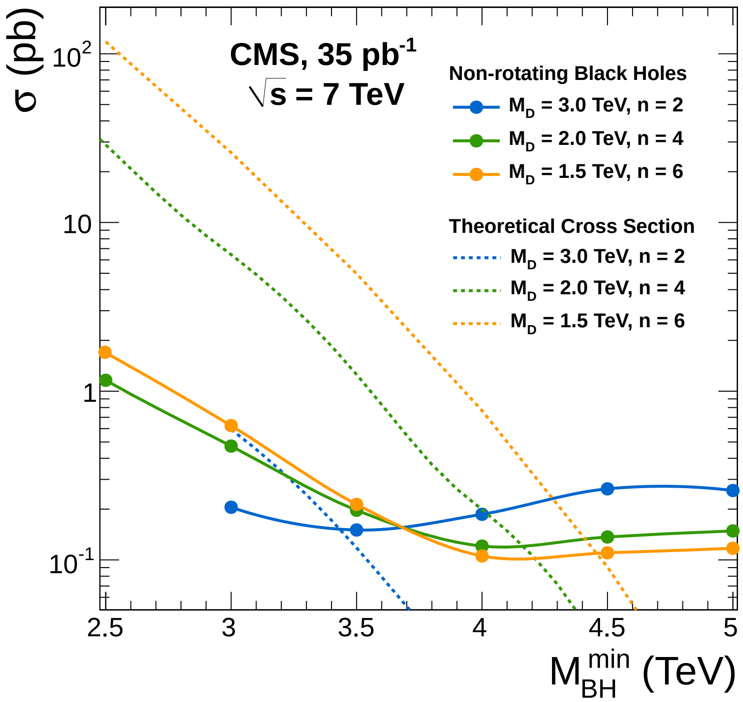

Figure 4.19: The upper limit on the black hole production cross section at 95% confidence level, and theoretical predictions, as a function of minimum black hole mass.

Table 4.5: Simulated non-rotating black hole of model parameters, corresponding cross section (σ), the optimal minimum cut for event multiplicity ($N \geq N^{\mathrm{min}}$) and S_{T} ($S_{\mathrm{T}} > S_{\mathrm{T}}^{\mathrm{min}}$), the signal acceptance (A), the expected number of signal events (n^{sig}), the number of observed events (n^{data}) in data, the expected number of background events (n^{bkg}), and the observed (σ^{95}) and expected ($\sigma^{95}_{\mathrm{exp.}}$) limits on the signal cross section at 95% confidence level.

M_{D} (TeV)	$M_{\mathrm{BH}}^{\mathrm{min}}$ (TeV)	n	σ (pb)	N^{min}	$S_{\mathrm{T}}^{\mathrm{min}}$ (TeV)	A	n^{sig}	n^{data}	n^{bkg}	σ^{95} (pb)	$\sigma^{95}_{\mathrm{exp.}}$ (pb)
1.5	2.0	2	63.73	3	1.4	81.3	1800.47	370	387.32 ± 57.21	3.25	3.69
1.5	2.5	2	16.32	3	1.7	83.7	474.54	82	99.66 ± 28.07	1.12	1.60
1.5	3.0	2	3.77	4	2.0	80.1	105.00	11	17.32 ± 7.89	0.32	0.52
1.5	3.5	2	0.75	5	2.3	74.1	19.26	2	2.77 ± 1.84	0.19	0.23
1.5	4.0	2	0.12	5	2.7	74.5	3.17	0	0.81 ± 0.80	0.12	0.16
1.5	4.5	2	0.02	5	3.2	68.7	0.36	0	$0.21^{+0.31}_{-0.21}$	0.13	0.14
1.5	5.0	2	0.00	5	3.7	60.7	0.03	0	$0.06^{+0.12}_{-0.06}$	0.15	0.15
2.0	2.0	2	29.59	3	1.5	74.7	767.98	203	240.51 ± 45.12	2.05	3.06
2.0	2.5	2	7.58	3	1.8	75.9	199.81	45	66.17 ± 22.18	0.75	1.36
2.0	3.0	2	1.75	3	2.2	73.6	44.80	10	15.18 ± 8.93	0.37	0.56
2.0	3.5	2	0.35	4	2.5	69.2	8.35	1	3.25 ± 2.65	0.16	0.27
2.0	4.0	2	0.06	5	2.9	58.1	1.15	0	$0.46^{+0.54}_{-0.46}$	0.15	0.19

Continued on Next Page

Table 4.5 Non-rotating Black Hole – Continued

M_{D} (TeV)	$M_{\mathrm{BH}}^{\min}$ (TeV)	n	σ (pb)	$N^{\min}$	$S_{\mathrm{T}}^{\min}$ (TeV)	A	n^{sig}	n^{data}	n^{bkg}	σ^{95} (pb)	$\sigma_{\mathrm{exp.}}^{95}$ (pb)
2.0	4.5	2	0.01	5	3.3	57.2	0.14	0	$0.16^{+0.25}_{-0.16}$	0.15	0.17
2.0	5.0	2	0.00	5	3.8	52.1	0.01	0	$0.05^{+0.10}_{-0.05}$	0.17	0.18
2.5	2.5	2	4.18	3	1.9	70.7	102.56	30	44.74 ± 17.57	0.66	1.14
2.5	3.0	2	0.97	3	2.3	67.0	22.49	5	10.87 ± 7.18	0.27	0.51
2.5	3.5	2	0.19	4	2.6	59.8	3.98	0	2.40 ± 2.16	0.15	0.27
2.5	4.0	2	0.03	4	3.1	55.5	0.61	0	$0.60^{+0.81}_{-0.60}$	0.16	0.20
2.5	4.5	2	0.00	5	3.5	43.0	0.06	0	$0.10^{+0.18}_{-0.10}$	0.21	0.22
2.5	5.0	2	0.00	5	3.9	43.6	0.00	0	$0.04^{+0.08}_{-0.04}$	0.20	0.21
3.0	3.0	2	0.59	3	2.4	62.1	12.82	2	7.88 ± 5.80	0.21	0.46
3.0	3.5	2	0.12	3	2.8	58.9	2.41	0	$2.40^{+2.57}_{-2.40}$	0.15	0.28
3.0	4.0	2	0.02	4	3.2	47.3	0.32	0	$0.46^{+0.67}_{-0.46}$	0.19	0.23
3.0	4.5	2	0.00	5	3.6	33.6	0.03	0	$0.08^{+0.15}_{-0.08}$	0.26	0.28
3.0	5.0	2	0.00	5	4.0	34.5	0.00	0	$0.03^{+0.07}_{-0.03}$	0.26	0.26
3.5	3.5	2	0.08	3	2.9	53.6	1.45	0	$1.82^{+2.11}_{-1.82}$	0.17	0.28

Continued on Next Page

Table 4.5 Non-rotating Black Hole – Continued

M_{D} (TeV)	$M_{\mathrm{BH}}^{\mathrm{min}}$ (TeV)	n	σ (pb)	N^{min}	$S_{\mathrm{T}}^{\mathrm{min}}$ (TeV)	A	n^{sig}	n^{data}	n^{bkg}	σ^{95} (pb)	$\sigma^{95}_{\mathrm{exp.}}$ (pb)
3.5	4.0	2	0.01	4	3.3	41.2	0.18	0	$0.36^{+0.56}_{-0.36}$	0.21	0.25
3.5	4.5	2	0.00	4	3.7	40.0	0.02	0	$0.14^{+0.27}_{-0.14}$	0.22	0.24
3.5	5.0	2	0.00	5	4.1	27.0	0.00	0	$0.02^{+0.06}_{-0.02}$	0.33	0.33
1.5	2.0	4	240.50	3	1.3	86.4	7217.47	642	641.51 ± 72.68	4.61	4.56
1.5	2.5	4	57.60	3	1.6	87.1	1743.72	128	153.10 ± 35.58	1.39	2.00
1.5	3.0	4	12.87	4	1.8	87.7	391.96	21	37.28 ± 12.56	0.35	0.75
1.5	3.5	4	2.51	4	2.2	86.6	75.39	5	8.55 ± 5.04	0.22	0.33
1.5	4.0	4	0.40	5	2.5	83.1	11.44	0	1.47 ± 1.20	0.11	0.17
1.5	4.5	4	0.05	5	3.0	78.1	1.28	0	$0.35^{+0.44}_{-0.35}$	0.11	0.13
1.5	5.0	4	0.00	5	3.6	65.4	0.08	0	$0.08^{+0.15}_{-0.08}$	0.14	0.14
2.0	2.0	4	120.60	3	1.4	79.4	3327.39	370	387.32 ± 57.21	3.31	3.78
2.0	2.5	4	28.88	3	1.7	81.4	816.93	82	99.66 ± 28.07	1.16	1.64
2.0	3.0	4	6.45	3	2.0	83.2	186.49	21	30.75 ± 13.97	0.47	0.76
2.0	3.5	4	1.26	4	2.3	77.9	34.00	3	6.12 ± 4.05	0.20	0.31

Continued on Next Page

Table 4.5 Non-rotating Black Hole – Continued

M_{D} (TeV)	$M_{\mathrm{BH}}^{\mathrm{min}}$ (TeV)	n	σ (pb)	N^{min}	$S_{\mathrm{T}}^{\mathrm{min}}$ (TeV)	A	n^{sig}	n^{data}	n^{bkg}	σ^{95} (pb)	$\sigma^{95}_{\mathrm{exp.}}$ (pb)
2.0	4.0	4	0.20	4	2.8	73.4	5.07	0	$1.35^{+1.45}_{-1.35}$	0.12	0.19
2.0	4.5	4	0.02	5	3.2	64.4	0.53	0	$0.21^{+0.31}_{-0.21}$	0.14	0.15
2.0	5.0	4	0.00	5	3.7	59.6	0.04	0	$0.06^{+0.12}_{-0.06}$	0.15	0.15
2.5	2.5	4	16.90	3	1.8	75.6	443.67	45	66.17 ± 22.18	0.75	1.36
2.5	3.0	4	3.78	3	2.1	77.7	101.98	12	21.46 ± 11.15	0.35	0.65
2.5	3.5	4	0.74	3	2.5	74.9	19.13	2	5.77 ± 4.71	0.18	0.32
2.5	4.0	4	0.12	4	2.9	64.0	2.58	0	$1.02^{+1.19}_{-1.02}$	0.14	0.20
2.5	4.5	4	0.01	5	3.3	52.8	0.25	0	$0.16^{+0.25}_{-0.16}$	0.17	0.18
2.5	5.0	4	0.00	5	3.9	44.5	0.02	0	$0.04^{+0.08}_{-0.04}$	0.20	0.20
3.0	3.0	4	2.44	3	2.2	72.4	61.26	10	15.18 ± 8.93	0.38	0.57
3.0	3.5	4	0.47	3	2.6	69.1	11.39	0	4.27 ± 3.83	0.13	0.30
3.0	4.0	4	0.08	4	3.0	56.5	1.47	0	$0.78^{+0.98}_{-0.78}$	0.16	0.21
3.0	4.5	4	0.01	4	3.5	51.6	0.16	0	$0.22^{+0.39}_{-0.22}$	0.17	0.19
3.0	5.0	4	0.00	5	3.9	39.2	0.01	0	$0.04^{+0.08}_{-0.04}$	0.23	0.23

Continued on Next Page

Table 4.5 Non-rotating Black Hole – Continued

M_{D} (TeV)	$M_{\mathrm{BH}}^{\mathrm{min}}$ (TeV)	n	σ (pb)	N^{min}	$S_{\mathrm{T}}^{\mathrm{min}}$ (TeV)	A	n^{sig}	n^{data}	n^{bkg}	σ^{95} (pb)	$\sigma_{\mathrm{exp.}}^{95}$ (pb)
3.5	3.5	4	0.33	3	2.7	64.1	7.30	0	3.18 ± 3.13	0.14	0.29
3.5	4.0	4	0.05	3	3.1	61.2	1.10	0	$1.07^{+1.44}_{-1.07}$	0.14	0.21
3.5	4.5	4	0.01	4	3.6	44.9	0.10	0	$0.17^{+0.32}_{-0.17}$	0.20	0.22
3.5	5.0	4	0.00	5	4.0	31.7	0.01	0	$0.03^{+0.07}_{-0.03}$	0.28	0.28
1.5	2.5	6	117.90	3	1.5	90.6	3712.86	203	240.51 ± 45.12	1.69	2.52
1.5	3.0	6	25.94	3	1.8	91.3	822.65	45	66.17 ± 22.18	0.62	1.13
1.5	3.5	6	4.97	4	2.1	88.3	152.63	6	12.09 ± 6.29	0.21	0.39
1.5	4.0	6	0.77	5	2.4	84.4	22.50	0	2.01 ± 1.48	0.11	0.18
1.5	4.5	6	0.09	5	2.9	80.9	2.55	0	$0.46^{+0.54}_{-0.46}$	0.11	0.13
1.5	5.0	6	0.01	5	3.4	75.2	0.19	0	$0.13^{+0.21}_{-0.13}$	0.12	0.13
2.0	2.0	6	260.50	3	1.3	83.0	7512.33	642	641.51 ± 72.68	4.77	4.74
2.0	2.5	6	61.07	3	1.6	85.8	1819.42	128	153.10 ± 35.58	1.41	2.04
2.0	3.0	6	13.44	3	1.9	85.8	400.79	30	44.74 ± 17.57	0.54	0.94
2.0	3.5	6	2.58	3	2.3	83.5	74.79	5	10.87 ± 7.18	0.22	0.40

Continued on Next Page

Table 4.5 Non-rotating Black Hole – Continued

$M_{\rm D}$ (TeV)	$M_{\rm BH}^{\rm min}$ (TeV)	n	σ (pb)	$N^{\rm min}$	$S_{\rm T}^{\rm min}$ (TeV)	A	$n^{\rm sig}$	$n^{\rm data}$	$n^{\rm bkg}$	σ^{95} (pb)	$\sigma_{\rm exp.}^{95}$ (pb)
2.0	4.0	6	0.40	4	2.6	80.2	11.08	0	2.40 ± 2.16	0.11	0.20
2.0	4.5	6	0.05	5	3.0	71.0	1.16	0	$0.35^{+0.44}_{-0.35}$	0.12	0.15
2.0	5.0	6	0.00	5	3.6	63.1	0.08	0	$0.08^{+0.15}_{-0.08}$	0.14	0.15
2.5	2.5	6	36.67	3	1.6	83.2	1060.57	128	153.10 ± 35.58	1.45	2.10
2.5	3.0	6	8.07	3	2.0	81.1	227.31	21	30.75 ± 13.97	0.48	0.78
2.5	3.5	6	1.55	3	2.4	78.8	42.38	2	7.88 ± 5.80	0.16	0.36
2.5	4.0	6	0.24	4	2.7	72.5	6.01	0	1.79 ± 1.77	0.12	0.20
2.5	4.5	6	0.03	5	3.2	57.1	0.56	0	$0.21^{+0.31}_{-0.21}$	0.15	0.17
2.5	5.0	6	0.00	5	3.8	49.0	0.04	0	$0.05^{+0.10}_{-0.05}$	0.18	0.19
3.0	3.0	6	5.32	3	2.0	79.2	146.40	21	30.75 ± 13.97	0.50	0.80
3.0	3.5	6	1.02	3	2.4	76.3	27.05	2	7.88 ± 5.80	0.17	0.37
3.0	4.0	6	0.16	3	2.9	70.7	3.86	0	$1.82^{+2.11}_{-1.82}$	0.13	0.21
3.0	4.5	6	0.02	4	3.4	56.7	0.37	0	$0.28^{+0.47}_{-0.28}$	0.16	0.18
3.0	5.0	6	0.00	5	3.9	40.6	0.02	0	$0.04^{+0.08}_{-0.04}$	0.22	0.22

Continued on Next Page

Table 4.5 Non-rotating Black Hole – Continued

M_{D} (TeV)	$M_{\mathrm{BH}}^{\mathrm{min}}$ (TeV)	n	σ (pb)	N^{min}	$S_{\mathrm{T}}^{\mathrm{min}}$ (TeV)	A	n^{sig}	n^{data}	n^{bkg}	σ^{95} (pb)	$\sigma_{\mathrm{exp.}}^{95}$ (pb)
3.5	3.5	6	0.72	3	2.5	72.5	18.07	2	5.77 ± 4.71	0.18	0.33
3.5	4.0	6	0.11	3	3.0	65.7	2.53	0	$1.39^{+1.75}_{-1.39}$	0.13	0.21
3.5	4.5	6	0.01	4	3.5	49.4	0.22	0	$0.22^{+0.39}_{-0.22}$	0.18	0.20
3.5	5.0	6	0.00	5	3.9	35.8	0.01	0	$0.04^{+0.08}_{-0.04}$	0.25	0.25

Table 4.6: Simulated rotating black hole of model parameters, corresponding cross section (σ), the optimal minimum cut for event multiplicity ($N \geq N^{\mathrm{min}}$) and S_{T} ($S_{\mathrm{T}} > S_{\mathrm{T}}^{\mathrm{min}}$), the signal acceptance (A), the expected number of signal events (n^{sig}), the number of observed events (n^{data}) in data, the expected number of background events (n^{bkg}), and the observed (σ^{95}) and expected ($\sigma^{95}_{\mathrm{exp.}}$) limits on the signal cross section at 95% confidence level.

M_{D} (TeV)	$M_{\mathrm{BH}}^{\mathrm{min}}$ (TeV)	n	σ (pb)	N^{min}	$S_{\mathrm{T}}^{\mathrm{min}}$ (TeV)	A	n^{sig}	n^{data}	n^{bkg}	σ^{95} (pb)	$\sigma^{95}_{\mathrm{exp.}}$ (pb)
1.5	3.5	2	0.75	3	2.5	72.5	18.86	2	5.77 ± 4.71	0.18	0.33
1.5	4.0	2	0.12	4	2.9	65.4	2.79	0	$1.02^{+1.19}_{-1.02}$	0.14	0.19
1.5	4.5	2	0.02	5	3.3	50.1	0.26	0	$0.16^{+0.25}_{-0.16}$	0.18	0.19
2.0	3.5	2	0.35	3	2.6	66.5	8.03	0	4.27 ± 3.83	0.13	0.32
2.0	4.0	2	0.06	4	3.0	53.1	1.05	0	$0.78^{+0.98}_{-0.78}$	0.17	0.22
2.0	4.5	2	0.01	5	3.4	43.6	0.11	0	$0.13^{+0.21}_{-0.13}$	0.20	0.22
2.5	3.0	2	0.97	3	2.4	53.5	17.98	2	7.88 ± 5.80	0.24	0.53
2.5	3.5	2	0.19	3	2.8	57.1	3.81	0	$2.40^{+2.57}_{-2.40}$	0.16	0.29
2.5	4.0	2	0.03	4	3.1	51.1	0.56	0	$0.60^{+0.81}_{-0.60}$	0.17	0.22
2.5	4.5	2	0.00	4	3.6	40.9	0.06	0	$0.17^{+0.32}_{-0.17}$	0.22	0.24
3.0	3.0	2	0.59	3	2.4	57.4	11.85	2	7.88 ± 5.80	0.22	0.49
3.0	3.5	2	0.12	3	2.9	47.0	1.92	0	$1.82^{+2.11}_{-1.82}$	0.19	0.32

Continued on Next Page

Table 4.6 Rotating Black Hole – Continued

M_{D} (TeV)	$M_{\mathrm{BH}}^{\mathrm{min}}$ (TeV)	n	σ (pb)	N^{min}	$S_{\mathrm{T}}^{\mathrm{min}}$ (TeV)	A	n^{sig}	n^{data}	n^{bkg}	σ^{95} (pb)	$\sigma^{95}_{\mathrm{exp.}}$ (pb)
3.0	4.0	2	0.02	3	3.4	42.5	0.29	0	$0.50^{+0.83}_{-0.50}$	0.21	0.26
3.0	4.5	2	0.00	4	3.7	40.1	0.03	0	$0.14^{+0.27}_{-0.14}$	0.22	0.24
3.5	3.5	2	0.08	3	2.9	52.5	1.43	0	$1.82^{+2.11}_{-1.82}$	0.17	0.29
3.5	4.0	2	0.01	3	3.4	41.6	0.18	0	$0.50^{+0.83}_{-0.50}$	0.21	0.26
3.5	4.5	2	0.00	3	3.9	34.7	0.02	0	$0.15^{+0.33}_{-0.15}$	0.25	0.27
1.5	3.5	4	2.51	3	2.3	83.6	72.74	5	10.87 ± 7.18	0.22	0.40
1.5	4.0	4	0.40	4	2.7	75.0	10.33	0	1.79 ± 1.77	0.12	0.20
1.5	4.5	4	0.05	5	3.1	63.1	1.03	0	$0.27^{+0.37}_{-0.27}$	0.14	0.16
1.5	5.0	4	0.00	5	3.7	54.2	0.07	0	$0.06^{+0.12}_{-0.06}$	0.16	0.17
2.0	3.5	4	1.26	3	2.4	77.2	33.69	2	7.88 ± 5.80	0.16	0.37
2.0	4.0	4	0.20	4	2.8	67.7	4.67	0	$1.35^{+1.45}_{-1.35}$	0.13	0.20
2.0	4.5	4	0.02	5	3.2	53.8	0.44	0	$0.21^{+0.31}_{-0.21}$	0.17	0.18
2.5	3.5	4	0.74	3	2.5	71.1	18.16	2	5.77 ± 4.71	0.19	0.34
2.5	4.0	4	0.12	4	2.9	61.8	2.50	0	$1.02^{+1.19}_{-1.02}$	0.14	0.20

Continued on Next Page

Table 4.6 Rotating Black Hole – Continued

M_{D} (TeV)	$M_{\mathrm{BH}}^{\mathrm{min}}$ (TeV)	n	σ (pb)	N^{min}	$S_{\mathrm{T}}^{\mathrm{min}}$ (TeV)	A	n^{sig}	n^{data}	n^{bkg}	σ^{95} (pb)	$\sigma^{95}_{\mathrm{exp.}}$ (pb)
2.5	4.5	4	0.01	4	3.4	53.9	0.26	0	$0.28^{+0.47}_{-0.28}$	0.16	0.19
3.0	3.5	4	0.47	3	2.6	64.8	10.69	0	4.27 ± 3.83	0.14	0.32
3.0	4.0	4	0.08	3	3.1	60.2	1.57	0	$1.07^{+1.44}_{-1.07}$	0.15	0.21
3.0	4.5	4	0.01	4	3.5	46.3	0.14	0	$0.22^{+0.39}_{-0.22}$	0.19	0.21
3.5	3.5	4	0.33	3	2.7	62.3	7.09	0	3.18 ± 3.13	0.14	0.30
3.5	4.0	4	0.05	3	3.2	53.2	0.96	0	$0.82^{+1.20}_{-0.82}$	0.17	0.23
3.5	4.5	4	0.01	4	3.6	44.9	0.10	0	$0.17^{+0.32}_{-0.17}$	0.20	0.22
1.5	3.5	6	4.97	3	2.2	86.7	149.82	10	15.18 ± 8.93	0.31	0.47
1.5	4.0	6	0.77	3	2.6	85.0	22.64	0	4.27 ± 3.83	0.10	0.25
1.5	4.5	6	0.09	4	3.1	74.0	2.33	0	$0.60^{+0.81}_{-0.60}$	0.12	0.15
1.5	5.0	6	0.01	5	3.6	59.1	0.15	0	$0.08^{+0.15}_{-0.08}$	0.15	0.16
2.0	3.5	6	2.58	3	2.3	82.6	73.92	5	10.87 ± 7.18	0.22	0.41
2.0	4.0	6	0.40	3	2.8	76.2	10.52	0	$2.40^{+2.57}_{-2.40}$	0.12	0.22
2.0	4.5	6	0.05	4	3.2	67.4	1.10	0	$0.46^{+0.67}_{-0.46}$	0.13	0.16

Continued on Next Page

Table 4.6 Rotating Black Hole – Continued

M_{D} (TeV)	$M_{\mathrm{BH}}^{\mathrm{min}}$ (TeV)	n	σ (pb)	N^{min}	$S_{\mathrm{T}}^{\mathrm{min}}$ (TeV)	A	n^{sig}	n^{data}	n^{bkg}	σ^{95} (pb)	$\sigma_{\mathrm{exp.}}^{95}$ (pb)
2.0	5.0	6	0.00	5	3.7	50.8	0.07	0	$0.06^{+0.12}_{-0.06}$	0.17	0.18
2.5	3.5	6	1.55	3	2.4	77.1	41.42	2	7.88 ± 5.80	0.17	0.37
2.5	4.0	6	0.24	3	2.8	73.7	6.11	0	$2.40^{+2.57}_{-2.40}$	0.12	0.22
2.5	4.5	6	0.03	4	3.3	60.8	0.60	0	$0.36^{+0.56}_{-0.36}$	0.14	0.17
3.0	3.5	6	1.02	3	2.5	73.7	26.12	2	5.77 ± 4.71	0.18	0.33
3.0	4.0	6	0.16	3	2.9	68.0	3.71	0	$1.82^{+2.11}_{-1.82}$	0.13	0.22
3.0	4.5	6	0.02	4	3.4	54.9	0.36	0	$0.28^{+0.47}_{-0.28}$	0.16	0.18
3.5	3.5	6	0.72	3	2.5	70.3	17.50	2	5.77 ± 4.71	0.19	0.34
3.5	4.0	6	0.11	3	3.1	60.6	2.33	0	$1.07^{+1.44}_{-1.07}$	0.15	0.21
3.5	4.5	6	0.01	4	3.5	47.2	0.21	0	$0.22^{+0.39}_{-0.22}$	0.19	0.21

Table 4.7: Simulated black hole with stable remnant of model parameters, corresponding cross section (σ), the optimal minimum cut for event multiplicity ($N \geq N^{\mathrm{min}}$) and S_{T} ($S_{\mathrm{T}} > S_{\mathrm{T}}^{\mathrm{min}}$), the signal acceptance (A), the expected number of signal events (n^{sig}), the number of observed events (n^{data}) in data, the expected number of background events (n^{bkg}), and the observed (σ^{95}) and expected ($\sigma^{95}_{\mathrm{exp.}}$) limits on the signal cross section at 95% confidence level.

M_{D} (TeV)	$M_{\mathrm{BH}}^{\mathrm{min}}$ (TeV)	n	σ (pb)	N^{min}	$S_{\mathrm{T}}^{\mathrm{min}}$ (TeV)	A	n^{sig}	n^{data}	n^{bkg}	σ^{95} (pb)	$\sigma^{95}_{\mathrm{exp.}}$ (pb)
1.5	3.5	2.0	1.17	3	2.4	51.8	21.11	2	7.88 ± 5.80	0.25	0.55
1.5	4.0	2.0	0.19	3	2.9	46.2	3.08	0	$1.82^{+2.11}_{-1.82}$	0.19	0.33
1.5	4.5	2.0	0.02	3	3.5	39.5	0.32	0	$0.39^{+0.69}_{-0.39}$	0.22	0.27
2.0	3.5	2.0	0.54	3	2.7	40.4	7.65	0	3.18 ± 3.13	0.22	0.46
2.0	4.0	2.0	0.09	3	3.2	36.6	1.13	0	$0.82^{+1.20}_{-0.82}$	0.24	0.33
2.0	4.5	2.0	0.01	3	3.9	28.4	0.11	0	$0.15^{+0.33}_{-0.15}$	0.31	0.34
2.5	3.5	2.0	0.30	3	2.9	34.8	3.63	0	$1.82^{+2.11}_{-1.82}$	0.25	0.43
2.5	4.0	2.0	0.05	3	3.4	32.7	0.56	0	$0.50^{+0.83}_{-0.50}$	0.27	0.33
2.5	4.5	2.0	0.01	3	4.0	27.0	0.06	0	$0.12^{+0.27}_{-0.12}$	0.33	0.35
1.5	3.5	4.0	4.31	3	2.1	64.5	96.59	12	21.46 ± 11.15	0.42	0.78
1.5	4.0	4.0	0.68	3	2.6	59.1	14.01	0	4.27 ± 3.83	0.15	0.35
1.5	4.5	4.0	0.08	3	3.2	48.9	1.37	0	$0.82^{+1.20}_{-0.82}$	0.18	0.25

Continued on Next Page

Table 4.7 Black Hole with Stable Remnant – Continued

M_{D} (TeV)	$M_{\mathrm{BH}}^{\mathrm{min}}$ (TeV)	n	σ (pb)	N^{min}	$S_{\mathrm{T}}^{\mathrm{min}}$ (TeV)	A	n^{sig}	n^{data}	n^{bkg}	σ^{95} (pb)	$\sigma^{95}_{\mathrm{exp.}}$ (pb)
2.0	3.5	4.0	2.16	3	2.3	52.3	39.29	5	10.87 ± 7.18	0.35	0.65
2.0	4.0	4.0	0.34	3	2.9	44.9	5.33	0	$1.82^{+2.11}_{-1.82}$	0.20	0.34
2.0	4.5	4.0	0.04	3	3.6	36.5	0.51	0	$0.31^{+0.57}_{-0.31}$	0.24	0.28
2.5	3.5	4.0	1.27	3	2.6	41.6	18.31	0	4.27 ± 3.83	0.21	0.50
2.5	4.0	4.0	0.20	3	3.1	39.6	2.76	0	$1.07^{+1.44}_{-1.07}$	0.22	0.32
2.5	4.5	4.0	0.02	3	3.8	31.5	0.26	0	$0.19^{+0.39}_{-0.19}$	0.28	0.31
1.5	3.5	6.0	8.59	3	1.9	74.9	223.34	30	44.74 ± 17.57	0.62	1.07
1.5	4.0	6.0	1.34	3	2.4	69.0	32.15	2	7.88 ± 5.80	0.18	0.41
1.5	4.5	6.0	0.16	4	2.9	56.0	3.06	0	$1.02^{+1.19}_{-1.02}$	0.16	0.23
2.0	3.5	6.0	4.45	3	2.1	60.9	94.05	12	21.46 ± 11.15	0.45	0.83
2.0	4.0	6.0	0.69	3	2.6	57.1	13.79	0	4.27 ± 3.83	0.15	0.37
2.0	4.5	6.0	0.08	3	3.3	46.4	1.31	0	$0.64^{+0.99}_{-0.64}$	0.19	0.25
2.5	3.5	6.0	2.67	3	2.3	50.6	46.96	5	10.87 ± 7.18	0.36	0.67
2.5	4.0	6.0	0.42	3	2.9	45.0	6.52	0	$1.82^{+2.11}_{-1.82}$	0.20	0.33

Continued on Next Page

Table 4.7 Black Hole with Stable Remnant – Continued

M_{D} (TeV)	$M_{\mathrm{BH}}^{\mathrm{min}}$ (TeV)	n	σ (pb)	N^{min}	$S_{\mathrm{T}}^{\mathrm{min}}$ (TeV)	A	n^{sig}	n^{data}	n^{bkg}	σ^{95} (pb)	$\sigma_{\mathrm{exp.}}^{95}$ (pb)
2.5	4.5	6.0	0.05	3	3.6	36.7	0.62	0	$0.31^{+0.57}_{-0.31}$	0.24	0.28

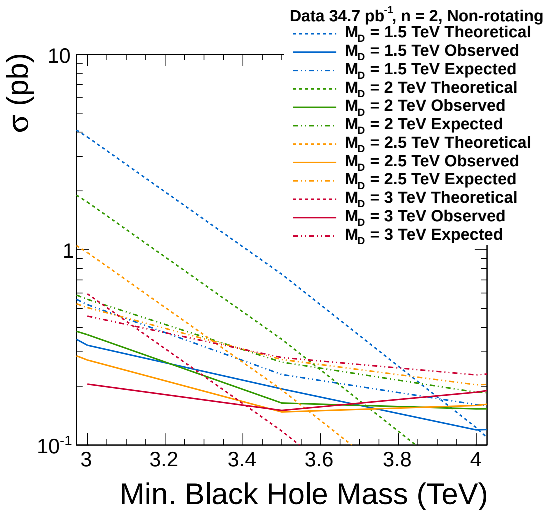

(a) Non-rotating $n = 2$

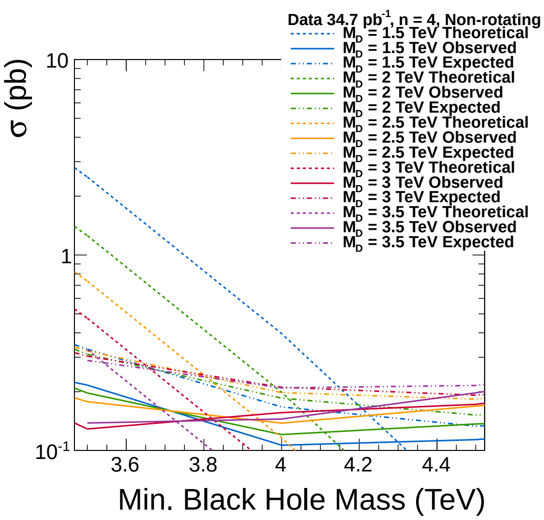

(b) Non-rotating $n = 4$

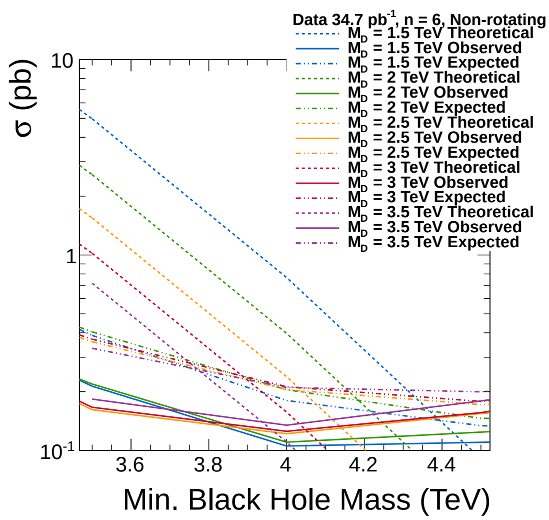

(c) Non-rotating $n = 6$

Figure 4.20: Theoretical, observed and expected limits on cross section of non-rotating black hole production, grouped in number of extra dimensions $n = 2, 4, 6$.

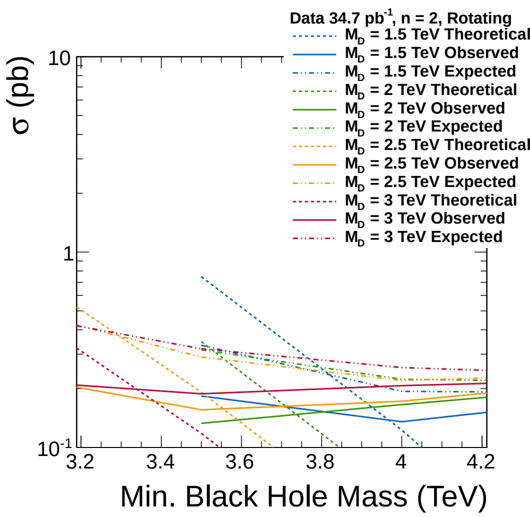

(a) Rotating $n = 2$

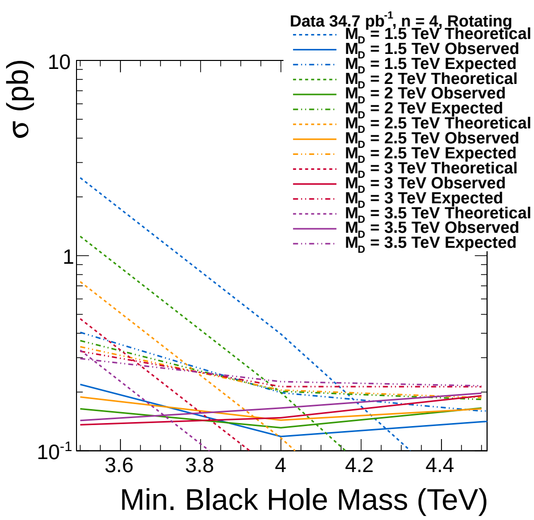

(b) Rotating $n = 4$

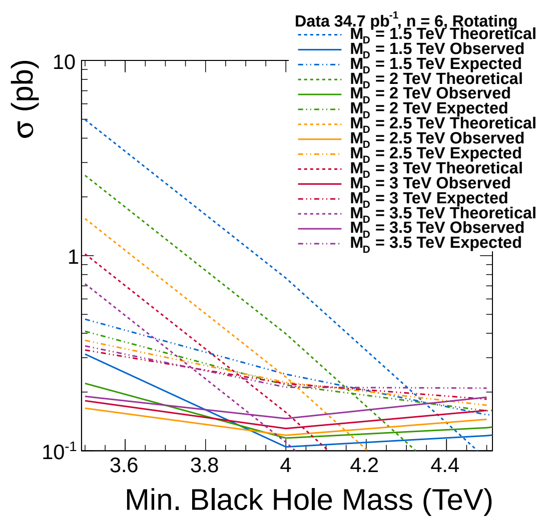

(c) Rotating $n = 6$

Figure 4.21: Theoretical, observed and expected limits on cross section of rotating black hole production, grouped in number of extra dimensions $n = 2, 4, 6$.

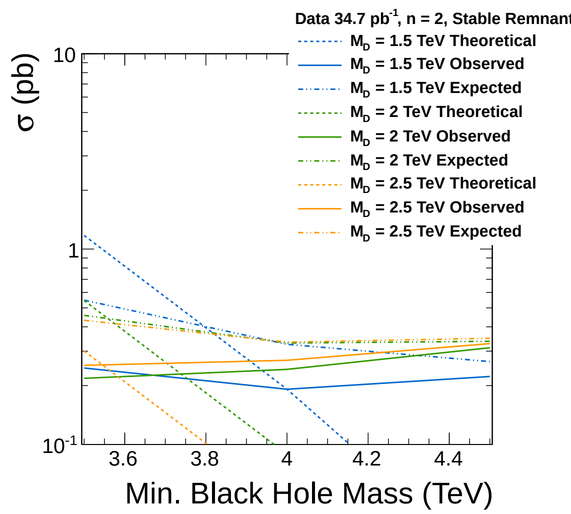

(a) Stable Remnant $n = 2$

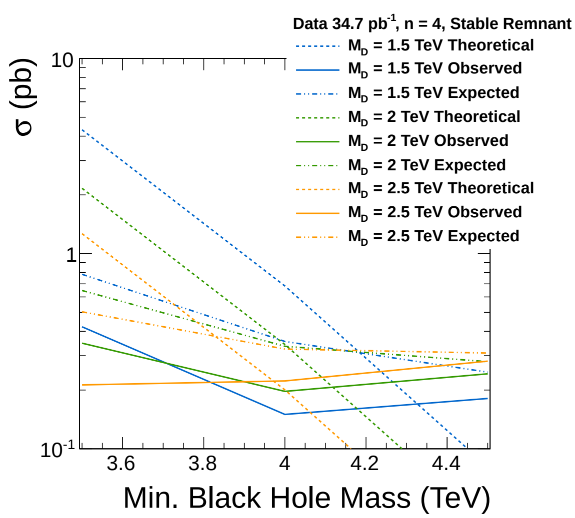

(b) Stable Remnant $n = 4$

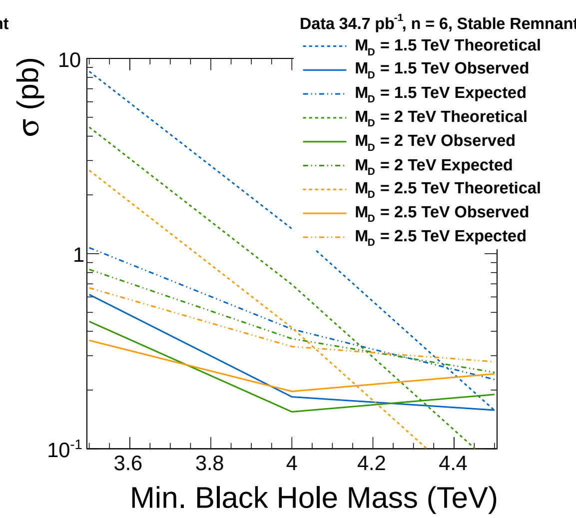

(c) Stable Remnant $n = 6$

Figure 4.22: Theoretical, observed and expected limits on cross section of black hole with stable remnant production, grouped in number of extra dimensions $n = 2, 4, 6$.

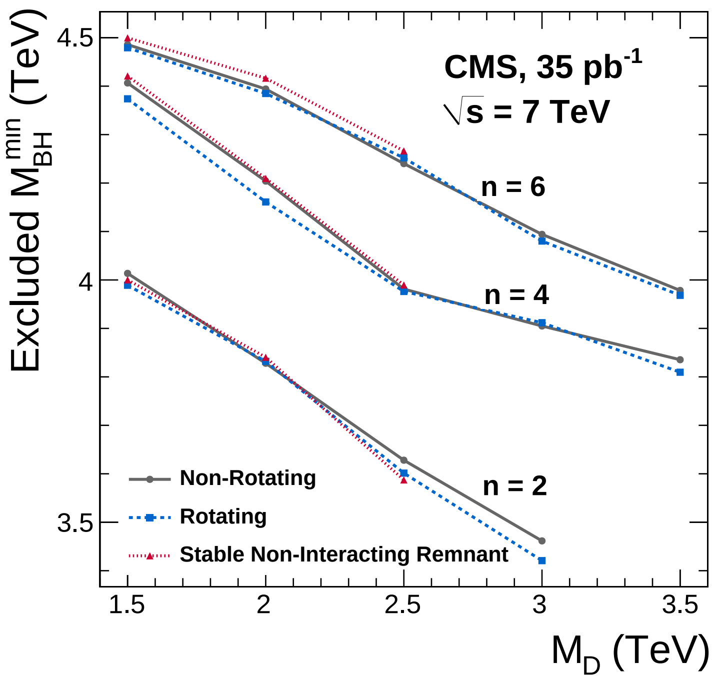

Figure 4.23: The 95% confidence level limits on the minimum black hole mass $M_{\mathrm{BH}}^{\mathrm{min}}$ as a function of extra dimensional Planck scale M_{D} for several benchmark scenarios.

4.5.2 Model-Independent Limits

Because there is large variety of black hole models, it is useful to provide a model-independent limits. The model-independent limits give the upper limits on cross section at 95% C.L. as a function of $S_{\mathrm{T}}^{\mathrm{min}}$ and N^{min}. Assuming signal acceptance of 100% and its nominal uncertainty of 5%, the observed and expected limits are calculated as a function of $S_{\mathrm{T}}^{\mathrm{min}}$ for different inclusive event multiplicities. For a given parameter of a particular signal model, we first calculate the signal acceptance A as a function of the analysis cuts: $S_{\mathrm{T}}^{\mathrm{min}}$ and N^{min}. Then we find the minimum observed (expected) upper limit on cross section provided in Table 4.8. The procedure is repeated for the entire parameter space, and the intersection of the best observed (expected) upper limits and the theoretical cross section is obtained. This process gives the best upper limit, instead of optimizing for a discovery potential. A closure test has been done on a black hole model in the parameter space of the minimum black hole mass. As expected, the upper limit on the minimum black hole mass using model-independent limits (Table 4.8) is a little better than model-dependent search, that is optimized for discovery potential (Fig. 4.25). The overall performance of the model-independent approach is consistent with the dedicated one within a few hundred GeV. The model-independent upper limits table can be used to test any physics, not limited to black hole production, that result in multi-particle final states, such as high-mass $t\bar{t}$ resonances [110] in the six jet and lepton+jet final states; Six-jet signals from R-parity violating gluino decay into three jets [111, 112]; Four-jet final states of pairs of resonances produced from massive color-octet bosons [113], etc. Moreover, these limits can be used to constrain black hole models for additional points in model parameter space.

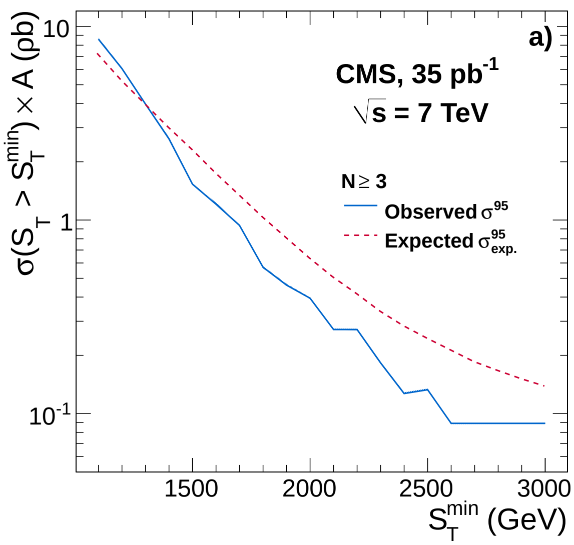

(a) $N \geq 3$

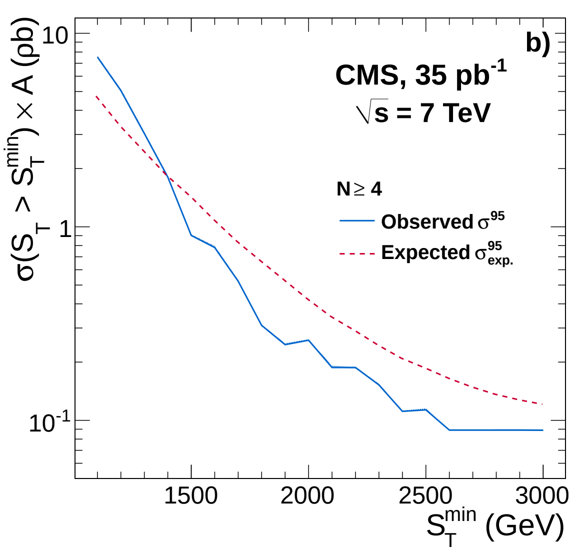

(b) $N \geq 4$

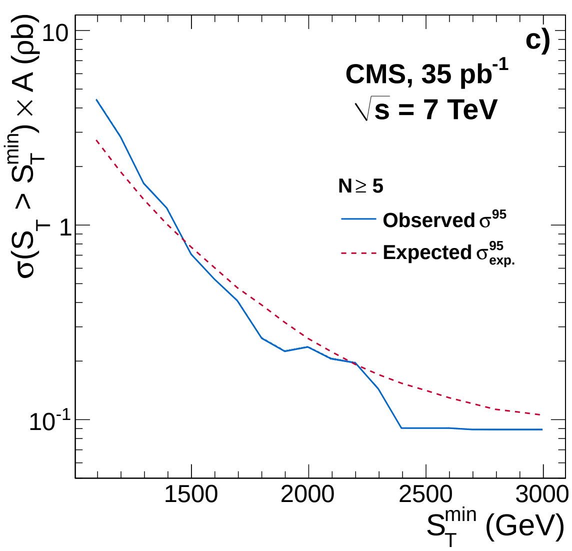

(c) $N \geq 5$

Figure 4.24: Model-independent 95% confidence level upper limits on a signal cross section times acceptance for counting experiments with $S_T > S_T^{min}$ as a function of S_T^{min} for $N \geq 3, 4, 5$.

Table 4.8: Model-independent 95% confidence level upper limits on a signal cross section for counting experiments with $S_{\mathrm{T}} > S_{\mathrm{T}}^{\min}$ and event multiplicity $N \geq N^{\min}$. The signal acceptance is 100% with nominal uncertainty of 5%.

$N^{\min}$	$S_{\mathrm{T}}^{\min}$ (GeV)	n^{data}	n^{bkg}	σ^{95} (pb)	$\sigma^{95}_{\mathrm{exp.}}$ (pb)
3	1100	2002	1945.92 ± 129.02	8.59	7.23
3	1200	1132	1096.98 ± 93.49	6.05	5.21
3	1300	642	641.51 ± 72.68	3.97	3.94
3	1400	370	387.32 ± 57.21	2.62	3.00
3	1500	203	240.51 ± 45.12	1.53	2.28
3	1600	128	153.11 ± 35.58	1.21	1.74
3	1700	82	99.66 ± 28.07	0.94	1.34
3	1800	45	66.17 ± 22.18	0.57	1.03
3	1900	30	44.74 ± 17.57	0.46	0.80
3	2000	21	30.75 ± 13.97	0.39	0.63
3	2100	12	21.46 ± 11.15	0.27	0.50
3	2200	10	15.18 ± 8.93	0.27	0.41
3	2300	5	10.87 ± 7.18	0.18	0.34
3	2400	2	7.88 ± 5.80	0.13	0.28
3	2500	2	5.77 ± 4.71	0.13	0.24
3	2600	0	4.27 ± 3.83	0.09	0.21
3	2700	0	3.18 ± 3.13	0.09	0.18
3	2800	0	$2.40\,^{+2.57}_{-2.40}$	0.09	0.17
3	2900	0	$1.82\,^{+2.11}_{-1.82}$	0.09	0.15
3	3000	0	$1.39\,^{+1.75}_{-1.39}$	0.09	0.14
4	1100	1207	1096.13 ± 81.75	7.54	4.70
4	1200	688	617.93 ± 56.96	5.06	3.30
4	1300	387	361.36 ± 42.85	3.04	2.44

Continued on Next Page

Table 4.8 Model Independent Limits – Continued

$N^{\min}$	$S_{\mathrm{T}}^{\min}$ (GeV)	n^{data}	n^{bkg}	σ^{95} (pb)	$\sigma^{95}_{\mathrm{exp.}}$ (pb)
4	1400	217	218.18 ± 33.10	1.81	1.84
4	1500	111	135.48 ± 25.83	0.90	1.40
4	1600	73	86.24 ± 20.25	0.78	1.08
4	1700	42	56.14 ± 15.92	0.52	0.83
4	1800	21	37.28 ± 12.56	0.31	0.65
4	1900	13	25.20 ± 9.93	0.25	0.52
4	2000	11	17.32 ± 7.89	0.26	0.42
4	2100	6	12.09 ± 6.29	0.19	0.34
4	2200	5	8.55 ± 5.04	0.19	0.29
4	2300	3	6.12 ± 4.05	0.15	0.24
4	2400	1	4.44 ± 3.27	0.11	0.21
4	2500	1	3.25 ± 2.65	0.11	0.18
4	2600	0	2.40 ± 2.16	0.09	0.16
4	2700	0	1.79 ± 1.77	0.09	0.15
4	2800	0	$1.35\ ^{+1.45}_{-1.35}$	0.09	0.14
4	2900	0	$1.02\ ^{+1.19}_{-1.02}$	0.09	0.13
4	3000	0	$0.78\ ^{+0.98}_{-0.78}$	0.09	0.12
5	1100	560	495.45 ± 45.86	4.38	2.73
5	1200	317	279.30 ± 30.16	2.79	1.86
5	1300	175	163.33 ± 21.47	1.61	1.34
5	1400	108	98.62 ± 15.97	1.22	1.00
5	1500	59	61.24 ± 12.17	0.70	0.77
5	1600	36	38.98 ± 9.41	0.52	0.60
5	1700	23	25.37 ± 7.33	0.41	0.47

Continued on Next Page

Table 4.8 Model Independent Limits – Continued

N^{min}	$S_{\text{T}}^{\text{min}}$ (GeV)	n^{data}	n^{bkg}	σ^{95} (pb)	$\sigma^{95}_{\text{exp.}}$ (pb)
5	1800	12	16.85 ± 5.75	0.26	0.38
5	1900	8	11.39 ± 4.53	0.22	0.31
5	2000	7	7.83 ± 3.59	0.23	0.26
5	2100	5	5.46 ± 2.86	0.21	0.22
5	2200	4	3.86 ± 2.29	0.19	0.19
5	2300	2	2.77 ± 1.84	0.14	0.17
5	2400	0	2.01 ± 1.48	0.09	0.15
5	2500	0	1.47 ± 1.20	0.09	0.14
5	2600	0	1.09 ± 0.98	0.09	0.13
5	2700	0	0.81 ± 0.80	0.09	0.12
5	2800	0	$0.61\ ^{+0.66}_{-0.61}$	0.09	0.11
5	2900	0	$0.46\ ^{+0.54}_{-0.46}$	0.09	0.11
5	3000	0	$0.35\ ^{+0.44}_{-0.35}$	0.09	0.10

4.6 Miscellaneous Cross-Checks

4.6.1 Muon and MET Dataset

Since a muon deposits very little energy in calorimeters, it is not reconstructed as jet at the HLT. An event with one or more energetic muon(s) plus multiple jets may not exceed the H_{T} trigger threshold, and therefore is excluded from the

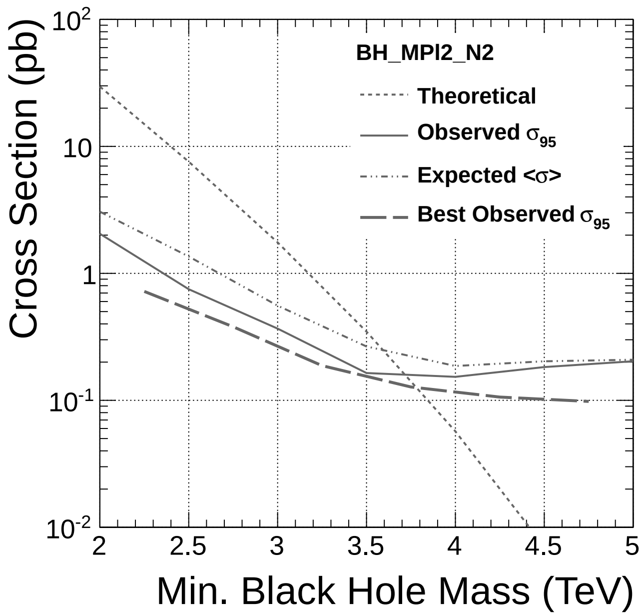

(a) Non-rotating, $M_{\mathrm{D}} = 2.0\ \ \mathrm{TeV}, n = 2$

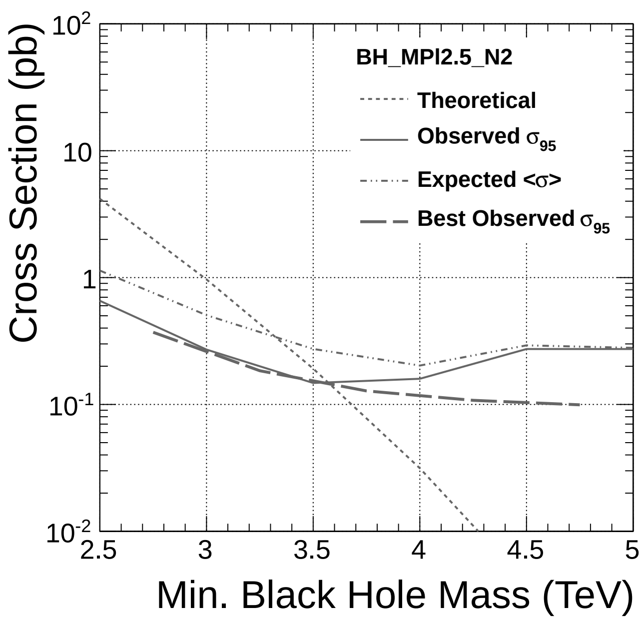

(b) Non-rotating, $M_{\mathrm{D}} = 2.5\ \ \mathrm{TeV}, n = 2$

Figure 4.25: Comparison of upper limit on minimum black hole mass using direct search and model-independent limits table. The observed and expected limits are calculated from direct searches, while the best observed limit are obtained from the model-independent limits.

analysis. Similarly, a high-$\not\!\!E_T$ event with multiple soft jets could also be a black hole candidate without being accepted by H_{T} trigger. To ensure that we do not miss any potential black hole events, the analysis is repeated on the muon and $\not\!\!E_T$ datasets. The muon events are chosen to trigger HLT_Mu* AND NOT HLT_HT*, while the $\not\!\!E_T$ events are selected by requiring HLT_MET* AND NOT HLT_Mu* AND NOT HLT_HT*. Such event selection allows three orthogonal datasets triggered by H_{T}, muon, and $\not\!\!E_T$. Figure 4.26 shows the S_{T} distribution with event multiplicity $N \geq 2$ for muon and $\not\!\!E_T$ datasets. Only a few events are found in the normalization region $600\ \text{GeV} \leq S_{\mathrm{T}} < 1100\ \text{GeV}$, and none of them are found in the search region $S_{\mathrm{T}} > 1100\ \text{GeV}$, which indicates that the analysis is valid by considering only H_{T}-triggered events.

4.6.2 Error Stream

The error stream is a special dataset aims to collect events that failed the HLT processing. The failure could be out-of-time exceptions (e.g. due to high multiplicity of tracks), bugs in the HLT algorithms, or technical issues, such as network problems and buffer overflows. Since black hole candidates are expected to create lots of activities in multiple detectors, the complexity of event signature may cause an exception in HLT process. For event multiplicity $N \geq 2$, most of the events in error stream are below the normalization region. No black hole candidates are found in error stream.

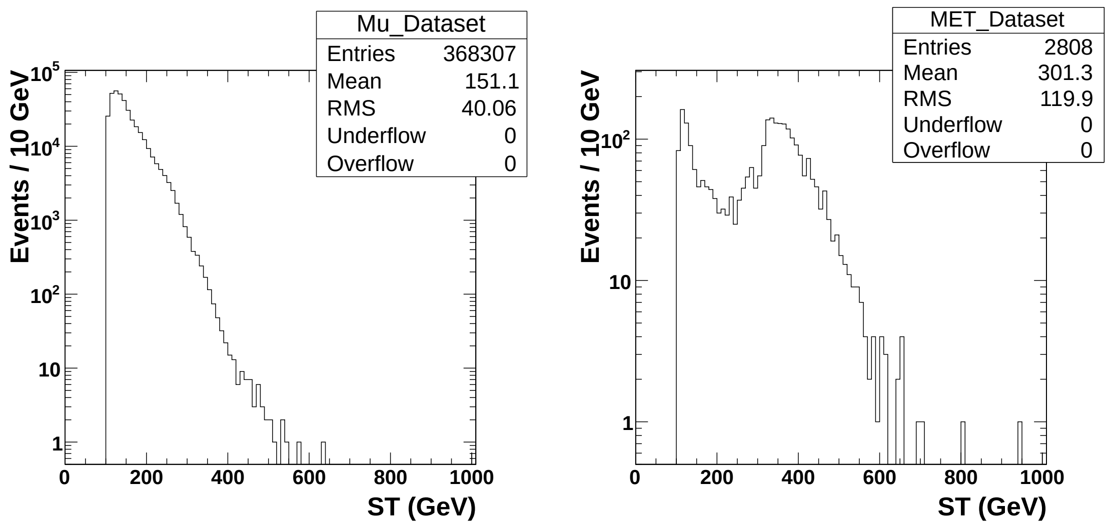

(a) Muon Dataset **(b)** MET Dataset

Figure 4.26: The S_{T} distribution with event multiplicity $N \geq 2$ for muon and $\not{E}_T$ datasets.

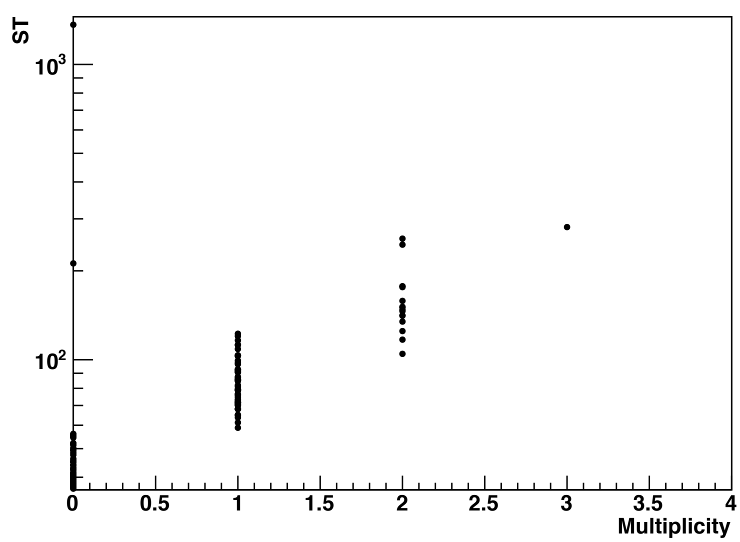

Figure 4.27: The S_{T} distribution *vs.* event multiplicity for events in the HLT error stream.

4.6.3 Effect of Pile-up

In collisions at high luminosity, there is a probability that multiple interactions occur in a single bunch crossing. The global properties, such as S_{T} and event multiplicity, may be over-estimated due to the multiple interactions. Each interaction can be traced down to its original interaction point, i.e. primary vertex. The pile-up events contain more than one primary vertices. Although the rate on pile-up is expected to be very low in the first year of LHC running, the assumption of S_{T} invariant shape is checked explicitly with no effect on pile-up. The fraction of event with single primary vertex in event multiplicity $N = 2$ and $N \geq 3$ are shown in Figure. 4.28. For the region above H_{T} trigger turn-on, the curves are flat, confirming that there is no appreciable effect from the pile-up events.

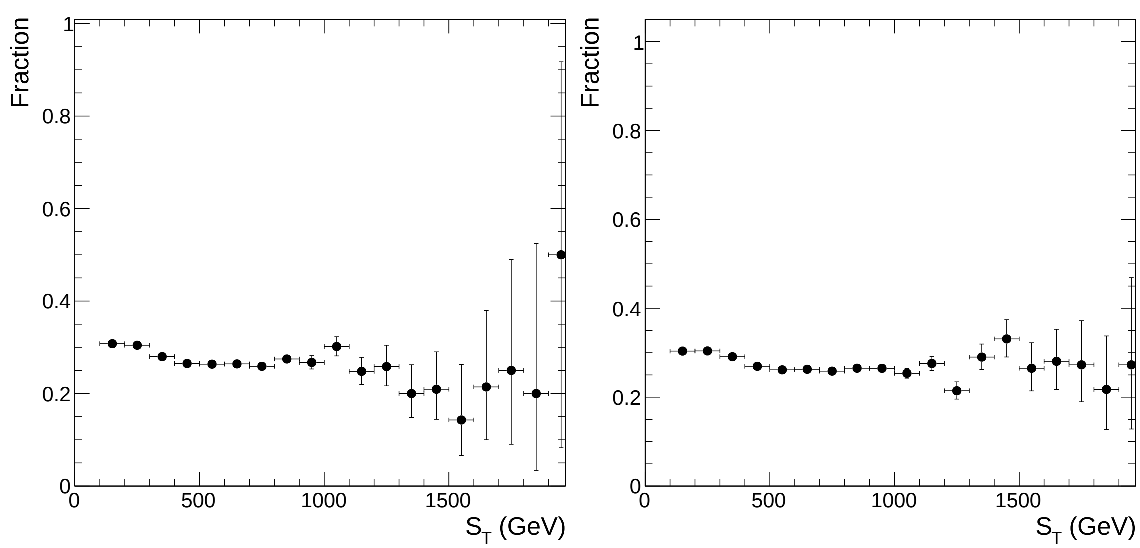

(a) $N = 2$ **(b)** $N \geq 3$

Figure 4.28: Fraction of event with single primary vertex in event multiplicity (a) $N = 2$ and (b) $N \geq 3$.

4.6.4 Signal Acceptance Uncertainty

The background uncertainty arose from shape modeling is dominated in the limit calculation, while the signal acceptance uncertainty is less sensitive. It allows the uniform use of a nominal 5% value on signal acceptance uncertainty in different signal models. In fact, the model-independent limits curves shown in Figure 4.24 represent a side-band variation of 1% - 10%, which is invisible without zooming (Fig. 4.29). The variation on signal acceptance uncertainty is negligible. Therefore, using the nominal value of 5% is valid for the model-independent analysis.

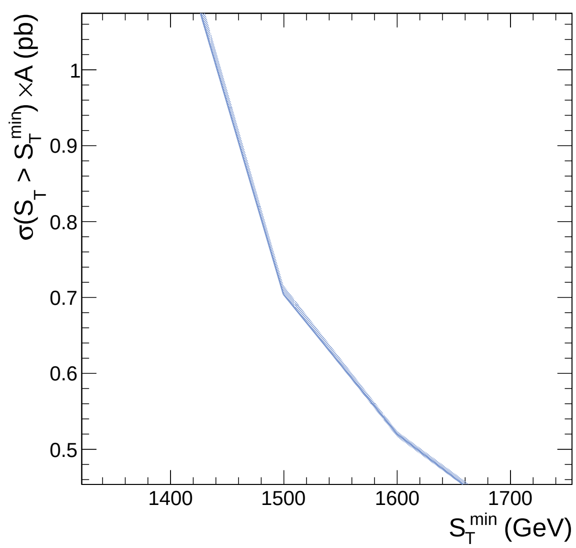

Figure 4.29: Zooming on part of Fig. 4.24c, showing that the side-band of 1% - 10% uncertainty on signal acceptance with nominal value 5% in solid line.

Chapter 5

Conclusions

This Dissertation described a search for microscopic signatures produced by proton-proton collision with a center-of-mass energy of 7 TeV at the LHC. Data taken by CMS experiment in year 2010 with a total integrated luminosity of 34.7 ± 3.8 pb^{-1} was analyzed. Two main variables were introduced: event multiplicity N defined as the number of jets, leptons, and photons with the transverse energy above 50 GeV; the total scalar sum of transverse energy S_{T} of jets, leptons, photons and $\not\!\!E_T$, with a transverse energy threshold of 50 GeV on each object. A novel background estimation technique for multi-jet events in TeV scale was developed, assuming the shape of S_{T} distribution is independent of event multiplicity. The assumption was verified in both multi-jet simulation and data. No excess of data events was observed above the predicted background. The limits on the minimum black hole mass at the 95% confidence level were set in a range from 3.5 to 4.5 TeV for values of the Planck scale up to 3 TeV. In addition, model-independent upper limits on cross section times the acceptance at the 95% confidence level were provided for high-S_{T} inclusive final states for $N \geq 3, 4, 5$.

This work is the first dedicated search for microscopic black holes at a particle accelerator, and the describes first published limits on the black hole production in extra dimensions in space using semi-classical approximation. The model-independent limits are not only applicable to a variety of black hole models, but also constrain a broad range of new physics on the production of energetic and high-multiplicity final states. The results of this Dissertation were published in *Physics Letters B* ***697*** *(2011) 434*.

Appendix A

Black Hole Generator Configurations

A.1 BlackMax: Non-rotating Black Hole

```
Number_of_simulations
16000
incoming_particle(1:pp_2:ppbar_3:ee+)
1
Center_of_mass_energy_of_incoming_particle
7000.
M_pl(GeV)
__MPl__
definition_of_M_pl:(1:M_D_2:M_p_3:M_DL_4:put_in_by_hand)
1
if_definition==4
1.
```

```
Choose_a_case:(1:tensionless_nonrotating_2:tension_nonrotating_3:
    rotating_nonsplit_4:Lisa_two_particles_final_states)
1
number_of_extra_dimensions
__N__
number_of_splitting_dimensions
0
size_of_brane(1/Mpl)
0.0
extradimension_size(1/Mpl)
10.
tension(parameter_of_deficit_angle:1_to_0)
0.0
choose_a_pdf_file(200_to_240_cteq6)Or_>10000_for_LHAPDF
21000
Chose_events_by_center_of_mass_energy_or_by_initial_black_hole_mass
    (1:center_of_mass_2:black_hole_mass)
2
Minimum_mass(GeV)
__Mmin__
Maxmum_mass(GeV)
7000.
Include_string_ball:(1:no_2:yes)
1
String_scale(M_s)(GeV)
1000
string_coupling(g_s)
0.8
The_minimum_mass_of_a_string_ball_or_black_hole(in_unit_Mpl)
```

```
1.
fix_time_step(1:fix_2:no)
2
time_step(1/GeV)
1.e-5
other_definition_of_cross_section(0:no_1:yoshino_2:pi*r^2_3:4pi*r
    ^2)
0
calculate_the_cross_section_according_to(0:
    the_radius_of_initial_black_hole_1:centre_of_mass_energy)
0
calculate_angular_eigen_value(0:calculate_1:fitting_result)
0
Mass_loss_factor(0~1.0)
0.0
momentum_loss_factor(0~1.0)
0.0
Angular_momentum_loss_factor(0~1.0)
0.0
turn_on_graviton(0:off_1:on)
0
Seed
123589541
Write_LHA_Output_Record?_0=NO__1=Yes_2=More_Detailed_output
2
L_suppression(1:none_2:delta_area_3:anular_momentum_4:
    delta_angular_momentum)
1
angular_momentum_suppression_factor
```

```
1
charge_suppression(1:none_2:do)
1
charge_suppression_factor
1
color_suppression_factor
20
split_fermion_width(1/Mpl)_and_location(from−15to15)(
    up_to_9extradimensions)
u_quark_Right(Note:do_not_insert_blank_spaces)
1.0
10.0,0.0,0.0,0.0,0.0,0.0,0.0,0.0,0.0
u_quark_Left(Note:do_not_insert_blank_spaces)
1.0
10.0,0.0,0.0,0.0,0.0,0.0,0.0,0.0,0.0
u_bar_quark_Right(Note:do_not_insert_blank_spaces)
1.0
10.0,0.0,0.0,0.0,0.0,0.0,0.0,0.0,0.0
u_bar_quark_Left(Note:do_not_insert_blank_spaces)
1.0
10.0,0.0,0.0,0.0,0.0,0.0,0.0,0.0,0.0
d_quark_Right(Note:do_not_insert_blank_spaces)
1.0
10.0,0.0,0.0,0.0,0.0,0.0,0.0,0.0,0.0
d_quark_Left(Note:do_not_insert_blank_spaces)
1.0
10.0,0.0,0.0,0.0,0.0,0.0,0.0,0.0,0.0
d_bar_quark_Right(Note:do_not_insert_blank_spaces)
1.0
```

```
10.0,0.0,0.0,0.0,0.0,0.0,0.0,0.0,0.0
d_bar_quark_Left(Note:do_not_insert_blank_spaces)
1.0
10.0,0.0,0.0,0.0,0.0,0.0,0.0,0.0,0.0
s_quark_Right(Note:do_not_insert_blank_spaces)
1.0
10.0,0.0,0.0,0.0,0.0,0.0,0.0,0.0,0.0
s_quark_Left(Note:do_not_insert_blank_spaces)
1.0
10.0,0.0,0.0,0.0,0.0,0.0,0.0,0.0,0.0
s_bar_quark_Right(Note:do_not_insert_blank_spaces)
1.0
10.0,0.0,0.0,0.0,0.0,0.0,0.0,0.0,0.0
s_bar_quark_Left(Note:do_not_insert_blank_spaces)
1.0
10.0,0.0,0.0,0.0,0.0,0.0,0.0,0.0,0.0
c_quark_Right(Note:do_not_insert_blank_spaces)
1.0
10.0,0.0,0.0,0.0,0.0,0.0,0.0,0.0,0.0
c_quark_Left(Note:do_not_insert_blank_spaces)
1.0
10.0,0.0,0.0,0.0,0.0,0.0,0.0,0.0,0.0
c_bar_quark_Right(Note:do_not_insert_blank_spaces)
1.0
10.0,0.0,0.0,0.0,0.0,0.0,0.0,0.0,0.0
c_bar_quark_Left(Note:do_not_insert_blank_spaces)
1.0
10.0,0.0,0.0,0.0,0.0,0.0,0.0,0.0,0.0
b_quark_Right(Note:do_not_insert_blank_spaces)
```

```
1.0
10.0,0.0,0.0,0.0,0.0,0.0,0.0,0.0,0.0
b_quark_Left(Note:do_not_insert_blank_spaces)
1.0
10.0,0.0,0.0,0.0,0.0,0.0,0.0,0.0,0.0
b_bar_quark_Right(Note:do_not_insert_blank_spaces)
1.0
10.0,0.0,0.0,0.0,0.0,0.0,0.0,0.0,0.0
b_bar_quark_Left(Note:do_not_insert_blank_spaces)
1.0
10.0,0.0,0.0,0.0,0.0,0.0,0.0,0.0,0.0
t_quark_Right(Note:do_not_insert_blank_spaces)
1.0
10.0,0.0,0.0,0.0,0.0,0.0,0.0,0.0,0.0
t_quark_Left(Note:do_not_insert_blank_spaces)
1.0
10.0,0.0,0.0,0.0,0.0,0.0,0.0,0.0,0.0
t_bar_quark_Right(Note:do_not_insert_blank_spaces)
1.0
10.0,0.0,0.0,0.0,0.0,0.0,0.0,0.0,0.0
t_bar_quark_Left(Note:do_not_insert_blank_spaces)
1.0
10.0,0.0,0.0,0.0,0.0,0.0,0.0,0.0,0.0
e_-_Left(Note:do_not_insert_blank_spaces)
1.0
-10.0,0.0,0.0,0.0,0.0,0.0,0.0,0.0,0.0
e_-_Right(Note:do_not_insert_blank_spaces)
1.0
-10.0,0.0,0.0,0.0,0.0,0.0,0.0,0.0,0.0
```

```
e_+_Left(Note:do_not_insert_blank_spaces)
1.0
-10.0,0.0,0.0,0.0,0.0,0.0,0.0,0.0,0.0
e_+_Right(Note:do_not_insert_blank_spaces)
1.0
-10.0,0.0,0.0,0.0,0.0,0.0,0.0,0.0,0.0
mu_-_Left(Note:do_not_insert_blank_spaces)
1.0
-10.0,0.0,0.0,0.0,0.0,0.0,0.0,0.0,0.0
mu_-_Right(Note:do_not_insert_blank_spaces)
1.0
-10.0,0.0,0.0,0.0,0.0,0.0,0.0,0.0,0.0
mu_+_Left(Note:do_not_insert_blank_spaces)
1.0
-10.0,0.0,0.0,0.0,0.0,0.0,0.0,0.0,0.0
mu_+_Right(Note:do_not_insert_blank_spaces)
1.0
-10.0,0.0,0.0,0.0,0.0,0.0,0.0,0.0,0.0
tau_-_Left(Note:do_not_insert_blank_spaces)
1.0
-10.0,0.0,0.0,0.0,0.0,0.0,0.0,0.0,0.0
tau_-_Right(Note:do_not_insert_blank_spaces)
1.0
-10.0,0.0,0.0,0.0,0.0,0.0,0.0,0.0,0.0
tau_+_Left(Note:do_not_insert_blank_spaces)
1.0
-10.0,0.0,0.0,0.0,0.0,0.0,0.0,0.0,0.0
tau_+_Right(Note:do_not_insert_blank_spaces)
1.0
```

```
-10.0,0.0,0.0,0.0,0.0,0.0,0.0,0.0,0.0
nutrino_e-(Note:do_not_insert_blank_spaces)
1.0
-10.0,0.0,0.0,0.0,0.0,0.0,0.0,0.0,0.0
nutrino_e+(Note:do_not_insert_blank_spaces)
1.0
-10.0,0.0,0.0,0.0,0.0,0.0,0.0,0.0,0.0
nutrino_mu-(Note:do_not_insert_blank_spaces)
1.0
-10.0,0.0,0.0,0.0,0.0,0.0,0.0,0.0,0.0
nutrino_mu+(Note:do_not_insert_blank_spaces)
1.0
-10.0,0.0,0.0,0.0,0.0,0.0,0.0,0.0,0.0
nutrino_tau-(Note:do_not_insert_blank_spaces)
1.0
-10.0,0.0,0.0,0.0,0.0,0.0,0.0,0.0,0.0
nutrino_tau+(Note:do_not_insert_blank_spaces)
1.0
-10.0,0.0,0.0,0.0,0.0,0.0,0.0,0.0,0.0
number_of_conservation
1
d,s,b,u,c,t,e,mu,tau,nu_e,nu_mu,nu_tau
1,1,1,1,1,1,0,0,0,0,0,0
1,1,1,1,1,1,-3,-3,-3,-3,-3,-3
0,0,0,0,0,0,1,1,1,1,1,1
0,0,0,0,0,0,0,0,0,0,0,0
0,0,0,0,0,0,0,0,0,0,0,0
0,0,0,0,0,0,0,0,0,0,0,0
0,0,0,0,0,0,0,0,0,0,0,0
```

A.2 BlackMax: Rotating Black Hole

```
Number_of_simulations
12000
incoming_particle(1:pp_2:ppbar_3:ee+)
1
Center_of_mass_energy_of_incoming_particle
7000.
M_pl(GeV)
__MPl__
definition_of_M_pl:(1:M_D_2:M_p_3:M_DL_4:put_in_by_hand)
1
if_definition==4
1.
Choose_a_case:(1:tensionless_nonrotating_2:tension_nonrotating_3:
    rotating_nonsplit_4:Lisa_two_particles_final_states)
3
number_of_extra_dimensions
__N__
number_of_splitting_dimensions
0
size_of_brane(1/Mpl)
0.0
extradimension_size(1/Mpl)
10.
tension(parameter_of_deficit_angle:1_to_0)
0.0
choose_a_pdf_file(200_to_240_cteq6)Or_>10000_for_LHAPDF
21000
```

```
Chose_events_by_center_of_mass_energy_or_by_initial_black_hole_mass
    (1:center_of_mass_2:black_hole_mass)
2
Minimum_mass(GeV)
__Mmin__
Maxmum_mass(GeV)
7000.
Include_string_ball:(1:no_2:yes)
1
String_scale(M_s)(GeV)
1000
string_coupling(g_s)
0.8
The_minimum_mass_of_a_string_ball_or_black_hole(in_unit_Mpl)
1.
fix_time_step(1:fix_2:no)
2
time_step(1/GeV)
1.e-5
other_definition_of_cross_section(0:no_1:yoshino_2:pi*r^2_3:4pi*r
    ^2)
0
calculate_the_cross_section_according_to(0:
    the_radius_of_initial_black_hole_1:centre_of_mass_energy)
0
calculate_angular_eigen_value(0:calculate_1:fitting_result)
0
Mass_loss_factor(0~1.0)
0.0
```

```
momentum_loss_factor(0~1.0)
0.0
Angular_momentum_loss_factor(0~1.0)
0.0
turn_on_graviton(0:off_1:on)
0
Seed
123589541
Write_LHA_Output_Record?_0=NO__1=Yes_2=More_Detailed_output
2
L_suppression(1:none_2:delta_area_3:anular_momentum_4:
    delta_angular_momentum)
1
angular_momentum_suppression_factor
1
charge_suppression(1:none_2:do)
1
charge_suppression_factor
1
color_suppression_factor
20
split_fermion_width(1/Mpl)_and_location(from-15to15)(
    up_to_9extradimensions)
u_quark_Right(Note:do_not_insert_blank_spaces)
1.0
10.0,0.0,0.0,0.0,0.0,0.0,0.0,0.0,0.0
u_quark_Left(Note:do_not_insert_blank_spaces)
1.0
10.0,0.0,0.0,0.0,0.0,0.0,0.0,0.0,0.0
```

```
u_bar_quark_Right(Note:do_not_insert_blank_spaces)
1.0
10.0,0.0,0.0,0.0,0.0,0.0,0.0,0.0,0.0
u_bar_quark_Left(Note:do_not_insert_blank_spaces)
1.0
10.0,0.0,0.0,0.0,0.0,0.0,0.0,0.0,0.0
d_quark_Right(Note:do_not_insert_blank_spaces)
1.0
10.0,0.0,0.0,0.0,0.0,0.0,0.0,0.0,0.0
d_quark_Left(Note:do_not_insert_blank_spaces)
1.0
10.0,0.0,0.0,0.0,0.0,0.0,0.0,0.0,0.0
d_bar_quark_Right(Note:do_not_insert_blank_spaces)
1.0
10.0,0.0,0.0,0.0,0.0,0.0,0.0,0.0,0.0
d_bar_quark_Left(Note:do_not_insert_blank_spaces)
1.0
10.0,0.0,0.0,0.0,0.0,0.0,0.0,0.0,0.0
s_quark_Right(Note:do_not_insert_blank_spaces)
1.0
10.0,0.0,0.0,0.0,0.0,0.0,0.0,0.0,0.0
s_quark_Left(Note:do_not_insert_blank_spaces)
1.0
10.0,0.0,0.0,0.0,0.0,0.0,0.0,0.0,0.0
s_bar_quark_Right(Note:do_not_insert_blank_spaces)
1.0
10.0,0.0,0.0,0.0,0.0,0.0,0.0,0.0,0.0
s_bar_quark_Left(Note:do_not_insert_blank_spaces)
1.0
```

```
10.0,0.0,0.0,0.0,0.0,0.0,0.0,0.0,0.0
c_quark_Right(Note:do_not_insert_blank_spaces)
1.0
10.0,0.0,0.0,0.0,0.0,0.0,0.0,0.0,0.0
c_quark_Left(Note:do_not_insert_blank_spaces)
1.0
10.0,0.0,0.0,0.0,0.0,0.0,0.0,0.0,0.0
c_bar_quark_Right(Note:do_not_insert_blank_spaces)
1.0
10.0,0.0,0.0,0.0,0.0,0.0,0.0,0.0,0.0
c_bar_quark_Left(Note:do_not_insert_blank_spaces)
1.0
10.0,0.0,0.0,0.0,0.0,0.0,0.0,0.0,0.0
b_quark_Right(Note:do_not_insert_blank_spaces)
1.0
10.0,0.0,0.0,0.0,0.0,0.0,0.0,0.0,0.0
b_quark_Left(Note:do_not_insert_blank_spaces)
1.0
10.0,0.0,0.0,0.0,0.0,0.0,0.0,0.0,0.0
b_bar_quark_Right(Note:do_not_insert_blank_spaces)
1.0
10.0,0.0,0.0,0.0,0.0,0.0,0.0,0.0,0.0
b_bar_quark_Left(Note:do_not_insert_blank_spaces)
1.0
10.0,0.0,0.0,0.0,0.0,0.0,0.0,0.0,0.0
t_quark_Right(Note:do_not_insert_blank_spaces)
1.0
10.0,0.0,0.0,0.0,0.0,0.0,0.0,0.0,0.0
t_quark_Left(Note:do_not_insert_blank_spaces)
```

```
1.0
10.0,0.0,0.0,0.0,0.0,0.0,0.0,0.0,0.0
t_bar_quark_Right(Note:do_not_insert_blank_spaces)
1.0
10.0,0.0,0.0,0.0,0.0,0.0,0.0,0.0,0.0
t_bar_quark_Left(Note:do_not_insert_blank_spaces)
1.0
10.0,0.0,0.0,0.0,0.0,0.0,0.0,0.0,0.0
e_-_Left(Note:do_not_insert_blank_spaces)
1.0
-10.0,0.0,0.0,0.0,0.0,0.0,0.0,0.0,0.0
e_-_Right(Note:do_not_insert_blank_spaces)
1.0
-10.0,0.0,0.0,0.0,0.0,0.0,0.0,0.0,0.0
e_+_Left(Note:do_not_insert_blank_spaces)
1.0
-10.0,0.0,0.0,0.0,0.0,0.0,0.0,0.0,0.0
e_+_Right(Note:do_not_insert_blank_spaces)
1.0
-10.0,0.0,0.0,0.0,0.0,0.0,0.0,0.0,0.0
mu_-_Left(Note:do_not_insert_blank_spaces)
1.0
-10.0,0.0,0.0,0.0,0.0,0.0,0.0,0.0,0.0
mu_-_Right(Note:do_not_insert_blank_spaces)
1.0
-10.0,0.0,0.0,0.0,0.0,0.0,0.0,0.0,0.0
mu_+_Left(Note:do_not_insert_blank_spaces)
1.0
-10.0,0.0,0.0,0.0,0.0,0.0,0.0,0.0,0.0
```

```
mu_+_Right(Note:do_not_insert_blank_spaces)
1.0
-10.0,0.0,0.0,0.0,0.0,0.0,0.0,0.0,0.0
tau_-_Left(Note:do_not_insert_blank_spaces)
1.0
-10.0,0.0,0.0,0.0,0.0,0.0,0.0,0.0,0.0
tau_-_Right(Note:do_not_insert_blank_spaces)
1.0
-10.0,0.0,0.0,0.0,0.0,0.0,0.0,0.0,0.0
tau_+_Left(Note:do_not_insert_blank_spaces)
1.0
-10.0,0.0,0.0,0.0,0.0,0.0,0.0,0.0,0.0
tau_+_Right(Note:do_not_insert_blank_spaces)
1.0
-10.0,0.0,0.0,0.0,0.0,0.0,0.0,0.0,0.0
nutrino_e-(Note:do_not_insert_blank_spaces)
1.0
-10.0,0.0,0.0,0.0,0.0,0.0,0.0,0.0,0.0
nutrino_e+(Note:do_not_insert_blank_spaces)
1.0
-10.0,0.0,0.0,0.0,0.0,0.0,0.0,0.0,0.0
nutrino_mu-(Note:do_not_insert_blank_spaces)
1.0
-10.0,0.0,0.0,0.0,0.0,0.0,0.0,0.0,0.0
nutrino_mu+(Note:do_not_insert_blank_spaces)
1.0
-10.0,0.0,0.0,0.0,0.0,0.0,0.0,0.0,0.0
nutrino_tau-(Note:do_not_insert_blank_spaces)
1.0
```

```
-10.0,0.0,0.0,0.0,0.0,0.0,0.0,0.0,0.0
nutrino_tau+(Note:do_not_insert_blank_spaces)
1.0
-10.0,0.0,0.0,0.0,0.0,0.0,0.0,0.0,0.0
number_of_conservation
1
d,s,b,u,c,t,e,mu,tau,nu_e,nu_mu,nu_tau
1,1,1,1,1,1,0,0,0,0,0,0
1,1,1,1,1,1,-3,-3,-3,-3,-3,-3
0,0,0,0,0,0,1,1,1,1,1,1
0,0,0,0,0,0,0,0,0,0,0,0
0,0,0,0,0,0,0,0,0,0,0,0
0,0,0,0,0,0,0,0,0,0,0,0
0,0,0,0,0,0,0,0,0,0,0,0
```

A.3 charybdis 2: Stable Remnant

```
********************************************************************

********************  CHARYBDIS2 RUN PARAMETERS
    *********************
********************************************************************


INSTRUCTIONS/DESCRIPTION (PLEASE READ CAREFULLY!!!):

Below is a list of all the switches that may be changed from the
    internal default values in charybdis2. This has been divided
    into logical sections to facilitate the identification of the
    parameter you want to change from default.

The basic rules are:

     1) First write the name of the variable you want to set in
        the begining of the line followed by a colon ':' without
        spaces;

     2) In the next line you write the value you want to give it.
        If you do not wish to change the default value you can
        just write "default" instead (quotes not present -- see
        for example the variable PDFGUP below) or remove the
        variable from the list (the former is preferred).

Any other lines that you enter are treated as comments as long as
```

they don't start with the name of a valid variable.

The list below has been constructed using this rule. In addition, extra lines with informative text were introduced. For example, in front of the name of the varable, any extra information can be entered. Examples of such are the default values for each variable which are provided in parenthesis in front of the name of the variable (see any below).

Even though the extra informative lines and comments in this file are not used, we advise you to keep them to make it more readable and self explanatory.

!!

!!!!!!!!!!! WARNING: Do not remove or change the !!!!!!!!!!!!!!
!!!!!!!!!!! "END OF INPUT" line at the end of the file! !!!!!!!!!!!!!!
!!

****

********************** START OF INPUT OPTIONS **********************
****

```
----------------------------------
------ Beams & Energies ------
----------------------------------
IDBMUP(1): (default is 2212)
2212
IDBMUP(2): (default is 2212)
2212
EBMUP(1): (default is 7000.0)
3500.0
EBMUP(2): (default is 7000.0)
3500.0
MINMSS: (default is 5000.0)
__Mmin__.0
MAXMSS: (default is 14000.0)
7000.0
PDFGUP(1): (Default depends on specific implementation)
default
PDFGUP(2): (Default depends on specific implementation)
default
LHAPDFSET: (default is 10000 -- needs to be set if you're using
   LHAPDF)
21000
----------------------------
------ MC & OUTPUT ------
----------------------------
CHNMAXEV: (default is 100)
12000
NRN(1): (default is 245234)
245234
```

```
NRN(2): (default is 42542)
42542
LHEFILENAME: (default is lhouches -- must be exactly 8 characters
    long!!!)
lhouches
HISFILENAME: (default is histfile -- must be exactly 8 characters
    long!!!)
histfile
BHLHOUCHES: (default is F -- means .FALSE.)
F
IBHPRN: (default is 1)
1
------------------------------------------------------------
------- Model parameters and conventions -------
------------------------------------------------------------
TOTDIM: (default is 6)
__N__
MPLNCK: (default is 1000.0)
__MPl__.0
MSSDEF: (default is 3 -- PDG definition)
3
YRCSEC: (default is T -- means .TRUE.)
T
MJLOST: (default is T -- means .TRUE.)
F
USEMINMSSBH: (default is T -- means .TRUE.)
T
CVBIAS: (default is F -- means .FALSE.)
F
```

```
FMLOST: (default is 0.99)
 0.99
GTSCA: (default is F)
F
NLEPTONCSV(0): (default is F -- means .FALSE.)
F
NLEPTONCSV(1): (default is F -- means .FALSE.)
F
NLEPTONCSV(2): (default is F -- means .FALSE.)
F
NLEPTONCSV(3): (default is F -- means .FALSE.)
F
DGSB: (default is F)
F
DGGS: (default is 0.3)
 0.3
DGMS: (default is 1000.0)
 1000.0
--------------------------------------
------ Evaporation switches ------
--------------------------------------
BHSPIN: (default is T)
T
BHJVAR: (default is T)
T
BHANIS: (default is T)
T
GRYBDY: (default is T)
T
```

```
TIMVAR: (default is T)
T
MSSDEC: (default is 3)
3
RECOIL: (default is 2)
2
THWMAX: (default is 1000.0)
1000.0
DGTENSION: (default is 1000.0)
1000.0
------------------------------------------------------------
------ Switches for termination of evaporation ------
------------------------------------------------------------
NBODYAVERAGE: (default is T)
F
KINCUT: (default is F)
F
SKIP2REMNANT: (default is F)
F
----------------------------------------
------ Remnant model switches ------
----------------------------------------
NBODY: (default is 2)
2
NBODYPHASE: (default is F)
F
NBODYVAR: (default is F)
F
RMBOIL: (default is F)
```

F

RMSTAB: (default is F)

T

RMMINM: (default is 100.0)

100.0

****

*****************************END*OF*INPUT

****

****

Appendix B

Event Display of a Black Hole Candidate

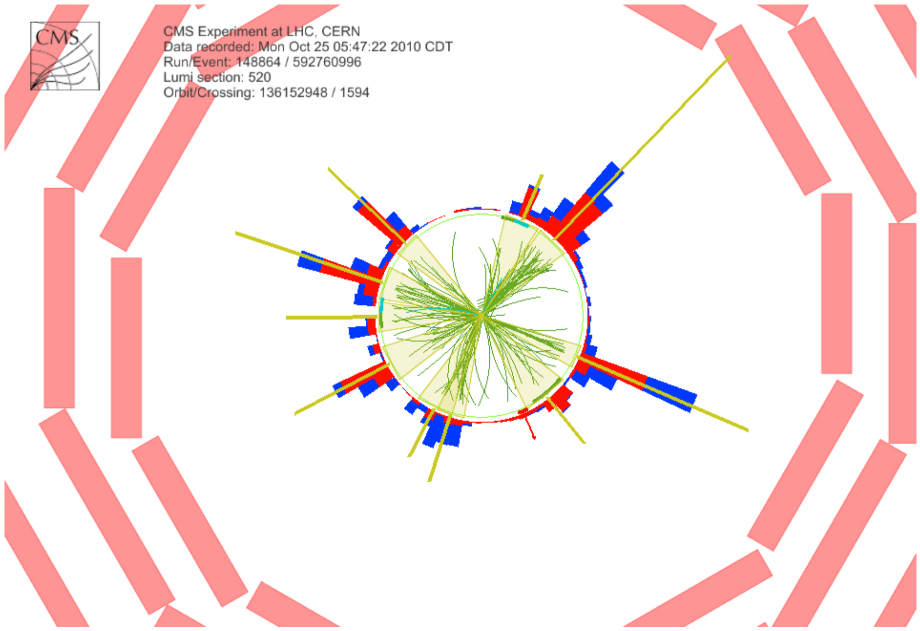

(a) $\rho - \phi$ View

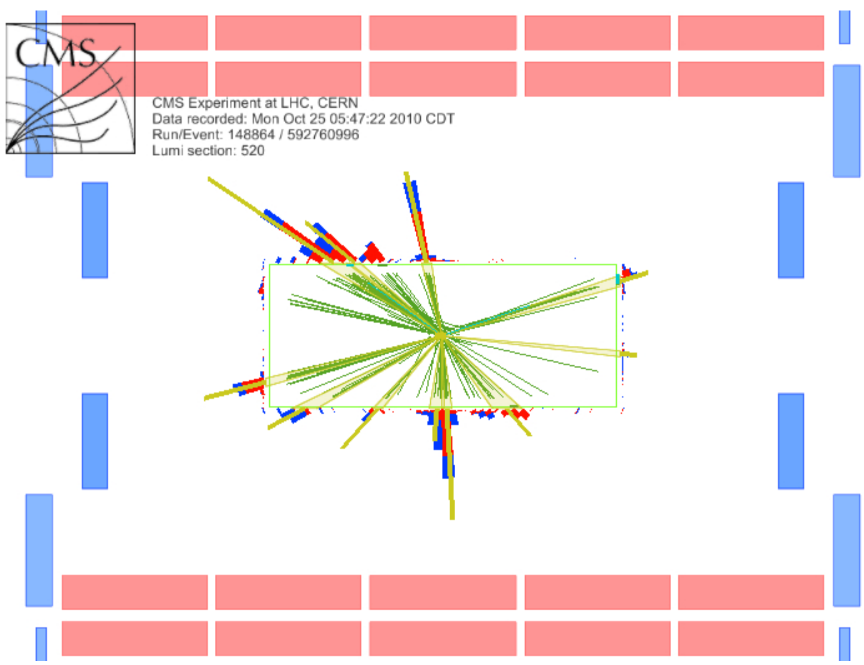

(b) $\rho - z$ View

Figure B.1: Event display of black hole candidate with event multiplicity $N = 10$.

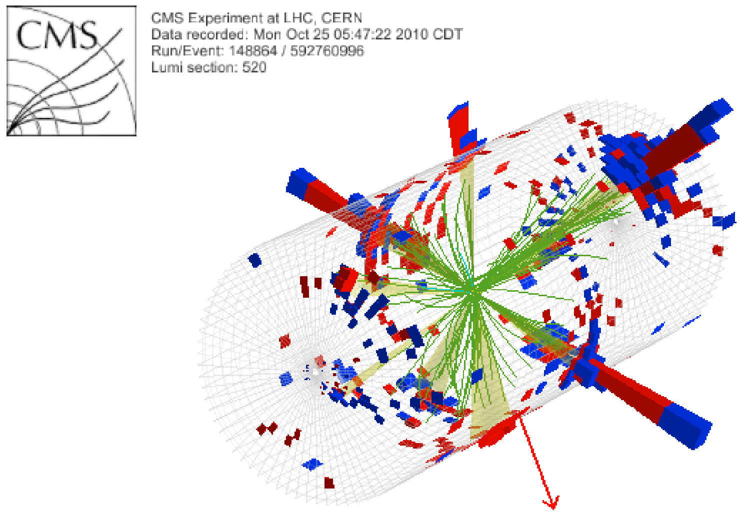

(c) 3D View

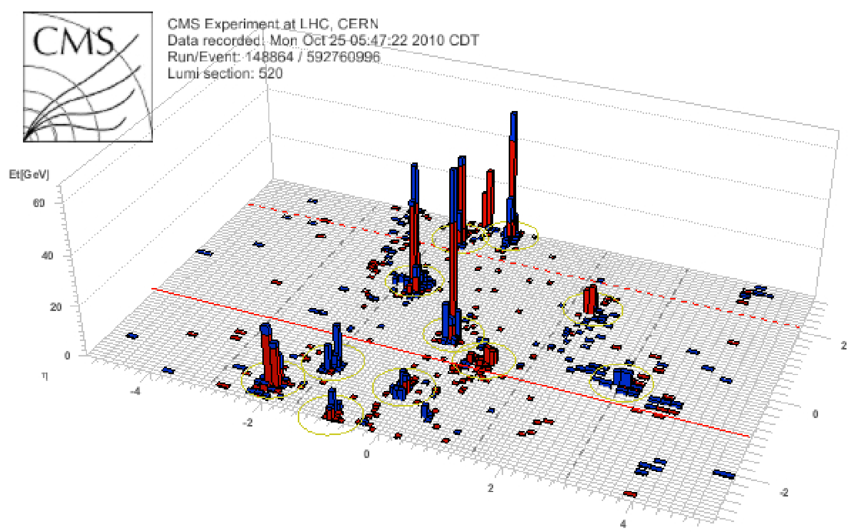

(d) 3D Lego View

Figure B.1: Event display of black hole candidate with event multiplicity $N = 10$.

Bibliography

[1] S. Dimopoulos and G. Landsberg, Phys. Rev. Lett. **87**, 161602 (2001).

[2] S. B. Giddings and S. Thomas, Phys. Rev. D **65**, 56010 (2002).

[3] N. Arkani-Hamed, S. Dimopoulos, and G. Dvali, Phys. Lett. B **429**, 263 (1998).

[4] S. W. Hawking, Nature **248**, 30 (1974).

[5] D.-C. Dai *et al.*, Phys. Rev. D **77**, 76007 (2008).

[6] J. A. Frost *et al.*, JHEP **10**, 014 (2009).

[7] M. Kobayashi and T. Maskawa, Prog. Theor. Phys. **49**, 652 (1973).

[8] S. Glashow, Nucl. Phys. **22**, 579 (1961).

[9] S. Weinberg, Phys. Rev. Lett. **19**, 1264 (1967).

[10] A. Salam, *Weak and Electromagnetic Interactions* , Originally printed in "Svartholm: Elementary Particle Theory, Proceedings Of The Nobel Symposium Held 1968 At Lerum, Sweden", Stockholm 1968, 367-377.

[11] M. Gell-Mann, Il Nuovo Cimento **4**, 848 (1956).

[12] K. Nishijima, Prog. Theor. Phys. **13**, 285 (1955).

[13] P. W. Higgs, Phys. Lett. **12**, 132 (1964).

[14] F. Englert and R. Brout, Phys. Rev. Lett. **13**, 321 (1964).

[15] G. S. Guralnik, C. R. Hagen, and T. W. Kibble, Phys. Rev. Lett. **13**, 585 (1964).

[16] K. Nakamura and P. D. Group, J. Phys. G **37**, 5021 (2010).

[17] D. Hanneke, S. Fogwell, and G. Gabrielse, Phys. Rev. Lett. **100**, 120801 (2008).

[18] D. B. Chitwood *et al.*, Phys. Rev. Lett. **99**, 32001 (2007).

[19] Fast Collaboration, Phys. Lett. B **663**, 172 (2008).

[20] M. C. Gonzalez-Garcia and Y. Nir, Rev. Mod. Phys. **75**, 345 (2003).

[21] R. N. Mohapatra *et al.*, Rep. Prog. Phys. **70**, 1757 (2007).

[22] M. C. Gonzalez-Garcia and M. Maltoni, Phys. Rep. **460**, 1 (2008).

[23] B. Andersson, G. Gustafson, G. Ingelman, and T. Sjöstrand, Phys. Rep. **97**, 31 (1983).

[24] T. Sjostrand, S. Mrenna, and P. Skands, JHEP **05**, 026 (2006).

[25] J. Michell, Philos. Trans. R. Soc. London **74**, 35 (1784).

[26] A. Einstein, Ann. Phys. **354**, 769 (1916).

[27] K. Schwarzschild, Sitzungsberichte der Königlich Preussischen Akademie der Wissenschaften zu Berlin , 189 (1916).

[28] G. D. Birkhoff and R. E. Langer, Relativity and modern physics (1923).

[29] J. D. Bekenstein, Phys. Rev. D **7**, 2333 (1973).

[30] W. Heisenberg, Z. Phys. **43**, 172 (1927).

[31] S. W. Hawking, Commun. Math. Phys **43**, 199 (1975).

[32] W. G. Unruh, Phys. Rev. D **14**, 870 (1976).

[33] R. P. Kerr, Phys. Rev. Lett. **11**, 237 (1963).

[34] R. Penrose and G. R. Floyd, Nature Physical Science **229**, 177 (1971).

[35] D. Christodoulou, Phys. Rev. Lett. **25**, 1596 (1970).

[36] E. T. Newman *et al.*, J. Math. Phy **6**, 918 (1965).

[37] P. O. Mazur, J. Phys. A **15**, 3173 (1982).

[38] W. Israel, Physical Review **164**, 1776 (1967).

[39] W. Israel, Commun. Math. Phys **8**, 245 (1968).

[40] B. Carter, Phys. Rev. Lett. **26**, 331 (1971).

[41] D. C. Robinson, Phys. Rev. Lett. **34**, 905 (1975).

[42] D. C. Robinson, Phys. Rev. D **10**, 458 (1974).

[43] C. W. Misner, K. S. Thorne, and J. A. Wheeler, *Gravitation* (San Francisco: W.H. Freeman, 1973).

[44] N. Arkani-Hamed, S. Dimopoulos, and G. Dvali, Phys. Rev. D **59**, 86004 (1999).

[45] T. Kaluza, Sitz. Preuss. Akad. Wiss. Phys. Math. , 966 (1921).

[46] O. Klein, Z. Phys. **37**, 895 (1926).

[47] R. Spero, J. K. Hoskins, R. Newman, J. Pellam, and J. Schultz, Phys. Rev. Lett. **44**, 1645 (1980).

[48] J. K. Hoskins, R. D. Newman, R. Spero, and J. Schultz, Phys. Rev. D **32**, 3084 (1985).

[49] C. D. Hoyle *et al.*, Phys. Rev. Lett. **86**, 1418 (2001).

[50] J. C. Long *et al.*, Nature **421**, 922 (2003).

[51] J. Chiaverini, S. J. Smullin, A. A. Geraci, D. M. Weld, and A. Kapitulnik, Phys. Rev. Lett. **90**, 151101 (2003).

[52] C. D. Hoyle *et al.*, Phys. Rev. D **70**, 42004 (2004).

[53] S. J. Smullin *et al.*, Phys. Rev. D **72**, 122001 (2005).

[54] D. J. Kapner *et al.*, Phys. Rev. Lett. **98**, 21101 (2007).

[55] R. C. Myers and M. J. Perry, Ann. Phys. **172**, 304 (1986).

[56] F. Tangherlini, Il Nuovo Cimento **27**, 636 (1963).

[57] I. Hinchliffe, K. Lane, and C. Quigg, Rev. Mod. Phys. (1984).

[58] A. D. Martin, W. J. Stirling, R. S. Thorne, and G. Watt, Eur. Phys. J. **70**, 51 (2010).

[59] P. C. Argyres, S. Dimopoulos, and J. March-Russell, Phys. Lett. B **441**, 96 (1998).

[60] R. Emparan, G. T. Horowitz, and R. C. Myers, Phys. Rev. Lett. **85**, 499 (2000).

[61] C. M. Harris and P. Kanti, JHEP **10**, 14 (2003).

[62] D. Ida, K.-y. Oda, and S. C. Park, arXiv **0902.3577v1** (2009).

[63] G. Duffy, C. M. Harris, P. Kanti, and E. Winstanley, JHEP **09**, 049 (2005).

[64] C. M. Harris and P. Kanti, Phys. Lett. B **633**, 106 (2006).

[65] M. Casals, P. Kanti, and E. Winstanley, JHEP **02**, 051 (2006).

[66] M. Casals, S. Dolan, P. Kanti, and E. Winstanley, JHEP **03**, 019 (2007).

[67] M. Casals, S. Dolan, P. Kanti, and E. Winstanley, JHEP **06**, 071 (2008).

[68] N. Arkani-Hamed and S. Dimopoulos, Phys. Rev. D **65**, 52003 (2002).

[69] M. B. Voloshin, Phys. Lett. B **518**, 137 (2001).

[70] M. B. Voloshin, Phys. Lett. B **524**, 376 (2002).

[71] S. Dimopoulos and R. Emparan, Phys. Lett. B **526**, 393 (2002).

[72] A. Jevicki and J. Thaler, Phys. Rev. D **66**, 24041 (2002).

[73] D. M. Eardley and S. B. Giddings, Phys. Rev. D **66**, 44011 (2002).

[74] H. Yoshino and Y. Nambu, Phys. Rev. D **66**, 65004 (2002).

[75] H. Yoshino and Y. Nambu, Phys. Rev. D **67**, 24009 (2003).

[76] S. D. H. Hsu, Phys. Lett. B **555**, 92 (2003).

[77] H. Yoshino and V. S. Rychkov, Phys. Rev. D **71**, 104028 (2005).

[78] M. B. Voloshin, Phys. Lett. B **605**, 426 (2005).

[79] J. R. Klauder, Magic Without Magic: John Archibald Wheeler, in *A Collection of Essays in Honor of his Sixtieth Birthday*, edited by J. R. Klauder, San Francisco: W.H. Freeman, 1972.

[80] D. Ida and K.-I. Nakao, Phys. Rev. D **66**, 64026 (2002).

[81] P. D. D'eath and P. N. Payne, Phys. Rev. D **46**, 658 (1992).

[82] P. D. D'eath and P. N. Payne, Phys. Rev. D **46**, 675 (1992).

[83] P. D. D'eath and P. N. Payne, Phys. Rev. D **46**, 694 (1992).

[84] J. Alwall *et al.*, arXiv **hep-ph/0609017v1** (2006).

[85] ATLAS Collaboration, J. Instrum. **3**, 8003 (2008).

[86] ALICE Collaboration, J. Instrum. **3**, 8002 (2008).

[87] CMS Collaboration, J. Instrum. **3**, 8004 (2008).

[88] LHCb Collaboration, J. Instrum. **3**, 8005 (2008).

[89] S. Dailler, Map of the Geneva region and of the LHC.. Carte de la region lemanique avec l'emplacemen du LHC., 1997, AC Collection. Legacy of AC. Pictures from 1992 to 2002.

[90] L. Evans and P. Bryant, J. Instrum. **3**, 8001 (2008).

[91] CERN, CERN Bulletin **BUL-NA-2010-343. 50/2010**, 3 (2010).

[92] CMS HCAL Collaboration, Eur. Phys. J. **55**, 159 (2008).

[93] CMS Collaboration, Technical Design Report CMS **CERN-LHCC-2000-038; CMS-TDR-006-1** (2000).

[94] CMS HCAL Collaboration, CMS Note **CMS-NOTE-2006-138** (2007).

[95] CMS HCAL Collaboration, Eur. Phys. J. **53**, 139 (2008).

[96] CMS Collaboration, Technical Design Report CMS **CERN-LHCC-2006-001; CMS-TDR-008-1** (2006).

[97] V. Khachatryan *et al.*, JHEP **01**, 080 (2011).

[98] CMS Collaboration, CMS Physics Analysis Summary **CMS-PAS-MUO-10-002** (2010).

[99] W. Adam, R. Frühwirth, A. Strandlie, and T. Todorov, J. Phys. G **31**, 9 (2005).

[100] M. Cacciari, G. P. Salam, and G. Soyez, JHEP **04**, 063 (2008).

[101] CMS Collaboration, CMS Physics Analysis Summary **CMS-PAS-JME-09-008** (2010).

[102] CMS Collaboration, CMS Physics Analysis Summary **CMS-PAS-JME-10-010** (2010).

[103] P. M. Nadolsky *et al.*, Phys. Rev. D **78**, 13004 (2008).

[104] S. Agostinelli *et al.*, Nucl. Instrum. Methods Phys. Res., Sect. A **506**, 250 (2003).

[105] J. Alwall *et al.*, JHEP **9**, 28 (2007).

[106] V. Khachatryan *et al.*, Phys. Rev. Lett. **105**, 211801 (2010).

[107] D. Orbaker, J. Phys. Conf. Ser. **219**, 2053 (2010).

[108] P. Biallass, T. Hebbeker, C. Hof, A. Meyer, and H. Pieta, CMS Analysis Note **AN-2009/048** (2009).

[109] CMS Collaboration, CMS Physics Analysis Summary **CMS-PAS-EWK-10-004** (2010).

[110] K. Agashe, A. Belyaev, T. Krupovnickas, G. Perez, and J. Virzi, Phys. Rev. D **77**, 15003 (2008).

[111] R. S. Chivukula, M. Golden, and E. H. Simmons, Phys. Lett. B **257**, 403 (1991).

[112] R. S. Chivukula, M. Golden, and E. H. Simmons, Nucl. Phys. B **363**, 83 (1991).

[113] B. A. Dobrescu, K. Kong, and R. Mahbubani, Phys. Lett. B **670**, 119 (2008).